Origin of solar surface activity and sunspots

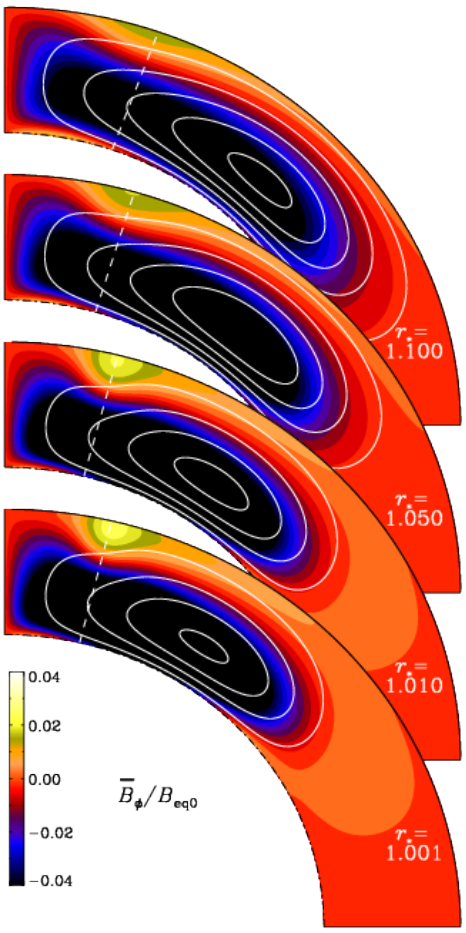

Sarah Jabbari
Nordita, Stockholm, Sweden
Department of Astronomy, Stockholm University, Sweden

Title page picture: Magnetic flux concentration by NEMPI for different values of the stratification parameter $r_\star$ in a spherical coordinate system. NEMPI was excited by a dynamo-generated magnetic field. The flux concentration occurs at a high latitude, indicated by a radial dashed line, near the surface. (Taken from Paper I, Figure 3.)

Origin of solar surface activity and sunspots

Licentiate Thesis

Sarah Jabbari

First Supervisor: Prof. Axel Brandenburg
Second Supervisor: Prof. Göran Scharmer
Mentor: Prof. Garrelt Mellema

Nordita, Stockholm, Sweden

Department of Astronomy, Stockholm University, Sweden

April 23, 2014

List of papers included in the thesis

I **Surface flux concentration in a spherical α^2 dynamo**
Jabbari, S., Brandenburg, A., Kleeorin, N., Mitra, D. and Rogachevskii, I.
A&A, 556, A106 (2013)

II **Magnetic flux concentrations from dynamo-generated fields**
Jabbari, S., Brandenburg, A., Losada, I. R., Kleeorin, N. and Rogachevskii, I.
A&A, submitted (revised in response to referee's comments), arXiv:1401.6107 (2014)

III **Mean-field and direct numerical simulations of magnetic flux concentration from vertical field**
Brandenburg, A., Gressel, O., **Jabbari, S.**, Kleeorin, N. and Rogachevskii, I.
A&A, 562, A53 (2014)

Contents

Abstract

In the last few years, there has been significant progress in the development of a new model for explaining magnetic flux concentrations, by invoking the negative effective magnetic pressure instability (NEMPI) in a highly stratified turbulent plasma. According to this model, the suppression of the turbulent pressure by a large-scale magnetic field leads to a negative contribution of turbulence to the effective magnetic pressure (the sum of non-turbulent and turbulent contributions). For large magnetic Reynolds numbers the negative turbulence contribution is large enough, so that the effective magnetic pressure is negative, which causes a large-scale instability (NEMPI). One of the potential applications of NEMPI is to explain the formation of active regions on the solar surface. On the other hand, the solar dynamo is known to be responsible for generating large-scale magnetic field in the Sun. Therefore, one step toward developing a more realistic model is to study a system where NEMPI is excited from a dynamo-generated magnetic field. In this context, the excitation of NEMPI in spherical geometry was studied here from a mean-field dynamo that generates the background magnetic field. Previous studies have shown that for NEMPI to work, the background field can neither be too weak nor too strong. To satisfy this condition for the dynamo-generated magnetic field, we adopt an "alpha squared dynamo" with an α effect proportional to the cosine of latitude and taking into account alpha quenching. We performed these mean-field simulations (MFS) using the Pencil Code. The results show that dynamo and NEMPI can work at the same time such that they become a coupled system. This coupled system has then been studied separately in more detail in plane geometry where we used both mean-field simulations and direct numerical simulations (DNS).

Losada et al. (2013) showed that rotation suppresses NEMPI. However, we now find that for higher Coriolis numbers, the growth rate increase again. This implies that there is another source that provides the excitation of an instability. This mechanism acts at the same time as NEMPI or even after NEMPI was suppressed. One possibility is that for higher Coriolis numbers, an α^2 dynamo is activated and causes the observed growth rate. In other words, for large values of the Coriolis numbers we again deal with the coupled system of NEMPI and mean-field dynamo. Both, MFS and DNS confirm this assumption. Using the test-field method, we also calculated the dynamo coefficients for such a system which again gave results consistent with previous studies. There was a small difference though, which is interpreted as being due to the larger scale separation that we have used in our simulations.

Another important finding related to NEMPI was the result of Brandenburg et al. (2013), that in the presence of a vertical magnetic field NEMPI results in magnetic flux concentrations of equipartition field strength. This leads to the formation of a magnetic

spot. This finding stimulated us to investigate properties of NEMPI for imposed vertical fields in more detail. We used MFS and DNS together with implicit large eddy simulations (ILES) to confirm that an initially uniform weak vertical magnetic field will lead to a circular magnetic spot of equipartition field strength if the plasma is highly stratified and scale separation is large enough. We determined the parameter ranges for NEMPI for a vertical imposed field. Our results show that, as we change the magnitude of the vertical imposed field, the growth rate and geometry of the flux concentrations is unchanged, but their position changes. In particular, by increasing the imposed field strength, the magnetic concentration forms deeper down in the domain.

Chapter 1

Introduction

1.1 The magnetic Sun

Most phenomena on the solar surface have a direct relation with solar activity. One of the known ones are sunspots. Concentrations of magnetic field are seen as dark areas on the solar surface which have radii between 2 to 20 Mm and life times between one day to a few months. Their temperature is about 3000 to 4000 K, which is cooler than the surrounding temperature of about 6000 K (Stix, 2002). So they look darker; see Figure 1.1. According to Ruzmaikin (2001), Sir Robert Hooke regarded sunspots as soot in the solar fire. About 200 years later, Zeeman discovered the interaction of the magnetic field with the electron angular moment (see Mestel, 1999). This discovery was used by Hale (1908b) to measure the magnitude of the solar magnetic field. In a previous paper, Hale (1908a) reported vortex-like flows in sunspots and thought therefore that this causes their magnetism. Since then, the magnetic nature of sunspots gradually unfolded. The Zeeman effect states that, if a gas is placed in the magnetic field, most of its spectral lines split into three. The separation between lines is directly proportional to strength

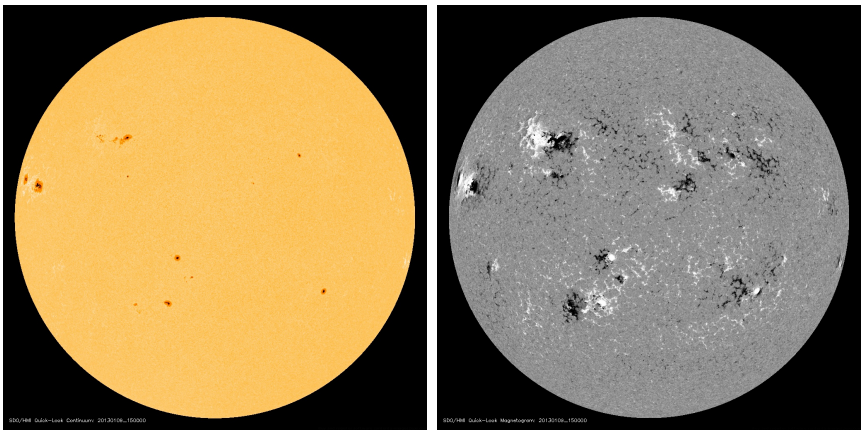

Figure 1.1: Full disk image of the Sun taken by SDO/HMI on 9/01/2013. (a) Continuum image; the dark spots are sunspots. (b) Magnetogram, the black and white colors show opposite polarities of magnetic field in active regions and sunspots.

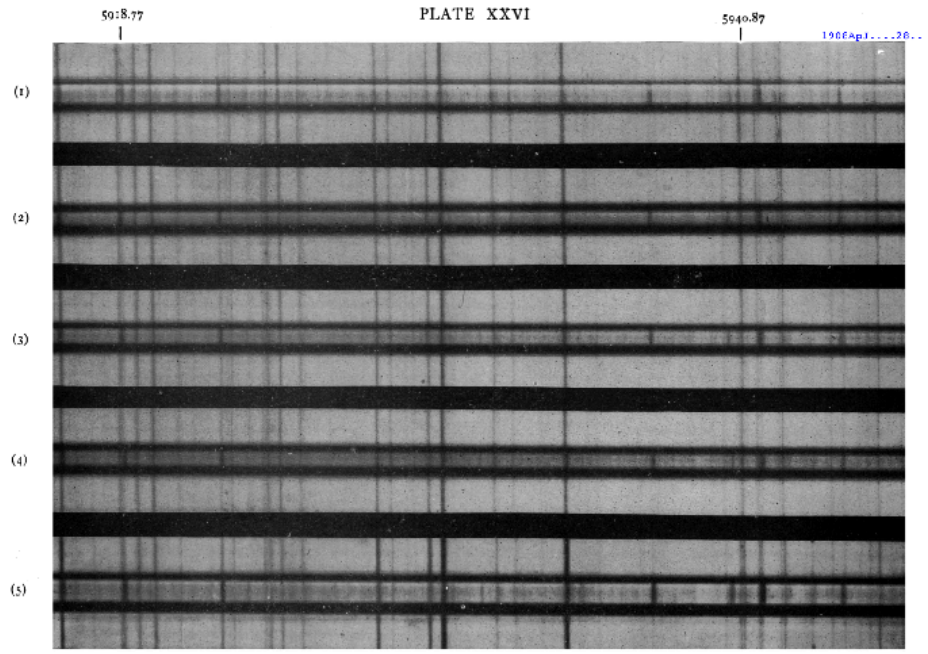

Figure 1.2: The figure shows different component (violet and red) of doublets for both northern and southern spot using a polarizer with different orientations; see panels (1)–(4) and details in the text. Without polarizer, both components are visible; see panel (5). Such a doublet in the spectrum is explained by a very strong magnetic field, which he associates with the sunspot (Hale, 1908b).

of the magnetic field, so one can measure the magnetic field at the solar surface using its spectrum of electromagnetic radiation. Hale considered the spectrum of sunspots and compared it with that from a portion of the Sun without sunspot (not very far from the spot). He showed that the Zeeman effect exists in the spectrum of the sunspot; see Figure 1.2. In the presence of a line-of-sight magnetic field, some of the spectral lines are split into two circularly polarized components with opposite polarization. Using a polarizer, he was able to see which of the two disappeared when changing the polarization plane by 90 degrees. Earlier, Hale (1908a) noticed that spots in the two hemispheres have opposite vorticity[1] (clockwise in the south, and anti-clockwise in the north—just like cyclones on the Earth). Indeed, using the same orientation of the polarizer, he noticed that for a spot in the south only the red component of the λ5940.87Å vanadium line is visible, see panel (1) of Figure 1.2, while for a spot in the north only the violet one is visible; see panel (2). This was for the western part of the umbra, but he found that the same result also for the eastern part of the umbra; see panel (3). Turning the polarizer by 90 degrees, only the red line is visible; see panel (4). Finally, without polarizer, both components of the

[1] Although Evershed (1909) proved this particular observation wrong, it was significant in that it led him to discover what is now called the Evershed flow.

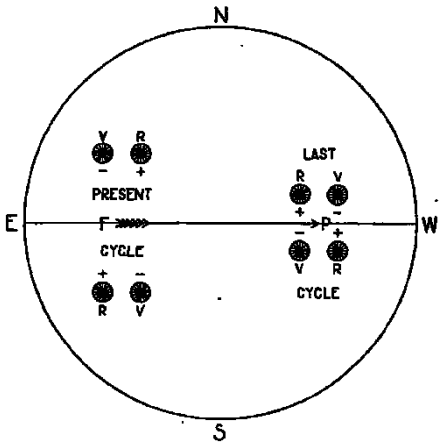

Figure 1.3: This figure presents the polarity laws of sunspots, which were attained by Hale (1919).

vanadium line are visible; see panel (5). Eleven years later, Hale (1919) investigated the polarity of sunspot magnetic fields and showed that it changes with the solar cycle; see Figure 1.3.

When trying to confirm the vortex-like flows found by Hale (1908a), Evershed (1909) found instead a radial outflow, which is now known as the Evershed flow. It extends from the umbra across the penumbra to the outskirts of the spot. This flow was long interpreted as a siphon flow along flux tubes anchored between footpoints of different energy potential leading to a Bernoulli effect (Meyer & Schmidt, 1968; Thomas, 1988; Schlichenmaier et al., 1998; Schlichenmaier, 2002). More recent work by Scharmer et al. (2008) shows that the Evershed flow corresponds to the horizontal flow component of overturning convection in gaps with strongly reduced field strength (Figure 1.4); see also Scharmer (2009), Schlichenmaier (2009) and Scharmer et al. (2011).

1.2 Origin of flux concentrations

In the following we review different approaches proposed to explain magnetic field concentrations on the solar surface. One of them is the rising flux tube model (Parker, 1955a). In particular, there are monolithic (Parker, 1977; Zwaan, 1978) and clustered models (Parker, 1979). In this context, also the convective collapse of the flux tube, which was proposed by Spruit (1979), will be reviewed. The other approach is the negative effective magnetic pressure instability (NEMPI), or a similar instability based on effects from the mean magnetic field. In Section 1.7 a brief summary of the history of the second approach, NEMPI and the role of a mean magnetic field on the formation of flux concentrations is presented. Mean field theory of the dynamo and its formulation is explained in a separate chapter (see Chapter 2). In the same chapter, the α^2 dynamo also is discussed. As NEMPI plays an important role in PhD project, I will explain in Chapter 3 its basics and review

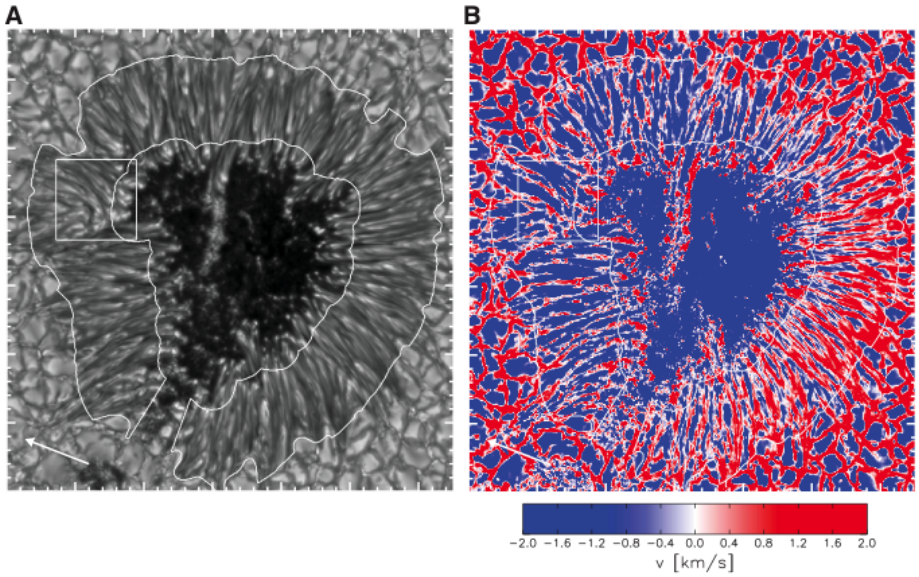

Figure 1.4: Continuum image (A) and Doppler map (B) of a sunspot. The white contour shows the interior penumbra. In the Doppler map, blue represents motions toward the observer and red shows movement away from it (Scharmer et al., 2011).

the work done so far in more detail. Later, the interaction between dynamo-generated magnetic field and NEMPI in spherical coordinates (Paper I) and also in plane geometry with rotation (Paper II) will be discussed in Chapter 4. In Chapter 5, the investigation of the behavior of the system in the presence of NEMPI driven by an imposed vertical magnetic field (Paper III) is presented (see Chapter 5). In the last chapter, more realistic model with solar parameters and the presence of ionization and radiative transfer will be discussed. I also will present some primarily results of this ongoing study (see Chapter 6).

1.3 Omega loop theory

Most sunspots form in specific areas on the solar surface, which are known as active regions. In such active regions most solar surface phenomena like sunspots, solar flares and coronal mass ejections (CMEs) frequently form. Active regions appear bright in X-ray and ultraviolet images. They correspond to regions of relatively strong magnetic field. There are different theories about the formation and evolution of these regions. In 1955, Parker presented an idea about sunspot formation which could explain most properties of sunspots such as their east-west orientation, bipolarity, their position in low

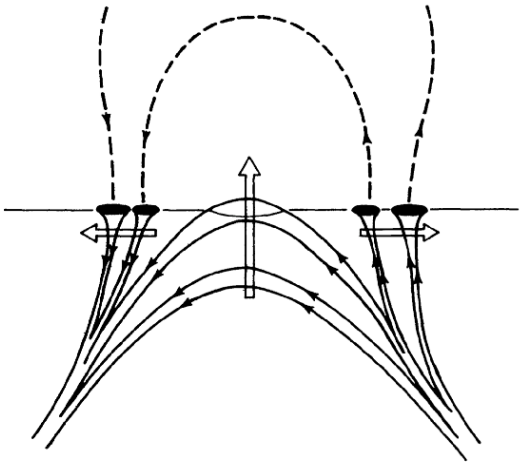

Figure 1.5: Illustration of a rising tree of magnetic flux tubes which reaches the surface and forms a bipolar region (Zwaan, 1987).

latitudes (Spörer's law) and the polarity inversion with time and latitude. He suggested that a large enough buoyant magnetic flux tube tends to rise and can carry flux lines of the Sun's toroidal field to the upper layers. As a flux tube pierces the photosphere, it forms a pair of sunspots (Parker, 1955a). In his original paper, he assumed that the flux tubes originated from a depth of around 10^4 km. In a review, Parker (1977) discussed various ideas regarding the magnetic origin of solar activity. The early ideas of magnetic flux appearance in the solar photosphere have also been described by Zwaan (1978). Figure 1.5 shows in summary how a rising flux tube can lead to the formation of a bipolar region. Zwaan reviewed these ideas in subsequent papers (Zwaan, 1985, 1987).

In 1978, Parker suggested that the interaction between a weak magnetic field and convective processes in small flux tubes leads to an amplification of the magnetic field. In the quiet sun, small magnetic flux tubes exist in conjunction with supergranular boundaries, where there is a strong downdraft. He presented a new effect in small flux tubes, which leads to strong cooling and thus to magnetic field concentration. This effect is different from that of other theories, which suggest radiation as the main mechanism for cooling the photosphere. Those theories assume that this mechanism is related to the suppression of convective heat transfer by the magnetic field. In fact, the plasma compresses the magnetic field in the downdraft such that the enhanced buoyancy force compensates the downward flow in the flux tube. This phenomenon leads to cooling inside the flux tube. Parker showed theoretically that a small decrease in temperature over many scale heights may lead to a reduced magnetic pressure in the solar surface, which results in magnetic field concentration (Parker, 1978).

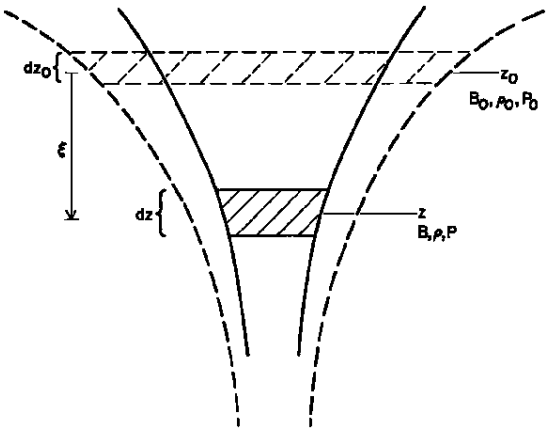

Figure 1.6: Schematic representation of a flux tube before (dashed line) and after (solid line) convective collapse (Spruit, 1979).

1.4 Convective collapse

Spruit (1979) followed Parker's idea regarding magnetic flux tubes to explain convective collapse of small flux tubes. He found a critical value for the magnetic field strength needed to get such field concentrations. For a field stronger than a certain critical value, the magnetic field will suppress convection. He computed this critical value for the solar convection zone to be about 1270 G at the solar surface (see also Spruit & Zweibel, 1979). In this case flux tubes are divided into two types, stable flux tubes (with magnetic field bigger than the critical value) and unstable ones (with magnetic field less than the critical value). For the second group of tubes, when the field strength is low enough, the instability sets in and, according to Parker, leads to downward flow, the temperature decreases, which results in magnetic field concentration in the upper layers. But there is a limitation for this downward flow too. If the resulting magnetic field is bigger than the critical value, the tube settles in a new equilibrium with the same properties as the initial one, but with a lower energy. This is what is called convective collapse of flux tubes. Figure 1.6 shows a sketch of convective collapse of a magnetic flux tube. On the other hand, since the value of the resulting magnetic field is small enough, downward displacement in the tube continues and the tube vanishes at the surface and sinks down to a deeper layer.

There is also a recent work by Spruit (2012), who confronted some ideas about the solar cycle with observations. He suggested that the interaction between magnetic field and turbulent convection is not responsible for the solar cycle and that the buoyancy instability of the magnetic field itself results in the solar cycle. He argues that the magnetic field is generated in the radiative interior and that the source of energy comes from the small radial shear that develops as the Sun spins down. Simulations have not yet shown that such a dynamo mechanism can really work (Zahn et al., 2007).

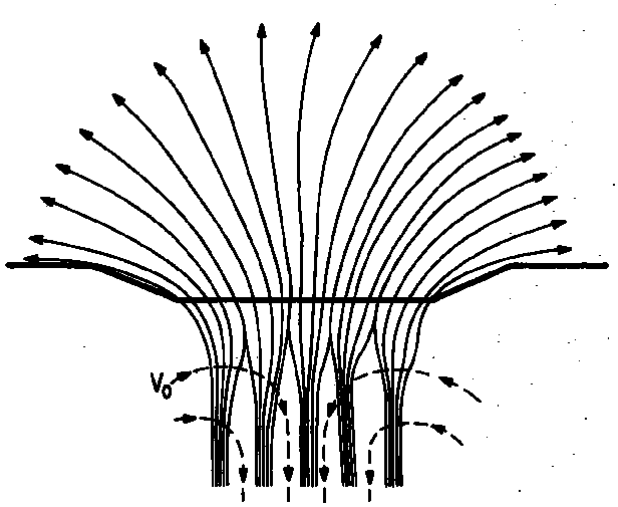

Figure 1.7: A sketch of a group of flux tubes with in the first 1000 km under the surface that pressed together to form an active region or a sunspot (Parker, 1979).

1.5 Clustered versus monolithic sunspot models

Later in 1979, Parker suggested that magnetic field concentrations at the surface, which lead to the formation of sunspots, are due to many small flux tubes. This is referred to as the cluster model of sunspots, as opposed to the more traditional monolithic models where the sunspot would have uniformly distributed magnetic flux. With this model he explained how a group of separate magnetic flux tubes in the convection zone reaches the surface through magnetic buoyancy, where they produce a single big flux concentration with a correspondingly larger magnetic field; see Figure 1.7. In this paper he investigated the instability and structure of sunspots using this new model. He emphasizes that flux tubes of different size have the same Wilson depression. Wilson depression occurs because of the fact that in a spot the surface where the optical depth is equal to unity is geometrically deeper. The reason is that, because the spot is cooler, the hotter radiating surface lies at a deeper level. Although, the visible surface inside sunspots of different size is lowered relative to the quiescent photosphere due to Wilson depression, it is found to be independent of the size of the spot. This is only possible for the clustered model where the individual elements lead to a certain Wilson depression, which can then not change as more tubes are being attached to each other. Even today the question of clustered versus monolithic sunspot remains open; see the recent discussion by Rempel & Schlichenmaier (2011).

In the second part of the paper, he discusses aerodynamic properties of such flux tubes (Parker, 1979). He shows in his later work that, under some assumptions, it is possible to obtain the depth where the hypothetical anchor points lie. These anchor points are the positions where the flux starts rising. By using this theory, one can estimate the depth of origin of solar active regions and sunspots. Parker (1984) suggested that this depth is

roughly equal to the horizontal size of an active region. For a normal active region, this depth is about 10^5 km (100 Mm). In his paper, he used the behavior of active regions at the solar surface to explain the dynamical behavior beneath the convection zone (Parker, 1984).

1.6 Flux concentrations in deep convection simulations

In the last ten years, there have been numerous studies of rising flux tubes in simulations; see Cheung et al. (2008); Rempel et al. (2009); Cheung et al. (2010); Rempel & Cheung (2014). There are also simulations with adiabatic stratification (Hood et al., 2012; Archontis, 2012; Archontis et al., 2013). They investigated the rising process from the convection zone into the solar atmosphere.

In their recent paper, they have studied the effects of flux tube-like initial conditions on the dynamics, rise and evolution of tubes. They have shown that strong twisting is not necessary for a tube to reach to the corona, as was previously thought (Fan, 2001, 2009). In their simulations the rising flux tube pierces the photosphere and forms loops in the corona (Archontis et al., 2013). Figure 1.8 shows one of their simulation results. One can see the formation of two loops due to the weakly twisted initial flux at $z = 0$ (upper row) and also the appearance of the raising flux at $z = 540$ km (middle row).

Although coherent flux tubes, which are assumed to form deep in the convection zone, are believed to have the potential to develop active regions, it has also been shown that the convective motions are important in the formation of active regions by promoting the uplift of magnetic structures between supergranular downdrafts. Recently, Stein & Nordlund (2012) introduced magnetoconvection as a possible origin of magnetic flux emergence from a depth of about 20 Mm. They demonstrated using a numerical simulation that it is not necessary to have an initially coherent flux tube to form an active region; see Figure 1.9. In fact, magnetoconvection with a horizontal 1 kG magnetic field injected at the bottom of their computational domain gives rise to bi-polar structures at the surface and thus leads to the formation of an active region.

1.7 Flux concentrations from mean-field effects

A different idea, which is able to explain large-scale magnetic field concentrations, was proposed by Kleeorin et al. (1989) and Kleeorin et al. (1990). They suggested that the effective (mean-field) magnetic pressure (turbulent and non-turbulent contributions) in a turbulent plasma can be negative, which leads to a large-scale magnetic instability. The turbulent pressure is of course positive, but it is being suppressed by the mean magnetic field. If this field causes a suppression of the turbulent pressure that is stronger than the intrinsic (non-turbulent) pressure, the net effect is negative.

This instability occurs in the presence of strong density stratification; and thus preferentially near the solar surface on scales encompassing those of many turbulent eddies. This instability is invoked as an explanation for magnetic field concentrations in the upper

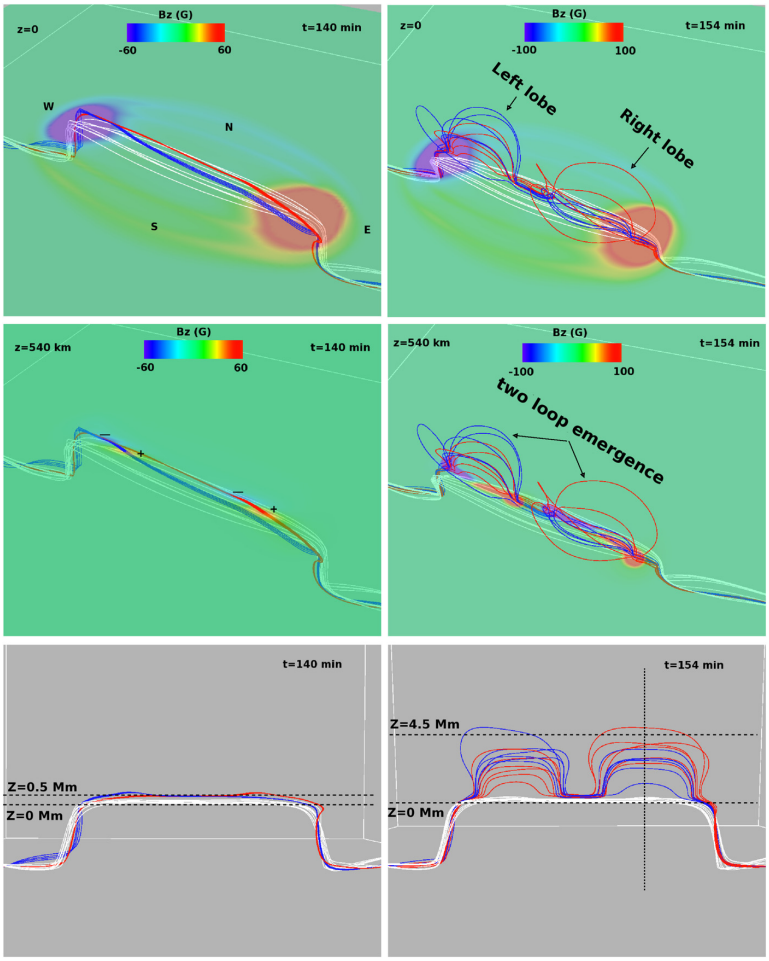

Figure 1.8: Visualization of the vertical magnetic field together with field lines for two different times (left and right columns) at the surface (top), at 540 km height (middle) and the side view of field lines (bottom) (Archontis et al., 2013).

layer of the convection zone (Kleeorin et al., 1989, 1990). As NEMPI is the basic theory behind our research, it will be described in more detail in Chapter 3.

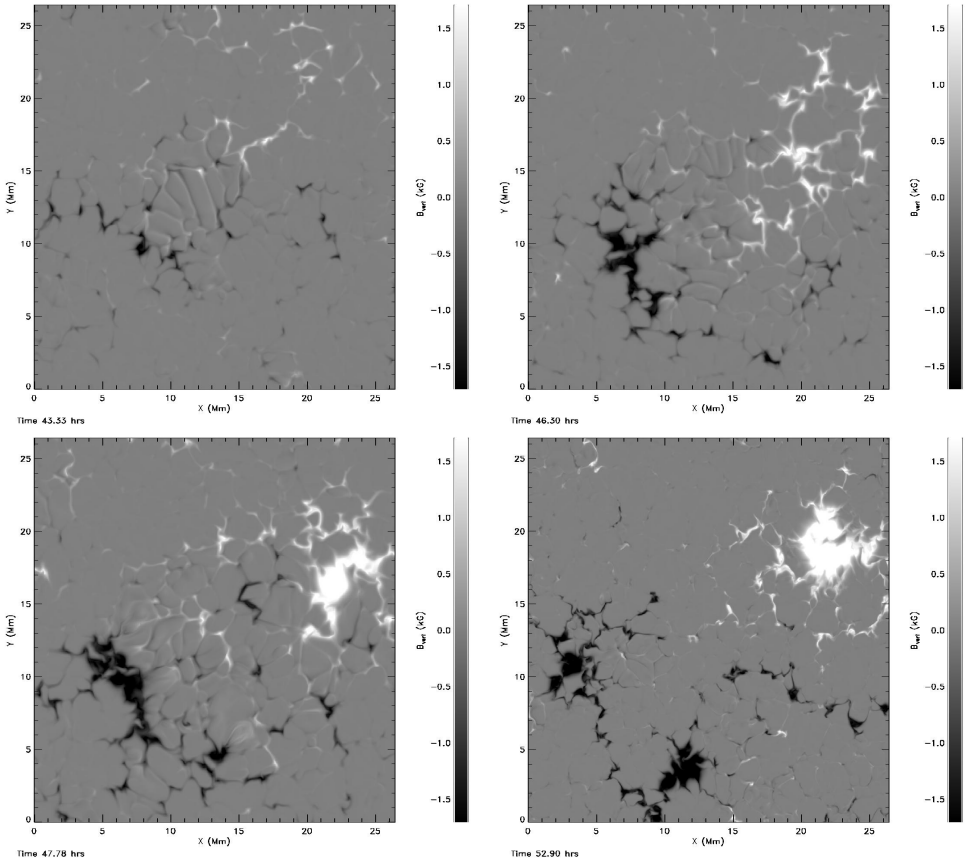

Figure 1.9: Separation of opposite polarity of magnetic field (magnetic field concentration) on the upper layer due to magnetoconvection resulted by Stein & Nordlund (2012).

Chapter 2

Mean-field approach in Dynamo theory

2.1 Two-scale assumption

Dynamo theory of the Sun's magnetic field starts from the idea that, in a rotating body, toroidal and poloidal magnetic fields can act as power sources of each other. This early idea of Parker (1955b) suggests that stretching of the poloidal field due to differential rotation in the body leads to the creation of toroidal field and, on the other hand, the effect of helical turbulence on the toroidal field produces a poloidal field. One approach to formulate this idea is through mean-field theory, where one assumes that all dependent variables are written in the form of a mean and a fluctuating part, i.e.,

$$\boldsymbol{F} = \overline{\boldsymbol{F}} + \boldsymbol{f}. \tag{2.1}$$

The important point here is that we do not impose any restriction on the strength of the fluctuating part, so this is different from perturbation theory. The two important equations here are the momentum and induction equations:

$$\rho\frac{\mathrm{D}\boldsymbol{U}}{\mathrm{D}t} = -\boldsymbol{\nabla}p + \boldsymbol{J}\times\boldsymbol{B} + \rho\boldsymbol{g} + \rho\nu\left(\boldsymbol{\nabla}^2\boldsymbol{U} + \frac{1}{3}\boldsymbol{\nabla}(\boldsymbol{\nabla}\cdot\boldsymbol{u}) + 2\mathsf{S}\cdot\boldsymbol{\nabla}\ln\rho\right), \tag{2.2}$$

$$\frac{\partial\boldsymbol{B}}{\partial t} = \boldsymbol{\nabla}\times\boldsymbol{U}\times\boldsymbol{B} + \eta\boldsymbol{\nabla}^2\boldsymbol{B}, \tag{2.3}$$

where ν and η are kinematic viscosity and magnetic diffusivity, respectively, and both are assumed to be constant. S is the traceless rate-of-strain tensor of the flow. By applying mean-field theory to the induction equation we are able to consider the effect of turbulence on the magnetic field fluctuation by introducing the mean electromotive force. We introduce

$$\boldsymbol{B} = \overline{\boldsymbol{B}} + \boldsymbol{b}, \tag{2.4}$$

$$\boldsymbol{U} = \overline{\boldsymbol{U}} + \boldsymbol{u}, \tag{2.5}$$

where $\overline{\boldsymbol{B}}$ and $\overline{\boldsymbol{U}}$ are the mean values and $\boldsymbol{b}$ and $\boldsymbol{u}$ are the fluctuations. Again, I emphasize that there is no restriction on the strength of $\boldsymbol{b}$ and $\boldsymbol{u}$. In the next section I will explain how this theory leads to a complete description of an α^2 dynamo.

2.2 Mean-field equations and α^2 dynamo

By substituting relations (2.4) and (2.5) into (2.3), taking averages of these equations, and using the Reynolds averaging rules, we get:

$$\frac{\partial \overline{\boldsymbol{B}}}{\partial t} = \boldsymbol{\nabla} \times (\overline{\boldsymbol{U}} \times \overline{\boldsymbol{B}}) + \eta \boldsymbol{\nabla}^2 \overline{\boldsymbol{B}} + \boldsymbol{\nabla} \times \overline{\boldsymbol{\mathcal{E}}}, \tag{2.6}$$

where $\overline{\boldsymbol{\mathcal{E}}} = \overline{\boldsymbol{u} \times \boldsymbol{b}}$. In the case of isotropic turbulence and under the assumption of perfect scale separation, the mean electromotive force (EMF) is given by (Moffatt, 1978)

$$\overline{\boldsymbol{\mathcal{E}}} = \alpha \overline{\boldsymbol{B}} - \eta_{\mathrm{t}} \boldsymbol{\nabla} \times \overline{\boldsymbol{B}}. \tag{2.7}$$

This expression implies that for a non-vanishing α effect, a mean magnetic field can be generated by the α^2 dynamo. Whether or not this happens depends on boundary conditions, the size of the domain, and the value of turbulent magnetic diffusivity. Substituting (2.7) into (2.6), we get

$$\frac{\partial \overline{\boldsymbol{B}}}{\partial t} = \boldsymbol{\nabla} \times (\overline{\boldsymbol{U}} \times \overline{\boldsymbol{B}}) + \eta \boldsymbol{\nabla}^2 \overline{\boldsymbol{B}} + \boldsymbol{\nabla} \times (\alpha \overline{\boldsymbol{B}}) - \boldsymbol{\nabla} \times (\eta_{\mathrm{t}} \boldsymbol{\nabla} \times \overline{\boldsymbol{B}}). \tag{2.8}$$

Let us consider the case when there is no mean flow ($\overline{\boldsymbol{U}} = 0$) and the turbulence is homogeneous. This implies that α and η_{t} are constants. It is therefore straightforward to write the mean induction equation in the form

$$\frac{\partial \overline{\boldsymbol{B}}}{\partial t} = \eta_{\mathrm{T}} \boldsymbol{\nabla}^2 \overline{\boldsymbol{B}} + \alpha \boldsymbol{\nabla} \times \overline{\boldsymbol{B}}, \tag{2.9}$$

where

$$\eta_{\mathrm{T}} = \eta + \eta_t \tag{2.10}$$

is total magnetic diffusivity. We seek for a solution of (2.9) as the real part of an expression of the form

$$\overline{\boldsymbol{B}}(\boldsymbol{x}) = \hat{\boldsymbol{B}}(\boldsymbol{k}) e^{i\boldsymbol{k}\cdot\boldsymbol{x} + \lambda t}. \tag{2.11}$$

Substituting this expression into the mean induction equation, we obtain

$$\lambda \hat{\boldsymbol{B}} = \alpha i \boldsymbol{k} \times \hat{\boldsymbol{B}} - \eta_T k^2 \hat{\boldsymbol{B}}. \tag{2.12}$$

The dispersion relation is then

$$(\lambda + \eta_T k^2) \left((\lambda + \eta_T k^2)^2 - \alpha^2 k^2 \right) = 0, \tag{2.13}$$

which yields the growth rate of the α^2 dynamo as

$$\lambda = -\eta_T k^2 + |\alpha k|. \tag{2.14}$$

The α^2 dynamo is characterized by a parameter called the dynamo number, which is defined as

$$C_\alpha = \alpha/\eta_{\rm T} k_1, \tag{2.15}$$

where α is the typical value of the α effect, and k_1 is the lowest wavenumber of the magnetic field that can be fitted into the domain. Using the concept of kinetic helicity for isotropic turbulence, these coefficients are given by

$$\alpha \approx \alpha_0 \equiv -\tfrac{1}{3}\tau\overline{\boldsymbol{\omega}\cdot\boldsymbol{u}}, \quad \eta_t \approx \eta_{\rm t0} \equiv \tfrac{1}{3}\tau\overline{\boldsymbol{u}^2}, \tag{2.16}$$

where $\tau = (u_{\rm rms}k_{\rm f})^{-1}$ is an estimate of the correlation time, $k_{\rm f}$ is the wavenumber of the energy-carrying eddies (or forcing wavenumber in forced turbulence), and

$$\epsilon_{\rm f} \equiv \overline{\boldsymbol{\omega}\cdot\boldsymbol{u}}/k_{\rm f}u_{\rm rms}^2 \tag{2.17}$$

is the normalized kinetic helicity. We know that in a stratified rotating system, kinetic helicity will be produced self-consistently by the interaction between rotation and stratification. In this case it was suggested that the relation between kinetic helicity and Coriolis numbers, $\mathrm{Co} = 2\Omega/u_{\rm rms}k_{\rm f}$, has the form of

$$\epsilon_{\rm f} \equiv \epsilon_{\rm f0}\,\mathrm{Gr}\,\mathrm{Co} \quad (\text{for } \mathrm{Gr}\,\mathrm{Co} \lesssim 0.1). \tag{2.18}$$

Here, Gr is the gravitational parameter, which is defined by

$$\mathrm{Gr} = g/c_{\rm s}^2 k_{\rm f}, \tag{2.19}$$

where g is the gravitational acceleration and $c_{\rm s}$ is the sound speed. Combining (2.15)–(2.19), the dynamo number takes the form

$$C_\alpha = \epsilon_{\rm f0}\,\mathrm{Gr}\,\mathrm{Co}\,k_{\rm f}/k_1. \tag{2.20}$$

This expression indicates that the combination of stratification and rotation leads to an α effect. This result was confirmed through DNS of Losada et al. (2013) and in Paper II. In the MFS of Paper I, we assumed an additional ad hoc nonlinearity called α quenching. This means that α is then replaced by

$$\alpha = \frac{\alpha_0}{1 + Q_\alpha \overline{\boldsymbol{B}}^2/B_{\rm eq}^2}. \tag{2.21}$$

The larger the quenching parameter Q_α, the smaller is the magnetic field resulting from the α effect.

Like for the induction equation (2.6), there are also mean-field parameterizations for the the mean momentum equation (2.2). It has the form

$$\rho\frac{\mathrm{D}\overline{\boldsymbol{U}}}{\mathrm{D}t} = -\boldsymbol{\nabla}p + \rho\boldsymbol{g} + \overline{\boldsymbol{F}}_{\rm M} + \overline{\boldsymbol{F}}_{\rm K}, \tag{2.22}$$

where p is the gas pressure, $\overline{\boldsymbol{F}}_{\rm K}=\rho\nu_{\rm t}(\nabla^2\overline{\boldsymbol{U}}+\frac{1}{3}\boldsymbol{\nabla}\boldsymbol{\nabla}\cdot\overline{\boldsymbol{U}}+2\overline{\mathbf{S}}\boldsymbol{\nabla}\ln\overline{\rho})$ is the viscous force from the mean flow (used in all mean-field and large eddy simulations), while $\overline{\boldsymbol{F}}_{\rm M}$ is the mean Lorentz force which, and can be expressed as

$$\overline{\boldsymbol{F}}_{\rm M}=\overline{\boldsymbol{J}}\times\overline{\boldsymbol{B}}+\frac{1}{2\mu_0}\boldsymbol{\nabla}(q_{\rm p0}\overline{\boldsymbol{B}}^2)+..., \tag{2.23}$$

where dots refer to extra terms that have been neglected, because they turned out not to be important (Brandenburg et al., 2012; Käpylä et al., 2012). Here, the second term represents one of the most important turbulent contributions to the mean Lorentz force. This will be discussed in Chapter 3. In nonlinear mean-field simulations, one solves (2.9) together with (2.22), and the continuity equation for different boundary conditions.

2.3 A comment on various instabilities

There are various hydrodynamic and hydromagnetic instabilities. NEMPI is closely related to the Parker instability, except that it requires that the scale of variation of the density is short compared with the scale of variation of the magnetic field. For the Parker instability, this is exactly the other way around; see Brandenburg et al. (2012). Furthermore, the NEMPI draws energy from the kinetic energy of the turbulence while the Parker instability draws potential energy. There is another conceptual difference between NEMPI and many other instabilities. Normally, one analyzes the stability of a system at rest. For example, the outer layers of the Sun are unstable to convection and this leads to turbulence. Asking therefore about instabilities such as NEMPI is questionable, because the system is already unstable. On the other hand, asking the same question at the level of the mean-field equations is straightforward and uncontroversial. A familiar example is the mean-field dynamo. However, identifying the dynamo in a turbulence simulation is already not straightforward and it is difficult to determine unambiguously a growth rate associated with this instability. It is the same with NEMPI. To determine its growth rate, one has to isolate large-scale features that are not expected to be generated otherwise and then determine their growth. Examples of this have been shown by Brandenburg et al. (2011) and Kemel et al. (2012b). The problem becomes even more complicated when we deal with two mean-field instabilities at the same time, namely NEMPI and the dynamo instability. In this connection, one may compare the scale of NEMPI and dynamo instabilities. In general, we have small-scale and large-scale dynamo instabilities, which occur in the absence of an imposed magnetic field if the plasma has large enough magnetic Reynolds number Re_M. The scale of NEMPI lies between these two. In the following we describe how we can use simulations to determine the relevant mean-field parameters of the large-scale dynamo.

2.4 Test-field method for computing the dynamo coefficients

An important numerical method for calculating dynamo coefficients, α_{ij} and η_{ij} is the test field method (TFM). Starting from (2.6) and employing various independent vector magnetic fields called test fields, $\overline{\boldsymbol{B}}^{pq}$, instead of $\overline{\boldsymbol{B}}$ while keeping the velocity fixed, one is able to calculate $\overline{\boldsymbol{\mathcal{E}}}$. From that and using (2.7) one gets a system of equations, which can be solved to obtain the coefficients α_{ij} and η_{ij}. Knowing that $\overline{\boldsymbol{J}}^{pq} = \boldsymbol{\nabla} \times \overline{\boldsymbol{B}}^{pq}$, this system of equations will have a form of

$$\overline{\mathcal{E}}_i^{pq} = \alpha_{ij} \overline{B}_j^{pq} - \eta_{ij} \overline{J}_j^{pq}. \tag{2.24}$$

Finally the transport coefficients are defined by

$$\alpha = \tfrac{1}{2}(\alpha_{11} + \alpha_{22}), \quad \eta_t = \tfrac{1}{2}(\eta_{11} + \eta_{22}), \tag{2.25}$$

$$\gamma = \tfrac{1}{2}(\alpha_{21} - \alpha_{12}), \quad \delta = \tfrac{1}{2}(\eta_{21} - \eta_{12}), \tag{2.26}$$

where $\alpha_{11}, ..., \alpha_{22}, \eta_{11}...$ and η_{22} are the different elements of the α and η tensors. For further details about TFM see Schrinner et al. (2005, 2007); Brandenburg (2005); Brandenburg et al. (2010). We have used this method to calculate the dynamo coefficients for a system with large-scale separation in the presence of the rotation (Paper II).

Chapter 3

Negative effective magnetic pressure instability

In addition to the dynamo instability, which has a particular type and scale (see Section 2.3), there is also another intermediate-scale instability which makes it possible to concentrate magnetic field from a weak initial magnetic field in a stratified and turbulent plasma. In comparison with the dynamo-generated magnetic field in the Sun, the magnetic structures resulting from NEMPI have smaller scales than the dynamo field. This instability might occur in the upper layers of the Sun and can cause the formation of active regions on the solar surface. In order to be able to explain the origin of active regions by NEMPI, it is necessary to study NEMPI in more detail. In this chapter the theory of negative effective magnetic pressure instability is explained.

3.1 Negative effective magnetic pressure

The idea of NEMPI started from the fact that the effective magnetic pressure can be negative in the case of a turbulent plasma. The total effective (or mean-field) pressure in the turbulent plasma is

$$p_{\rm tot} = p_{\rm g} + p_{\rm mag} + p_{\rm t}, \tag{3.1}$$

where $p_{\rm g}$ and $p_{\rm mag}$ are the gas and magnetic ($\overline{\boldsymbol{B}}^2/8\pi$) pressures, respectively.[1] Furthermore, $p_{\rm t}$ is the turbulent pressure, which is given by the isotropic part of the total (kinetic plus magnetic) stress tensor,

$$\overline{\rho}\,\overline{u_i u_j} - \frac{\overline{b_i b_j}}{4\pi} + \frac{\overline{b^2}}{8\pi}\delta_{ij} = \left(\overline{\rho}\overline{\boldsymbol{u}^2} - \frac{\overline{\boldsymbol{b}^2}}{4\pi} + \frac{\overline{3\boldsymbol{b}^2}}{8\pi}\right)\frac{\delta_{ij}}{3} + ... = \left(\underbrace{\overline{\rho}\overline{\boldsymbol{u}^2} + \frac{\overline{\boldsymbol{b}^2}}{4\pi}}_{\approx\text{const}} - \frac{\overline{\boldsymbol{b}^2}}{8\pi}\right)\frac{\delta_{ij}}{3} + ..., \tag{3.2}$$

where dots refer to additional anisotropic parts. This shows that, if the total energy density of the turbulence is approximately conserved, the turbulent pressure *decreases*

[1] In this thesis, I use gaussian units, while in Papers I and III we use SI units. In practice, it means that the permeability μ_0 in those papers is to be replaced by 4π. In Paper II we use nondimensional quantities which are obtained by replacing μ_0 by unity. This is also done in the next section and most of the simulations, except in Chapter 6, where I present new simulations using physical units applicable to the Sun.

with increasing $\overline{\boldsymbol{b}^2}$. In their early work, Kleeorin et al. (1989, 1990) formulated this in the form

$$p_{\rm t} = E_{\rm m}/3 + 2E_{\rm k}/3, \tag{3.3}$$

where $E_{\rm m} = \overline{b}^2/8\pi$ is the magnetic fluctuation energy density and $E_{\rm k} = \overline{\rho}\,\overline{u^2}/2$ is kinetic energy density. Again, making use of the assumption that the total energy density of the turbulence is approximately conserved ($E_{\rm tot} = E_{\rm m} + E_{\rm k} \approx$ const), the turbulent pressure can be written in the form

$$p_{\rm t} = 2E_{\rm tot}/3 - E_{\rm m}/3. \tag{3.4}$$

On the other hand, we expect $E_{\rm m}$ to be an increasing function of $p_{\rm mag}$, so we can expand it in a series of $p_{\rm mag}$

$$E_{\rm m} = E_{\rm m}(0) + a_T p_{\rm mag} + ..., \tag{3.5}$$

inserting this into (3.4) and using $q_{\rm p} = a_T/3$ we get

$$p_{\rm t} = p_{\rm t}(0) - q_{\rm p}\frac{\overline{B}^2}{8\pi}, \tag{3.6}$$

where the first term is the turbulent pressure in the case that the large-scale magnetic field is absent (the net effect of turbulence on the plasma pressure) and the second term determines the turbulent contribution to the mean magnetic pressure. Here, $q_{\rm p}$ is a function of the large-scale magnetic field that is expected to be positive. The expression for total pressure thus attains the form

$$p_{\rm tot} = p_{\rm g} + p_{\rm t}(0) + (1 - q_{\rm p})\frac{\overline{B}^2}{8\pi}. \tag{3.7}$$

We introduce the effective magnetic pressure as

$$P_{\rm eff} = (1 - q_{\rm p})\frac{\overline{B}^2}{8\pi}, \tag{3.8}$$

which can also be written in dimensionless form

$$\mathcal{P}_{\rm eff} = \tfrac{1}{2}(1 - q_{\rm p})\beta^2. \tag{3.9}$$

Here, $\beta = \overline{B}/B_{\rm eq}$, $B_{\rm eq} = \sqrt{4\pi\rho u_{\rm rms}^2}$ is the equipartition value of a magnetic field, where $\rho u_{\rm rms}^2/2$ is the turbulent kinetic energy. This relation indicates that for $q_{\rm p} > 1$, the effective magnetic pressure is negative, so it decreases the total pressure of the plasma. This gives rise to a large-scale instability which is driven at the expense of the total turbulence energy.

Kemel et al. (2012a) presented a useful parameterization of $q_{\rm p}$ as

$$q_{\rm p} = \frac{q_{\rm p0}}{1 + \beta^2/\beta_{\rm p}^2} \equiv \frac{\beta_\star^2}{\beta_{\rm p}^2 + \beta^2}, \tag{3.10}$$

where $\beta_\star = \sqrt{q_{\rm p0}}\beta_{\rm p}$. These two parameters, $\beta_\star$ and $\beta_{\rm p}$, are calculated by using direct numerical simulations (DNS).

3.2 DNS of the negative effective magnetic pressure instability

In this section I present a summary of the study of NEMPI using DNS. Here, we solve the equations of magnetohydrodynamics in the form of

$$\frac{\mathrm{D}\boldsymbol{U}}{\mathrm{D}t} = -c_\mathrm{s}^2\boldsymbol{\nabla}\ln\rho + \frac{1}{\rho}\boldsymbol{J}\times\boldsymbol{B} + \boldsymbol{f} + \boldsymbol{g} + \boldsymbol{F}_\nu, \tag{3.11}$$

$$\frac{\partial\boldsymbol{A}}{\partial t} = \boldsymbol{U}\times\boldsymbol{B} + \eta\nabla^2\boldsymbol{A}, \tag{3.12}$$

$$\frac{\partial\rho}{\partial t} = -\boldsymbol{\nabla}\cdot\rho\boldsymbol{U}. \tag{3.13}$$

Here $\boldsymbol{B} = \boldsymbol{B}_0 + \boldsymbol{\nabla}\times\boldsymbol{A}$, where $\boldsymbol{B}_0$ is the imposed uniform magnetic field (which can be horizontal or vertical) and $\boldsymbol{A}$ is the magnetic vector potential (nonuniform). Viscous force is defined as $\boldsymbol{F}_\nu = \boldsymbol{\nabla}\cdot(2\nu\rho\mathsf{S})$ and $\boldsymbol{J}$ is the current density, ν and η are kinematic viscosity and magnetic diffusivity due to Spitzer conductivity of the plasma, respectively. To drive turbulence one has two options, convection or forcing function. The forcing function $\boldsymbol{f}$, which is added to the momentum equation, is a random plane wave changing at every time step with average wavenumber k_f/k_1. The averaged momentum equation can be expressed in the form

$$\frac{\partial}{\partial t}\overline{\rho}\,\overline{\boldsymbol{U}}_i = -\frac{\partial}{\partial x_j}\overline{\Pi}_{ij} + \overline{\rho}\,g_i, \tag{3.14}$$

where $\overline{\Pi}_{ij}$ is the averaged momentum stress tensor, which has the form

$$\overline{\Pi}_{ij} = \overline{\Pi}^\mathrm{m}_{ij} + \overline{\Pi}^\mathrm{f}_{ij}. \tag{3.15}$$

Here

$$\overline{\Pi}^\mathrm{m}_{ij} = \overline{\rho}\,\overline{U}_i\overline{U}_j + \delta_{ij}\left(\overline{p} + \tfrac{1}{2}\overline{\boldsymbol{B}}^2\right) - \overline{B}_i\overline{B}_j - 2\nu\overline{\rho}\,\overline{\mathsf{S}}_{ij}, \tag{3.16}$$

and

$$\overline{\Pi}^\mathrm{f}_{ij} = \overline{\rho}\,\overline{u_iu_j} + \tfrac{1}{2}\delta_{ij}\overline{\boldsymbol{b}^2} - \overline{b_ib_j}. \tag{3.17}$$

$\overline{\Pi}^\mathrm{m}_{ij}$ is the contribution from the mean field and $\overline{\Pi}^\mathrm{f}_{ij}$ is the contribution from the fluctuating field. As we are interested in the contribution from the fluctuating part that results form the mean field, we should calculate $\overline{\Pi}^\mathrm{f}_{ij}$ also for zero mean field (let us call it $\overline{\Pi}^\mathrm{f0}_{ij}$), and then subtract it from $\overline{\Pi}^\mathrm{f}_{ij}$. We can parameterize the dependence of the resulting tensor, $\Delta\overline{\Pi}^\mathrm{f}_{ij} \equiv \overline{\Pi}^\mathrm{f}_{ij} - \overline{\Pi}^\mathrm{f0}_{ij} = -q_\mathrm{p}\delta_{ij}\overline{\boldsymbol{B}}^2/2 + q_\mathrm{s}\overline{B}_i\overline{B}_j - q_\mathrm{g}\overline{g}_i\overline{g}_j$, by introducing coefficients like q_p, q_s and q_g. So, one challenge related to NEMPI is to calculate these coefficients for different setups.

In the following subsection a summary of the DNS and MFS for the study of NEMPI is presented.

3.3 Results from DNS and MFS

Kleeorin et al. (1989, 1990) derived an expression for the effective magnetic force, which has the form of

$$\boldsymbol{F}_{\rm m} = -\boldsymbol{\nabla}\left[(1-q_{\rm p})\frac{\overline{\boldsymbol{B}}^2}{8\pi}\right] + \overline{\boldsymbol{B}}\cdot\boldsymbol{\nabla}\left[(1-q_{\rm s})\frac{\overline{\boldsymbol{B}}}{4\pi}\right], \tag{3.18}$$

where $q_{\rm s}$ and $q_{\rm p}$ are nonlinear functions of the large-scale magnetic field, $\overline{\boldsymbol{B}}$. In particular, the functions $q_{\rm s}(\overline{B})$ and $q_{\rm p}(\overline{B})$ relate the sum of the Reynolds and Maxwell stresses to the mean magnetic field. Another important point is that the growth rate of the instability is directly related to the large-scale magnetic field. The functions $q_{\rm p}(\overline{B})$ and $q_{\rm s}(\overline{B})$ have been derived by the spectral τ approach (Kleeorin et al., 1996; Rogachevskii & Kleeorin, 2007) and the renormalization approach (Kleeorin & Rogachevskii, 1994). In both approaches, one tries to approximate the nonlinear terms. In the τ approach one expresses nonlinear terms by a suitable damping term, where τ is a damping time. In particular, the deviation of the third moments caused by nonlinear terms from the background turbulence are expressed in terms of the the deviation of the corresponding second moments in the form of the relaxation term. The renormalization approach comprises a replacement of real turbulence with that characterized by effective turbulent transport coefficients. This procedure enables one to derive equations for the transport coefficients: turbulent viscosity, turbulent magnetic diffusivity, and turbulent magnetic coefficients as a function of scale inside the inertial range. The small parameter in the renormalization approach is the ratio of the energy of the mean magnetic field to the turbulent kinetic energy of the background turbulence (with zero-mean fields). The spectrum and statistical properties of the background turbulence are assumed to be given here. Figure 3.1 shows plots of these functions for different values of the magnetic Reynolds numbers. It also shows the effective mean magnetic pressure, $\mathcal{P}_{\rm eff}(\beta)$ and effective mean magnetic tension, $\sigma_{\rm B} = (1-q_{\rm s})\overline{B}^2/B_{\rm eq}^2$, where $B_{\rm eq}$ is the equipartition field strength.

In subsequent papers, Kleeorin and collaborators investigate the energy transfer from small-scale to large-scale magnetic field due to the negative effective magnetic pressure instability (NEMPI) and they tried to explain solar oscillation and sunspot formation by this new mechanism (Kleeorin et al., 1993, 1996). In this theory, active regions are regarded as a shallow phenomenon. In 2011, NEMPI was detected in DNS by Brandenburg et al. (2011). Since then it is of great interest to investigate different aspects of NEMPI and its interaction with the turbulent plasma. It was also studied in MFS in a highly stratified isothermal gas with large plasma β (Brandenburg et al., 2010, 2011; Kemel et al., 2012a). Figure 3.2 shows how a magnetic structure develops and then sinks. This is believed to be a consequence of the negative effective magnetic pressure. To achieve pressure equilibrium, the gas pressure must increase, so the density also increases and the structure becomes heavier and sinks. This result from DNS is in striking similarity to earlier MFS of Brandenburg et al. (2010). Another interesting result is of Kemel et al. (2012a) who showed in MFS that three-dimensional structures with variation along the direction of the mean field (here the y direction) form if one includes the effect of negative

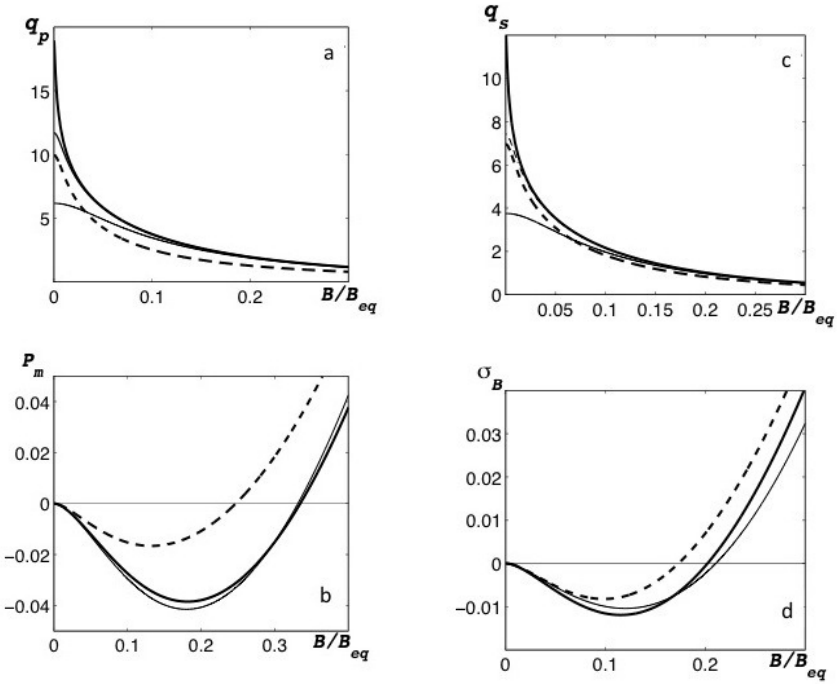

Figure 3.1: (a) The function $q_{\rm p}(\overline{\boldsymbol{B}})$ for different values of the magnetic Reynolds number; $\mathrm{Re}_M = 10^3$ (thin solid line), $\mathrm{Re}_M = 10^6$ (dashed-dotted line); $\mathrm{Re}_M = 10^{10}$ (thick solid line) for homogeneous turbulence and at $\mathrm{Re}_M = 10^6$ (dashed line) for convective turbulence. (b) The effective mean magnetic pressure $p_{\rm m}$ at $\mathrm{Re}_M = 10^6$ for homogeneous turbulence (thick solid line), and for convective turbulence for the horizontal field (dashed) and for vertical field (thin solid line. (c) The function $q_{\rm s}(\overline{\boldsymbol{B}})$ for different values of the magnetic Reynolds numbers; $\mathrm{Re}_M = 10^3$ (thin solid line), $\mathrm{Re}_M = 10^6$ (thin dashed-dotted line), $\mathrm{Re}_M = 10^{10}$ (thick solid) for a homogeneous turbulence, and at $\mathrm{Re}_M = 10^6$ (dashed line) for a convective turbulence. (d) The effective mean magnetic tension $\sigma_{\rm B}$ at $\mathrm{Re}_M = 10^6$ for homogeneous turbulence (thick solid line), and for a convective turbulence (Rogachevskii & Kleeorin, 2007).

effective magnetic tension; see Figure 3.3.

Kemel et al. (2013b), Kemel et al. (2013a), and Kemel et al. (2012b) considered NEMPI as a possible mechanism for the formation of active regions. They also investigated the effect of non-uniformity of the magnetic field on NEMPI. In their last paper they increased the number of eddies to 30 to get large enough scale separation to excite NEMPI (Kemel et al., 2013b,a, 2012b).

Käpylä et al. (2012) studied the effects of turbulent convection on NEMPI. They demonstrated that NEMPI still works if the entropy equation is included, provided the background stratification is adiabatic, i.e., there is no stabilizing force associated with Brunt-Väisälä oscillations.

Losada et al. (2012, 2013) used both MFS and DNS to investigate the effect of rotation

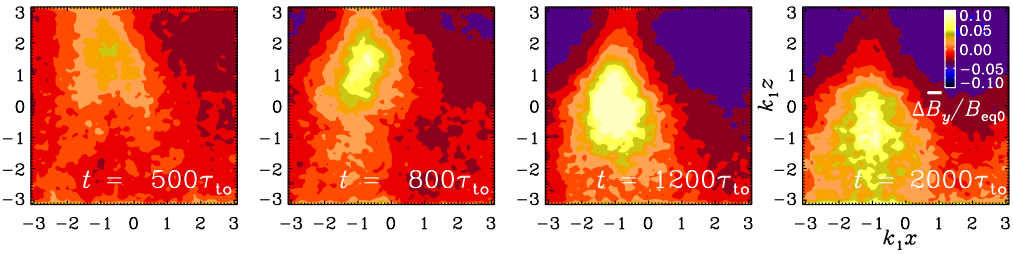

Figure 3.2: First numerical demonstration of NEMPI in DNS that shows a large-scale magnetic flux concentration resulting from NEMPI (Brandenburg et al., 2011).

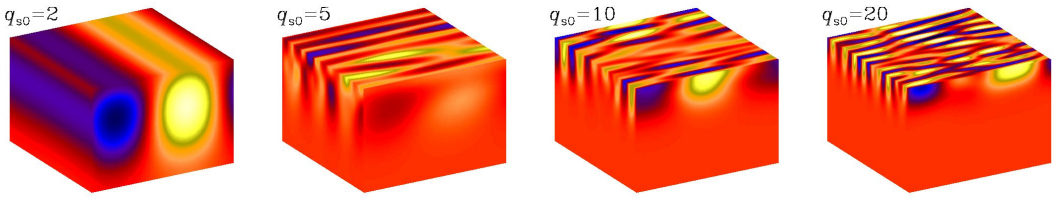

Figure 3.3: Another demonstration of NEMPI with mean field modeling. Here it has been shown how tension forces affect the magnetic field pattern (Kemel et al., 2012a).

on NEMPI. They considered the development of NEMPI in the case of large-scale separation in the presence of rotation. In MFS, they found that even relatively slow rotation, with Coriolis numbers, $\mathrm{Co} = 2\Omega/u_{\rm rms}k_{\rm f}$, around 0.1 suppresses NEMPI. Their results of MFS for small Co are compatible with DNS, which show that there is good agreement between DNS and MFS in the case of NEMPI. In the case of high Coriolis numbers (Co), however, the growth rate of NEMPI increases, which was not consistent with the fact that the rotation suppresses NEMPI (see also Figure 6 of Paper II). This implies that there is another source which provides growth of magnetic field. This mechanism acts at the same time as NEMPI or even after NEMPI was suppressed. One explanation was that for higher values of Co, an α^2 dynamo is activated and causes this observed growth rate. In other words, for large values of Co we deal with some kind of coupled system of NEMPI and dynamo. In Chapter 4, I will present the results of a more detailed study of this system, which led to two publications, Papers I and II.

The functions, $q_{\rm p}(\beta)$ and $q_{\rm s}(\beta)$ were determined in DNS by Brandenburg et al. (2010, 2012) and Käpylä et al. (2012). They showed by DNS of forced turbulence with an imposed field that these functions are positive and exceed unity for weak fields. Here, $\beta = \overline{B}/B_{\rm eq}$ is the mean magnetic field normalized by the equipartition field strength. They used this result to explain how the reduction happens on the effective Lorentz force, which leads to negative effective magnetic pressure. Their simulation demonstrates that $q_{\rm p}$ should be larger than $2q_{\rm s}$. They investigated both the solution of the forced turbulence and mean-field MHD on the large-scale Lorentz force in a density-stratified layer. They

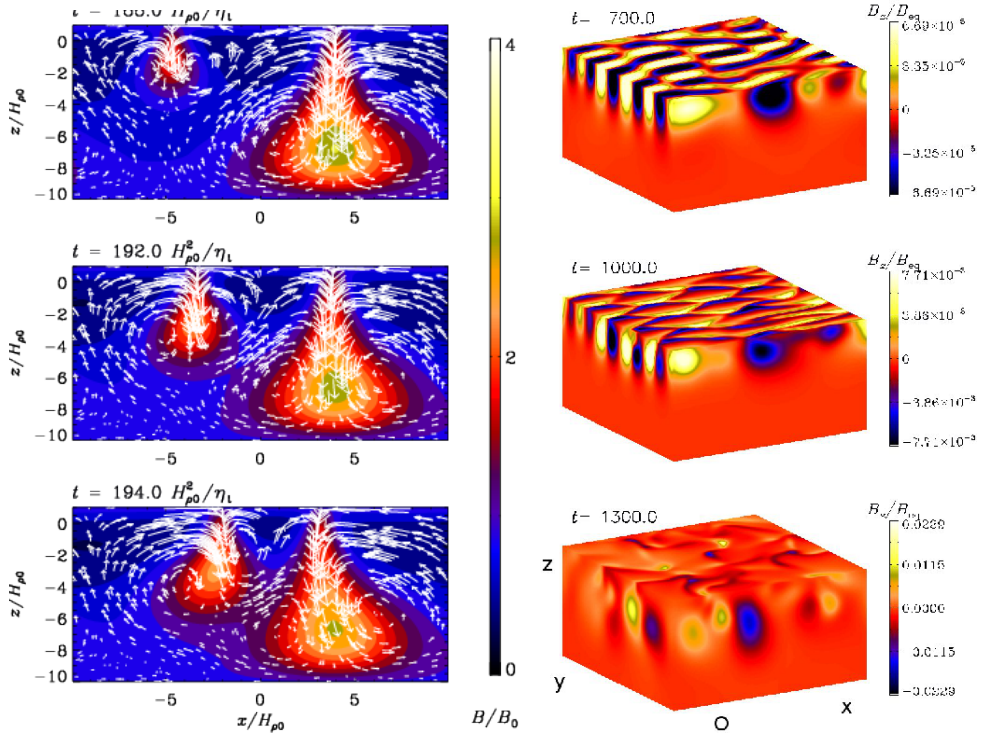

Figure 3.4: Left: time evolution of the meridional magnetic field and velocity vectors, which have resulted from 2D simulations. Right: 3D simulation of magnetic field showing three different times. The field concentration due to NEMPI forms near the surface (Brandenburg et al., 2010).

showed in their simulations that the growth rate of the instability increases with increasing $q_{\rm p}$, strength of stratification, and imposed field: enhancing any one of these quantities increases the growth rate. They also have found that increasing the magnetic diffusivity decreases the growth rate. Figure 3.4 shows their MFS results. In this figure, the time evolution of magnetic field after saturation of the instability is shown for two cases; 2D (left) and 3D (right) simulations. It can be seen from both plots how NEMPI leads to the formation of magnetic structures near the surface. The interesting thing about this figure is the bipolar magnetic field structures, which are formed on the surface in the case of 3D simulations (Brandenburg et al., 2010). The suppression of turbulent hydrodynamic pressure by the mean magnetic field also was studied in DNS. Brandenburg et al. (2012) simulated strongly stratified, isothermal turbulent plasma (large Reynolds number) with an imposed uniform magnetic field (smaller than the equipartition value) and proper scale separation. Their results showed that the ratio $B_0/B_{\rm eq0}$ should be in a suitable range for NEMPI to work. This is consistent with theory and mean-field calculations.

Recently, the formation of bipolar regions also was observed in DNS by Warnecke et al. (2013). In their simulation, they added an outer coronal layer to the upper boundary.

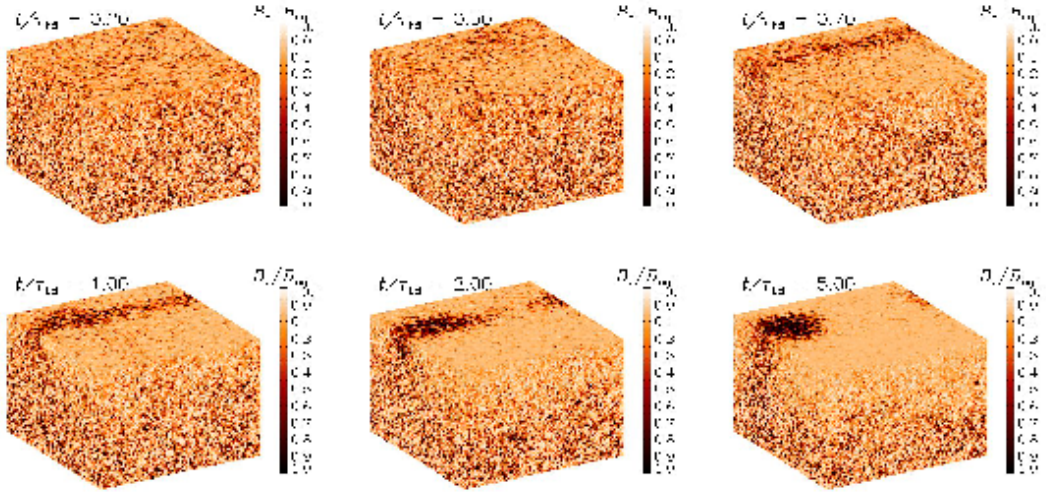

Figure 3.5: Magnetic spot formation due to NEMPI near the surface in the case of vertical imposed magnetic field (Brandenburg et al., 2013).

They showed that the presence of this new upper 'boundary condition' helps the formation of a bipolar magnetic region, which later decays.

One of the important recent works on NEMPI was done by Brandenburg et al. (2013), where, for the first time, they excited NEMPI by imposing a vertical magnetic field with a vertical field boundary condition in forced turbulence for a stratified plasma. Their DNS result showed that in the case of a vertical imposed field, because of the absence of saturation by what they call a potato sack effect, the resulting magnetic field is stronger, even larger than the equipartition value, and after 1.5 turbulent-diffusive times, a magnetic spot forms on the surface; see Figure 3.5. This achievement led us to investigate NEMPI with a vertical imposed field in more detail. The result of this study was presented in a follow-up paper on this subject (Paper III). Because of the importance of this result, I will discuss it in more detail in Chapter 5. In the next subsection, I present a comparison between NEMPI and the flux tube model.

3.4 NEMPI versus flux tubes

The reason that NEMPI leads to field structures only near the surface is that NEMPI works only in highly stratified turbulent plasma. As the magnetic field concentration formed by NEMPI happens very close to the surface, where stratification is strong, it can directly lead to the formation of active regions or even sunspots. Here, the buoyancy force also accompanies NEMPI in the formation of magnetic structures near the surface. Magnetic buoyancy acts both with flux tubes and in a stratified continuous magnetic field without any flux tubes. In the case of NEMPI, the second situation applies. The flux tube

picture was used in early theories to explain the rising of magnetic structures from deep inside the convection zone to reach the surface and create active regions (Parker, 1955a; Zwaan, 1978). In this mechanism, as the flux tube has a magnetic field stronger than its surroundings, the magnetic pressure inside the tube is bigger than the magnetic pressure outside. So, to have equal total (gas and magnetic) pressure inside and outside the tube, the density inside the flux tube has to decrease. The resulting buoyancy force due to the density difference between inside and outside the tube makes the tube rise. One of the arguments against this model arises from the large magnitude of the magnetic field at the bottom of the convection zone. For a rising flux tube to preserve the same orientation during its ascent, a magnetic field of 10^5 G is needed (Choudhuri & D'Silva, 1990; D'Silva & Choudhuri, 1993). This magnetic field is more than a hundred times stronger than the equipartition value. Such large field strengths have not yet been found in simulations of turbulent dynamos and make this assumption questionable. One must therefore look for alternatives.

The field concentrations generated by NEMPI were expected not to be strong enough to form active regions or sunspots. It has therefore been suggested that NEMPI may be accompanied by some other mechanism. One possible mechanism was proposed by Kitchatinov & Mazur (2000). In their model, the suppression of convection motions (heat flux) by a mean magnetic field is assumed to lead to a decrease in temperature and formation of magnetic field concentration. They took into account the fluid motion on flux emergence by using mean-field model. The instability they described is due to the fact that eddy diffusivity is quenched by strong magnetic fields. They suggested that this new instability, is physically compatible with convective collapse phenomena presented by Spruit (1979) and Spruit & Zweibel (1979). In the near-surface layer, cooling from the surface due to radiation and heating from bellow due to convective motions are balanced. The instability sets in when this balance is disturbed by reduced heat transfer due to the fact that the magnetic field quenches the turbulent thermal diffusivity. This leads to further cooling at the surface; the structure sinks to compensate the heat loss, which helps to concentrate the mean magnetic field even further (Kitchatinov & Mazur, 2000). It is of interest to study this instability further using both MFS and DNS.

There is still a long way to go before a more realistic and convincing model can be achieved. For instance the effect of ionization or the presence of radiation have not yet been studied in the case NEMPI. As these two processes play important roles in the solar surface dynamics, we expect that with new models including ionization and radiation, it will be possible to investigate new aspects of NEMPI. I will return to this aspect in Chapter 6.

Chapter 4

Combined effects of stratification and rotation on NEMPI

As all previous simulations of NEMPI were done with an imposed magnetic field and in plane geometry, it was of interest to see how using a dynamo-generated magnetic field will affect NEMPI and how it develops in spherical geometry. The results of this project showed that it is possible to have a situation where NEMPI is excited even when the initial field is dynamo-generated. The dynamo and negative effective magnetic pressure instabilities are then coupled. Losada et al. (2013) showed that in the case of sufficiently rapid rotation, dynamo action sets in, which leads to the complicated coupled system of dynamo and NEMPI. In fact, there is a close competition between stratification, one of the main factors to excite NEMPI, and rapid rotation, which suppresses NEMPI, but together with stratification it also produces kinetic helicity and thereby an α effect, which allows the large-scale dynamo to work. In this chapter, our understanding of this coupled system is presented.

4.1 NEMPI and α^2 dynamos, study of a coupled system in spherical geometry

As mentioned before, there are many aspects related to NEMPI which are poorly understood and should be investigated in more detail. In this regard, we have proposed a new model that combines NEMPI with a dynamo in spherical coordinates (Paper I). The model is described in the following subsection and the results of this work are presented and discussed in the subsection after that.

4.1.1 Outline of the model

In Paper I, we used MFS of NEMPI with an α^2 dynamo to investigate NEMPI under more realistic conditions like global geometry and dynamo-generated magnetic fields. In the case of spherical geometry it is not obvious how a magnetic field should be imposed, and it is therefore more straightforward to use a dynamo-generated one. In this paper, the combined effects of a dynamo and NEMPI in a highly stratified turbulent plasma with an adiabatic equation of state are investigated. The simulations showed that these two work

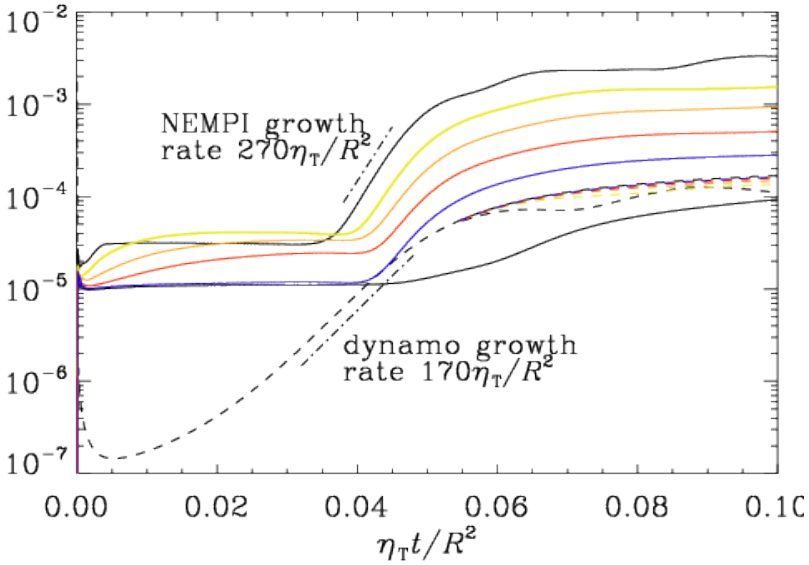

Figure 4.1: Dependence of $B_{\rm rms}$ (dashed lines) and $U_{\rm rms}$ (solid lines) on time for $q_{\rm p}0 = 0$ (black), 5 (blue), 10 (red), 20 (orange), 40 (yellow), and 100 (upper black line for $B_{\rm rms}$), showing dynamo growth together with NEMPI versus dimensionless time. (Taken from Figure 2 of Paper I.)

together in a constructive manner. Similar to what was found in previous simulations, in a highly stratified plasma when the value of the magnetic field is about a few percent of the equipartition value, NEMPI starts growing. We used α quenching to achieve to a suitable saturation magnitude of the mean magnetic field such that NEMPI works. We assume axisymmetry, adopt a perfect conductor boundary condition on the outer radius, assume the field to be antisymmetric about the equator (dipolar parity) and applied regularity conditions on the axis. The major results of the simulations are shown in the following subsection.

4.1.2 Major results of Paper I

Figure 4.1 shows the comparison between the NEMPI growth and the dynamo growth rate of this coupled system. At early times, the rms value of the magnetic field, Brms, grows exponentially, giving a growth rate of about $170\eta_{\rm T}/R^2$, where $\eta_{\rm T}$ is the total magnetic diffusivity defined in Equation (2.10). The rms velocity, $U_{\rm rms}$, shows a weak residual value, but after $\eta_{\rm T}t/R^2 > 0.035$ it grows sharply at a larger rate, $270\eta_{\rm T}/R^2$; see Figure 4.1. It has been shown in this plot that this results for $U_{\rm rms}$ depends only slightly on $q_{\rm p}0$, and this only when the dynamo is saturated, which is when $\eta_t t/R^2 > 0.05$; see Figure 4.1.

Figure 4.2 shows meridional cross-sections of $B/B_{\rm eq}$ (color coded) together with magnetic field lines of poloidal magnetic field for different values of $q_{\rm p}0$ and stratification parameter, $r_\star$ for the α quenching parameter $Q_\alpha = 1000$. Here the stratification is poly-

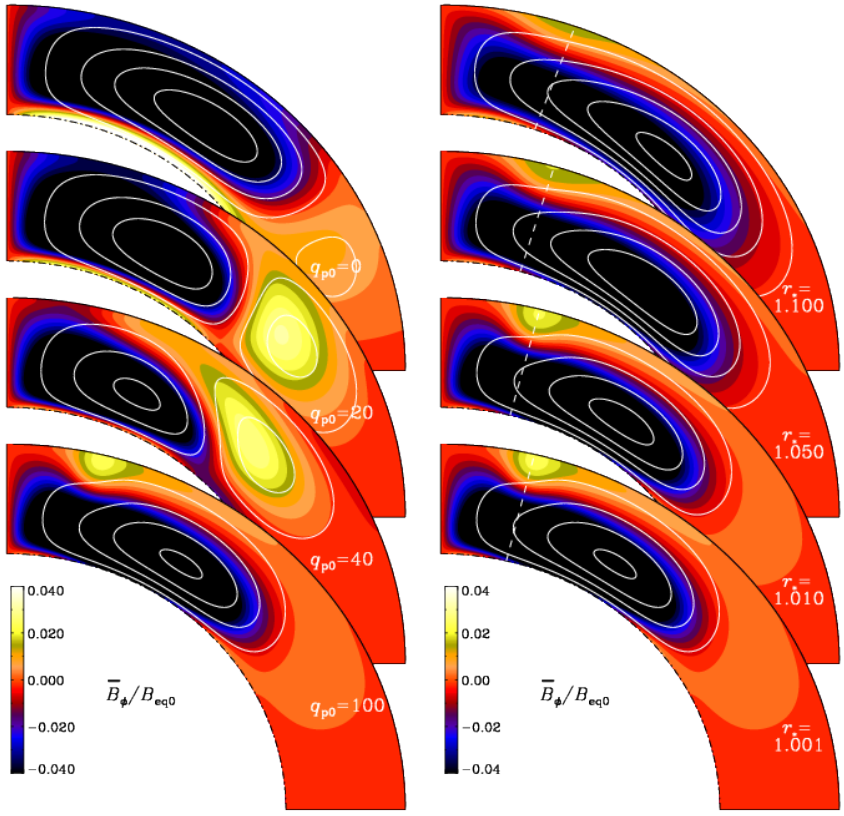

Figure 4.2: In the left plot, the effect of the q_p function on formation of magnetic field concentrations is illustrated (The prefactor $q_{\rm p0}$ takes the values 0, 20,40 and 100). On the right side, the effect of stratification on the development of NEMPI is shown ($r_\star$ takes the values 1.100, 1.050, 1.010 and 1.001). (Taken from Paper I.)

tropic and $r_\star$ is a radius outside the star where the temperature would be zero. The closer $r_\star$ is to R, the stronger is the stratification. For $r_\star/R = 1.001$, the density contrast is almost 10^4; see Table 1 of Paper I. The dashed lines indicate latitudes 49°, 61.5°, 75.6°, and 76.4°. It can be seen from the plot that just for $q_{\rm p}0 > 60$, field concentrations occur. Because the growth rate of the instability is inversely proportional to the pressure scale height for strong stratification (Kemel et al., 2012b), one should expect intense field concentration; in other words, for weaker stratification, field concentrations vanishes completely.

Figure 4.3 shows another result, namely the effect of the quenching parameter on the location of the field concentration. For smaller quenching or, in other words, for a stronger mean magnetic field, NEMPI occurs at lower latitudes. Also, for larger quenching, the magnetic field is smaller and NEMPI is more pronounced. Interesting results are obtained when the initial mean magnetic field is very weak ($Q_\alpha = 10000$). In this case an oscillatory poleward migration occurs, which is due to the effect of NEMPI on the dynamo. The frequency of this oscillatory behavior is about $\omega = 11.3\,\eta_t/R^2$. Such poleward migration

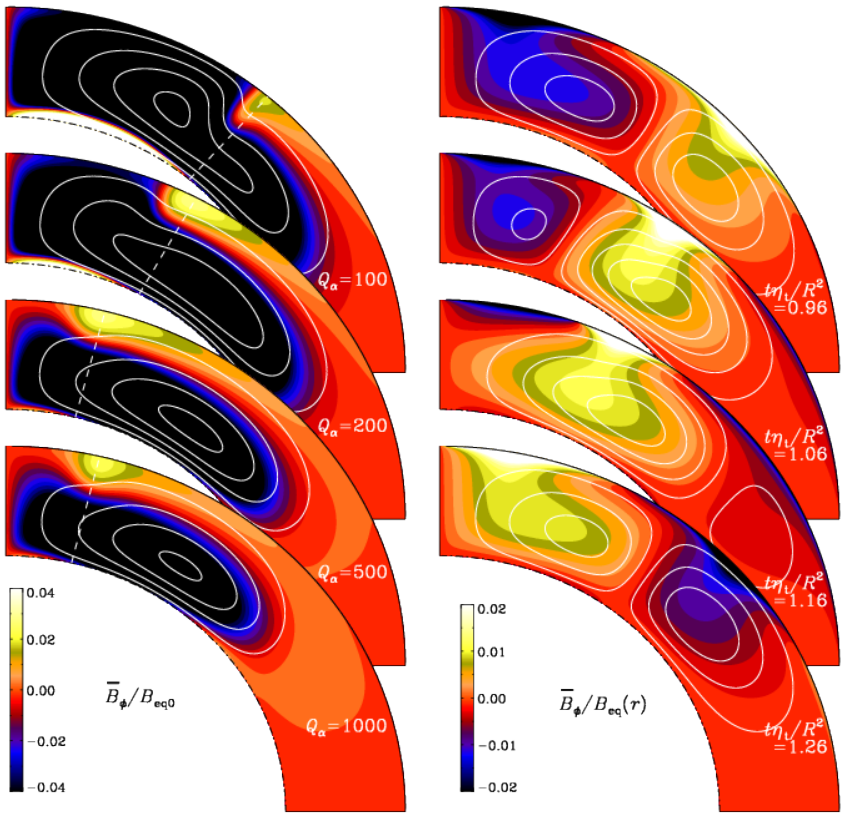

Figure 4.3: The plot in the left is meridional cross-sections of magnetic field for different values of quenching parameter, Q_α, for $r = 1.001$ (highest stratification) and $q_p = 100$. The illustration of poleward migration in the case of very strong quenching, $Q_\alpha = 10000$, has been presented in the plot on the right-hand side. (Taken from Paper I.)

also was observed in the case of NEMPI in the presence of rotation (Losada et al., 2012, 2013). So, it is possible that they may be based on a similar mechanism. In the plot, the toroidal field is normalized by the local equipartition value, and the colors indicate $\overline{B}/B_{\rm eq}(r)$.

4.1.3 Future works

In this study of NEMPI, we have used MFS. The investigation of NEMPI driven by a dynamo-generated magnetic field in spherical coordinates is also possible using DNS. Recent DNS have already demonstrated the possibility of bipolar regions in simulations either with an imposed horizontal magnetic field (Warnecke et al., 2013) or a dynamo-generated one (Mitra et al., 2014). We would expect bipolar regions also in spherical simulations and it would be interesting to see their tilt angle and other aspects of these dynamos. At the same time, after increasing our knowledge about NEMPI in wedge-like two-dimensional spherical geometry, it would also be possible to develop our model to a

three-dimensional case. In the next section, I present the study of NEMPI and dynamo instability for plane geometry in the presence of rotation.

4.2 Combined effects of stratification and rotation on NEMPI

4.2.1 Outline of the model

As mentioned in the previous section, if a dynamo-generated magnetic field is used to excite NEMPI, we encounter a complicated system of dynamo and NEMPI. The main aim of this study is to understand this coupled system in more detail. For this reason we adopt plane geometry and add rotation to a corresponding setup. The first step was to reproduce the results of Losada et al. (2013) for fast rotation by using both MFS and DNS. In their DNS, as they increased the rotation, NEMPI was suppressed by rotation but when the Coriolis number, Co, was increased even further, the growth rate of the instability starts to increase. They suggest that this effect might be due to the activation of an α^2 dynamo by the high rotation rate (high Coriolis number, Co) and the presence of stratification. To prove this, we used both DNS and MFS of turbulent plasmas in plane geometry in the presence of rotation. NEMPI works with high stratification, while rapid rotation together with stratification is the key to activate a large-scale dynamo. This is when the competition between rotation and stratification starts. Using Ω to calculate the dynamo number, C_α, by DNS calculations of kinetic helicity and comparing the result with data from the test-field method (TFM) gives us the opportunity of providing all the proper conditions for the system to change to a coupled system of NEMPI and dynamo (for computational details see Chapter 2 on the α^2 dynamo and Paper II for more detail).

It was also of interest to investigate the effects of changing the gravity parameter, $\mathrm{Gr} = g/c_\mathrm{s}^2 k_\mathrm{f}$ on the growth rate of the instability with and without rotation. By using $k_\mathrm{f} = u_\mathrm{rms}/3\eta_t$, one can write Gr in the form

$$\mathrm{Gr} = 3\eta_t g/c_\mathrm{s}^2 u_\mathrm{rms}, \tag{4.1}$$

where η_t is the turbulent diffusivity. We emphasize that in this work the stratification is taken to be isothermal, so the parameter $r_\star/R$ used in Section 4.1 has no significance and would be infinite. The main results of this study are presented in the next subsection.

4.2.2 Major results of Paper II

Our DNS and MFS confirmed that, although rotation tends to suppress NEMPI, with increasing Coriolis number up to the values where the system reaches the dynamo threshold, the dynamo instability activates and causes an increase in the growth rate. This dynamo instability is an α^2 mean-field dynamo with a known Beltrami-like large-scale magnetic field, with an x component that has a 90° phase shift relative to the y component of the magnetic field (see Figure 4.4). To calculate the related dynamo number of this system,

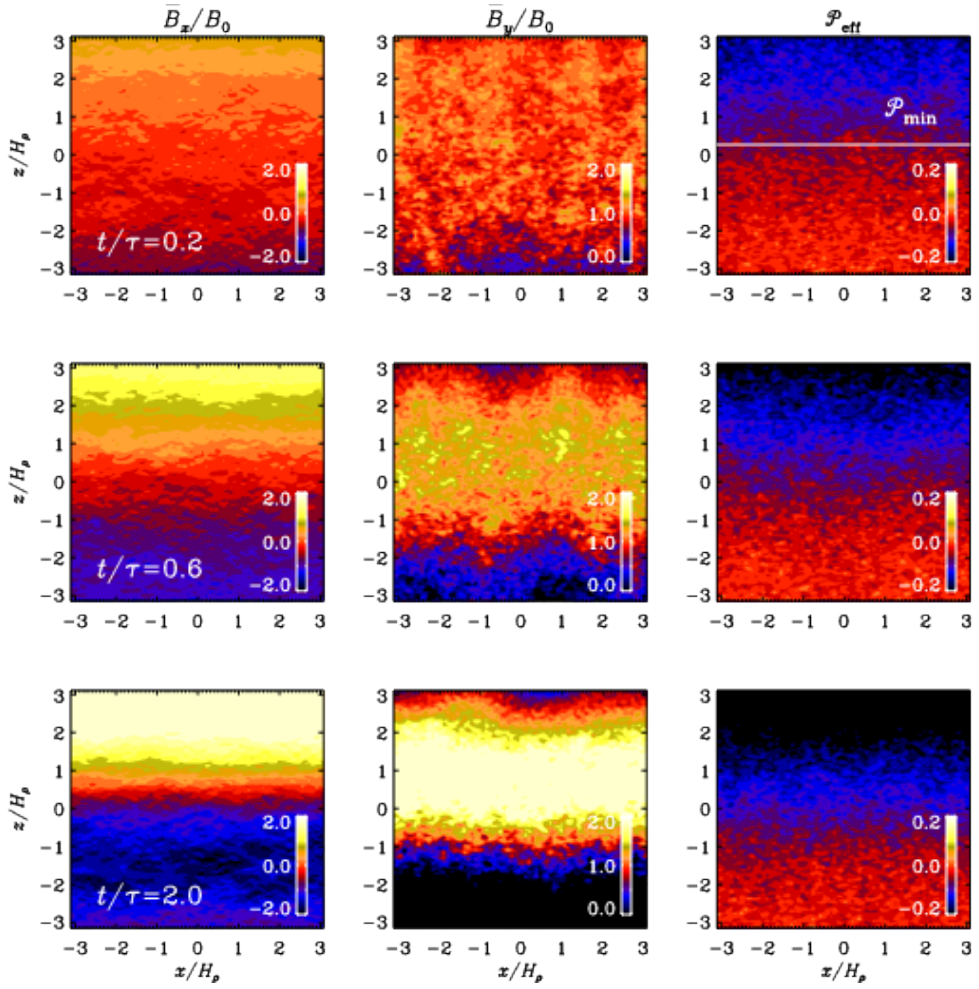

Figure 4.4: Visualization of $\overline{B}_x/B_{\rm eq0}$ and $\overline{B}_y/B_0$ together with effective magnetic pressure for different times. Here $\Omega = 0.15$, Co $= 0.09$, Gr $= 0.033$, and $k_{\rm f}/k_1 = 30$.

two different approaches were used: the formulation presented in Chapter 2 and TFM, which was already explained in section 2.4.

The estimated value for alpha is close to the value computed by TFM, but if one compares our coefficients with earlier works, there is a small difference. In fact, our results are somewhat larger than what was found previously. The only reason can be the fact that we have used larger scale separation (in the present simulations, $k_{\rm f} = 30$ was used, while the largest value used before was 5). To study the effects of changing the gravity parameter, Gr, there are two options. The first one is to keep the turbulent diffusivity constant and change Gr by changing gravity. The other option is to change turbulent diffusivity to change Gr while keep g constant. However, it turned out that our results are independent of whether Gr is changed by changing g or η_t (see Figure 4.5).

Figure 4.6 shows a comparison between the growth rate for the coupled system of

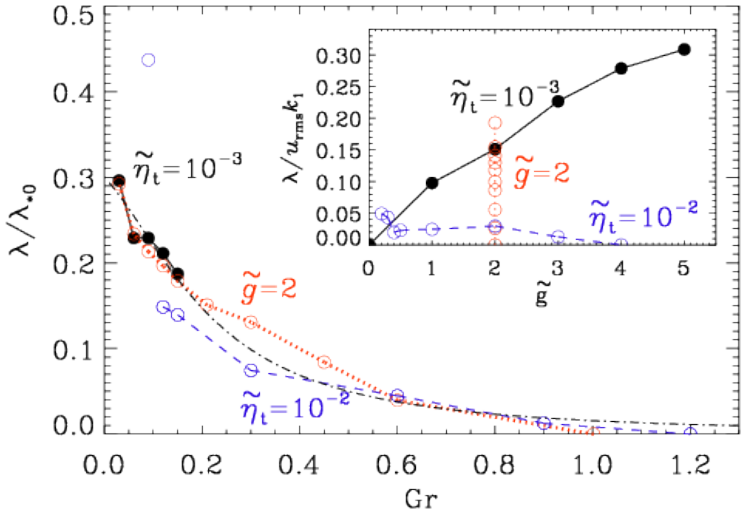

Figure 4.5: Normalized growth rate of NEMPI versus stratification parameter Gr that varies with changing gravity, g, for Co $= 0$, constant $\tilde{\eta}_t$ ($\tilde{\eta}_t = 10^{-3}$ black, filled symbols and $\tilde{\eta}_t = 10^{-2}$ blue, open symbols), or it changes with different $\eta_t = \nu_t$ for constant $\tilde{g} = 2$ (red, open symbols). The dash-dotted line shows the approximate fit given by $\lambda/\lambda_{*0} \approx 0.3/\left[1 + 2\mathrm{Gr} + (4\mathrm{Gr})^2\right]$. The inset shows the growth rate normalized by the turnover time as a function of $\tilde{g}$.

dynamo and NEMPI together with those of a pure dynamo for the same values of the gravitational parameter. The behavior of the growth rate for both instabilities is same, but the position of the minimum in the growth rate moves toward larger values of Co. The minimum indicates the values of Co where α^2 mean-field dynamo action sets in.

4.2.3 New developments

This work has increased our understanding of the action of NEMPI together with a dynamo in the presence of rotation. What we have learned here can be used for further studies. For instance, there is now a project by Mitra et al. (2014) concerning a dynamo-generated magnetic field which is used to excite NEMPI in plane geometry. One difference is the absence of rotation and another difference is that their dynamo acts just in a limited part of the simulation box (at the bottom of the box) and not in the whole domain like in our study. Preliminary results show that in the location where the dynamo acts there are large-scale structures and in the upper part of the domain there is a bipolar region, which may be due to NEMPI. This work is still under study.

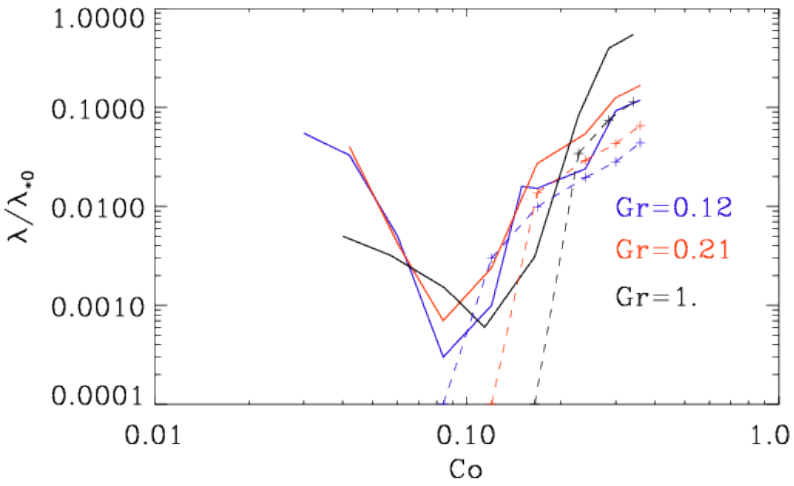

Figure 4.6: Normalized growth rate of the combined NEMPI and dynamo instability (solid lines) together with cases with pure dynamo instability (no imposed field, dashed lines) versus Co for three different value of Gr, Gr = 0.12 (blue) and Gr = 0.21 (red) and Gr = 1.0 (black). In these simulations $\tilde{g} = 4$ and $\tilde{\eta}_t = 10^{-3}$ (blue line), $\tilde{g} = 3.5$, $\tilde{\eta}_t = 2 \times 10^{-3}$ (red line) and $\tilde{g} = 3.5$, $\tilde{\eta}_t = 9.5 \times 10^{-3}$ (black line).

Chapter 5

Flux tube structure, NEMPI and vertical magnetic field

As mentioned before, one of the important achievements in studying NEMPI was the formation of a magnetic spot in DNS (Brandenburg et al., 2013). The main difference between this work and previous investigations of NEMPI is the presence of a weak *vertical* magnetic field as an imposed field. For the case with a horizontal imposed field, the resulting magnetic field is of the order of 10% of the equipartition value, but in the simulations with vertical imposed field they have found magnetic fields even larger than the equipartition value. They explained this phenomenon by using the concept of the potato sack effect. In the case of NEMPI with horizontal initial field, the magnetic flux has larger density with respect to its surrounding, so it sinks down and takes the structure with it. This leads to the saturation of the instability. For a vertical imposed field, however, this effect does not exist, because the heavier flow sinks in the direction of field lines, so it does not affect the magnetic field concentration. This makes the structure remain longer in the area where NEMPI is working, so it gets larger magnetic field. They also have shown that, even in the case of a vertical magnetic field, the depth where NEMPI occurs varies when the strength of the imposed field changes. In fact, it increases by increasing the strength of the initial field. In the other hand, the magnitude of the resulting magnetic field, which is calculated in units of the equipartition field, decreases with depth. Another finding related to the vertical imposed field was that the size of the spot depends on the value of the imposed field. These important findings for a vertical imposed field together with the interest in explaining the formation of active regions and sunspots using NEMPI, led us to investigate more about NEMPI, which is driven by a vertical imposed field.

5.1 Magnetic flux concentrations from vertical field

5.1.1 Outline of the model

In this study we simulate highly stratified forced turbulence in an isothermal layer without radiation. The aim of this work is to investigate the properties of NEMPI for a vertical imposed field. For this reason we used both MFS and DNS. In MFS, we used cylindrical

coordinates, which allows us to transform our problem into an axisymmetric one.

We used two different codes; Pencil Code, which previously was shown to be successful in studying NEMPI and another code called NIRVANA, which was used for implicit large eddy simulations (ILES). The main difference between these two codes is the fact that ILES does not include any explicit physical dissipation coefficients. This is useful because one can do simulations with higher Mach numbers without being constrained by heavy and expensive simulations at high resolution that would otherwise be required. In this setup, like in many others used for DNS of NEMPI, the stratification is uniform, which means that the density scale height is independent of height. Using such a system, we want to investigate the effects of changing the aspect ratio, gravity, Mach number, scale separation, and other properties regarding the onset and nonlinear development of NEMPI. We also study the parameter sensitivity of NEMPI. In the next section, I will present the main results of this study.

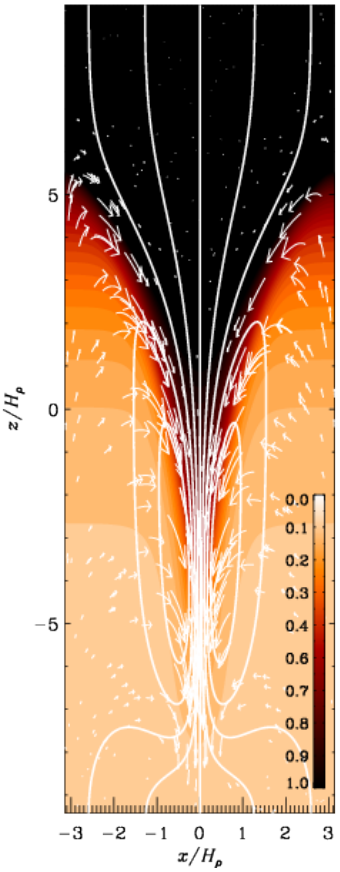

Figure 5.1: $\overline{B}_z/B_{\rm eq}$ together with field lines and flow vectors from MFS. (Taken from Figure 5 of Paper III.)

5.1.2 Major results of Paper III

Let us start with the MFS results. In the case of vertical imposed field, we find a cellular pattern for magnetic field. When we change the aspect ratio, we find that the number of cells per unit area is independent of the size of the domain (see Figure 1 of Paper III).

By considering the magnetic field profile during saturation, we obtain a slender tube with an aspect ratio of about 1:8. By changing the magnitude of the imposed field, the position of the structure moves along the vertical direction while the shape of the flux tube does not vary (see Figure 4 of Paper III). In fact when we increase the strength of imposed field, the structure moves downward. This is in agreement with Brandenburg et al. (2013). As one sees in Figure 5.1, there is an inflow into the tube along magnetic field lines at the lower depth while there is an outflow at higher depth. It is because of this inflow that the flux tube remains concentrated.

For the case with smaller scale separation, again the position of the structure changes, but this time it moves upward. The reason is the fact that scale separation is proportional

to the inverse turbulence diffusion coefficient. This means that, by decreasing the scale separation, we increase the diffusivity, which leads to a weaker field concentration. A weaker field concentration has a smaller magnetic pressure and, following the pressure conservation rule, we will have a smaller gas pressure, too. Smaller gas pressure results in smaller density, which means the structure will sink less (see Figure 7 of Paper III).

As discussed in Chapter 3, we know that there are two parameters $\beta_\star$ and β_p that determine the dependency of the coefficient q_p on the magnetic field; see Equation (3.10). Here we also study the sensitivity of NEMPI on these two parameters. Figures 9–11 of Paper III show the result of this study. For small $\beta_\star$ we obtain a fatter structure while for a big value the structure becomes thinner. On the other hand, when β_p is small the structure is shorter and for larger β_p, the structure is taller.

As was studied before, for a horizontal imposed field, we also investigated the effect of rotation on NEMPI for this new setup with a vertical imposed field. Similar to previous work employing a horizontal magnetic field (Losada et al., 2012, 2013), we find that NEMPI is being suppressed by rotation and, at the same time, the structure moves upward and becomes fatter for a vertical imposed field (see Figure 12 of Paper III). Finally, our DNS results show that an increase of the imposed field leads to an increase of the resulting magnetic field strength and also an increase in the radius of the structure. Previous studies of the effects of changing magnetic Prandtl and Reynolds numbers, Pr_M and Re_M, respectively, showed that for $\mathrm{Pr}_M \geq 8$ and $\mathrm{Re}_M \ll 1$, there is no NEMPI. Our DNS confirm that for $\mathrm{Pr}_M \geq 5$ there is no NEMPI, which is consistent with those previous findings. As mentioned before, to study the effect of Mach number it is more convenient to use ILES. It turns out that for the larger Mach number, the structure becomes smaller. In other words, for larger Mach number the structure forms in the upper layer, so it cannot be fully contained in our domain. That is why we see smaller magnetic structures. Figures 5.2 and 5.3 illustrate the formation of structure at the upper surface by performing DNS and ILES, respectively. Note that there is good agreement between the results of DNS and ILES. This is important because in ILES we ignore explicit dissipative terms, which means that the Reynolds number is not known, but perhaps much larger than before. Our results indicate that NEMPI is independent of the details of the Reynolds number.

5.1.3 Outlook

This study is significant in the sense that it results in the formation of a magnetic flux tubes due to NEMPI. Our detailed analysis shows that NEMPI operates only in the deeper parts of the tube, but it has an effect much higher up because the negative magnetic pressure leads to downward suction which concentrates the field also higher up. The results of this research are useful for future studies of NEMPI with an imposed vertical field. One of the works related to this study is discussed in the next section where we use DNS to calculate the coefficients, q_p, q_s, and q_g for the case of a vertical field. We expect to find the better relation between q_p and initial field.

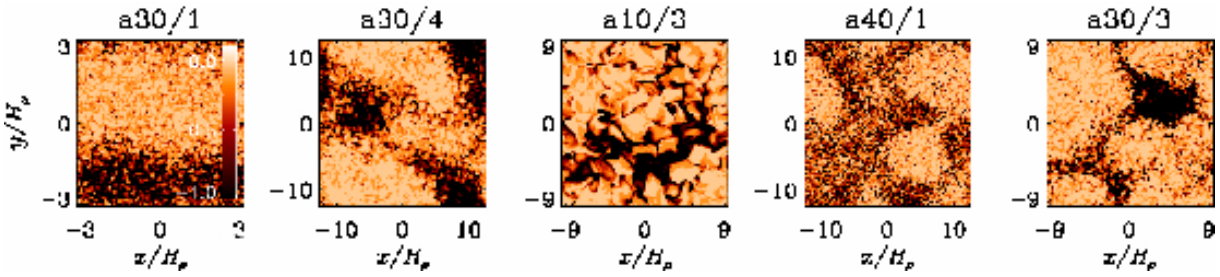

Figure 5.2: Magnetic field configuration at the upper surface for various DNS Runs a30/1 etc denoting the forcing forcing wavenumber (e.g., 10, 30, or 40), and the value of gravity (e.g., 1, 3, or 4); see Table 5 of Paper III for further details.

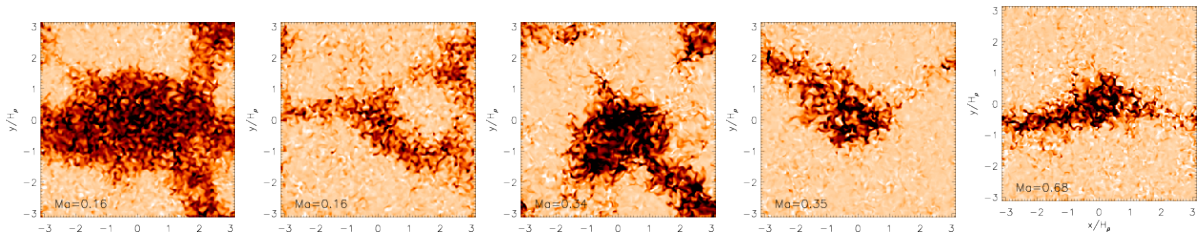

Figure 5.3: Surface appearance of the vertical magnetic field, $B_z^{\max}$, in ILES with different Mach numbers (from left to right). The color coding shows $B_z^{\max}/B_{\rm eq}$ in the range of -0.1 (white) to $+1.0$ (black). Root-mean-square Mach numbers are given by the labels. For the upper two rows with lower Mach number, the left column is for fixed initial mean field, whereas in the right column the initial field is adjusted between the runs, such that the field strength remains constant relative to the kinetic energy in the background turbulence.

5.2 Parameterization of NEMPI for vertical field

5.2.1 Outline of the model

As I already discussed in Section 3.2, there are coefficients, which determine how the averaged momentum stress tensor will change by mean field, $\overline{B}$. Brandenburg et al. (2012) calculated these coefficients for a *horizontal* imposed field in highly stratified forced turbulence. They found that $q_{\rm p}$ is always positive function of $\overline{B}$, which is consistent with previous studies. It is also a function of z because β is a function of z. This comes from the fact that the equipartition field changes with depth. They used this property to calculate the β dependence of the effective magnetic pressure and also of $\beta_\star$ and $\beta_{\rm p}$ for horizontal imposed field; see Equation (3.10).

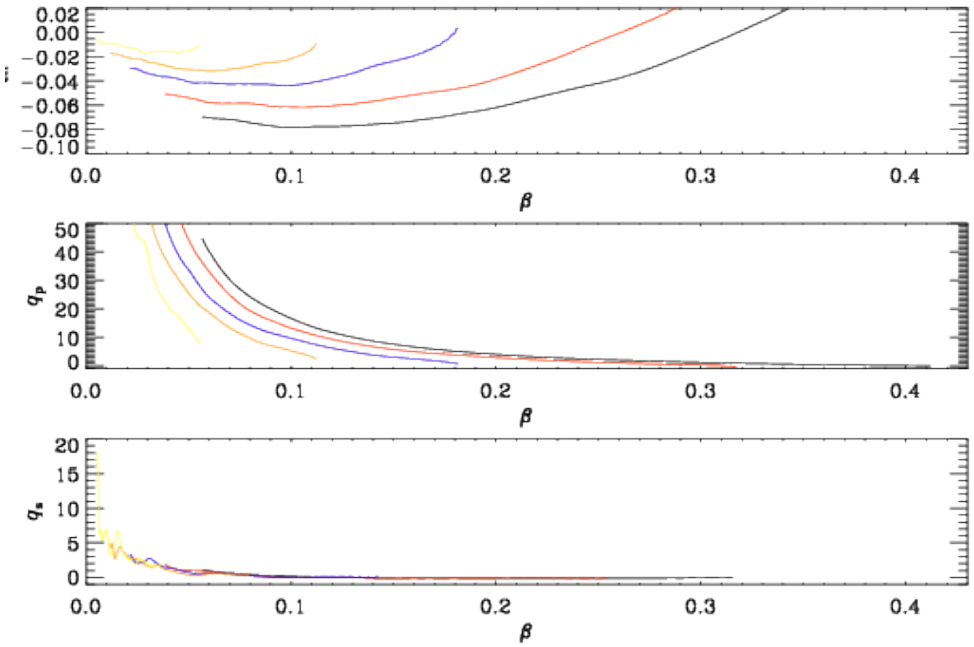

Figure 5.4: Effective magnetic pressure $\mathcal{P}_{\rm eff}$ and transport coefficients $q_{\rm p}$ and $q_{\rm s}$ versus β for different vertical fields ($B_0/B_{\rm eq0} = 0.025$ yellow, 0.05 orange, 0.08 red, 0.14 black, and 0.2 blue).

5.2.2 Major results of this work

The goal is to find out how the parameters $q_{\rm p}$ and $q_{\rm s}$ are affected by imposing a vertical magnetic field. This is the purpose of our ongoing project, which I will present in this section. We adopted the same setup as Brandenburg et al. (2012), except that we used a vertical imposed field and larger scale separation ($k_{\rm f}/k_1 = 30$). Figure 5.4 shows the results of the simulations with vertical field. Different colors illustrate different magnitude of initial field. It can be seen that, similar to the case of horizontal field, $q_{\rm p}$ is always positive and larger than unity, so the effective magnetic pressure is negative. Similar to the horizontal case, $q_{\rm s}$ is very small for large β and for β larger than 0.1, it is zero. For $\beta < 0.05$, however, $q_{\rm s}$ is not small (it is more than 1) but for very small β (< 0.05), the error-bars are large enough so we are not able to determine $q_{\rm s}$ for such small β. As expected, the minimum of the effective magnetic pressure is larger if the imposed field is stronger.

Somewhat surprisingly, the curves for different values of $B_0/B_{\rm eq0}$ do not collapse onto a single one. This is different from the case of a horizontal magnetic field (Brandenburg et al., 2012). The reason for this is not yet clear, but it suggests that there is still an additional explicit z dependence in the model. This work is still in progress and will be the subject of a future paper.

Chapter 6

The next steps

The main goal of studying NEMPI is to use it as a part of a comprehensive research, which explains not just the observed properties of solar active regions and sunspots but also the origin of their formation and evolution. The findings of Papers I and II were our first steps toward a more realistic model by using a dynamo-generated magnetic field to feed the instability. As the results were encouraging, we are now in the process of taking one step further by including ionization and radiative transfer in our model. In this new model we are looking for the formation of structures with sunspot properties. As the results of Paper III already showed that it is possible to reach higher field strengths (even more than the equipartition value), we seek a model which, at the same time, reproduces other important properties of a real sunspot. The purpose of this chapter is to show some of the primary results of this ongoing research.

6.1 Realistic solar simulations

Realistic simulations of the solar atmosphere are done by a number of different groups. I mentioned already the work of Stein & Nordlund (2012), which has a long history starting with a seminal paper by Nordlund (1982) explaining numerical aspects of a realistic model for solving radiation hydrodynamics of the solar atmosphere. One of the early insights resulting from such work include the realization that in the strongly stratified solar convection zone downdrafts merge gradually into larger networks of downdrafts as one goes deeper down (Stein & Nordlund, 1989, 1998). The code used by Stein & Nordlund (2012) works with sixth-order staggered derivatives, which is also the basis of the Bifrost code used by the Oslo group (see, e.g., Leenaarts et al., 2009). Wedemeyer-Böhm et al. (2012) use the CO5BOLD[1] code, which is based on an approximate Riemann solver of Roe type and also incorporates realistic physics. Another code is the MURaM code[2] which goes back to work by Vögler et al. (2005) and is also used in sunspot models of Rempel (2011) and in models of active region formation (Cheung et al., 2010; Rempel & Cheung, 2014). Yet another code is the one used by Kitiashvili et al. (2010), who simulated the spontaneous formation of stable magnetic structures on the Sun from an imposed vertical magnetic field similar to the approach used here. A potential shortcoming of

[1] COnservative COde for the COmputation of COmpressible COnvection in a BOx of L Dimensions
[2] MURaM Code stands for MPAe/UofC Radiation MHD Code

all those models may be an under-representation of turbulence at small scales, especially in the deeper layers which tend to show just a few major downdrafts. Although high resolution simulations of Stein & Nordlund (1998, 2006) suggest that the shear at the edges of downdrafts drives significant amounts of small-scale turbulence, we decided to add explicit small-scale forcing as was also used in Papers II and III.

6.2 Outline of the model

We use a setup similar to that Heinemann et al. (2006, 2007), where gray radiation transport along 6 fixed directions is taken into account, using an opacity that is given by the number of H^- ions times their frequency-averaged cross-section. The source function is given by $\sigma_{\rm SB}T^4$, where $\sigma_{\rm SB}$ is the Stefan-Boltzmann constant and T is temperature. The equation of state is calculated under the assumption that hydrogen is partially ionized, as given by the Saha equation. Unlike the other aforementioned codes, no table lookups are necessary in this still idealized approach. Even though the ionization of other elements such as helium is ignored, and the radiation transport is gray with only a single contributor to the opacity, it is much more realistic than convection simulations that ignore radiation and ionization altogether.

Simulations with realistic value of the opacity are hard because the resulting Rayleigh and Reynolds numbers become huge. For this reason, Barekat & Brandenburg (2014) used strongly reduced opacities in their DNS with the Pencil Code. Another alternative is to add shock viscosities that increase locally in places of strong flow convergence, as it was done by Heinemann et al. (2007), who also used the Pencil Code. In addition, they adopted damping in the top layers to keep the code stable. In those layers, the density becomes very small, so the Alfvén speed becomes huge and begins to limit the length of the time step severely. To avoid this, Heinemann et al. (2007) assumed an artificial "quenching" of the Lorentz force when the Alfvén speed exceeds a certain limit, which is here set to $2500\,{\rm km\,s^{-1}}$. The number of rays used in the radiation transport could be increased to 22, but the resulting changes are minor (cf. Barekat & Brandenburg, 2014).

6.3 Results so far

In our simulations, the typical rms velocity is around $3\,{\rm km\,s^{-1}}$, ranging from $2\,{\rm km\,s^{-1}}$ in the lower part of the domain to about $4\,{\rm km\,s^{-1}}$ at the surface; see the upper panel of Figure 6.1. Furthermore, it can be seen from the lower panel of Figure 6.1 that the equipartition field strength is not constant and increases with depth. This is what we expect from the fact that density increases with depth faster than $u_{\rm rms}^2$ decreases.

In Figure 6.2 we plot the vertical dependence of the optical depth $\tau(x,y,z) = \tau_{\rm top} + \int_{z_{\rm top}}^{z} \kappa\rho\,{\rm d}z'$. At the surface, τ is clearly below unity, so the gas is optically thin. Near the surface, $z = 0$, there is a sharp increase of τ with depth and, as expected, the optical depth becomes very large toward the bottom of our domain. Dotted black lines in this figure

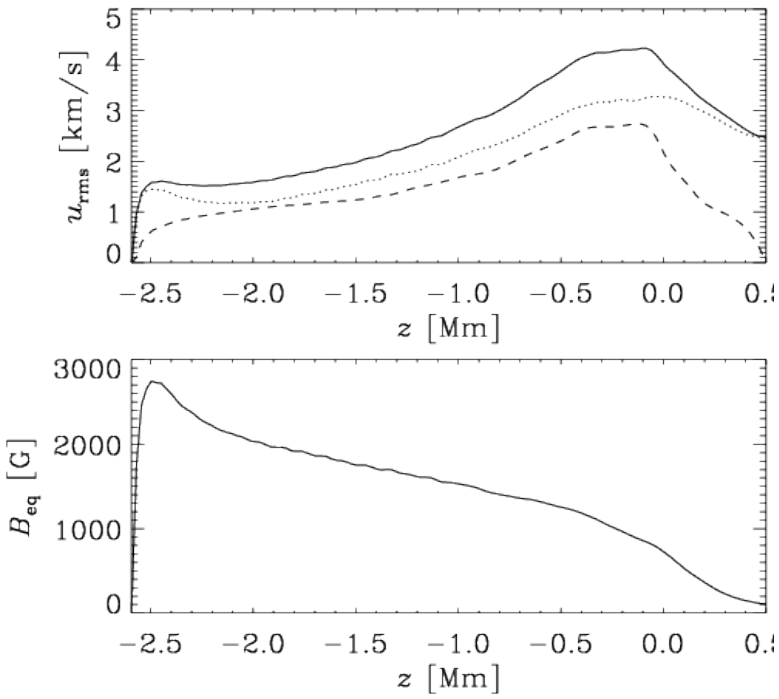

Figure 6.1: The dependency of $u_{\rm rms}$ separately for the horizontal components x (solid line) and y (dotted line) as well as the vertical component (dashed) in the upper panel and the equipartition magnetic field strength $B_{\rm eq}$ as a function of depth in the lower panel.

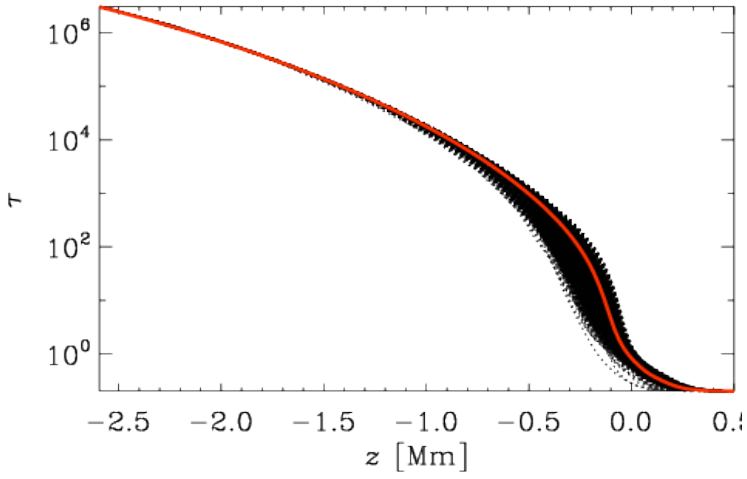

Figure 6.2: Optical depth as a function of z. Dotted black lines are the τ curves in different xy locations and the red line represents the horizontal average.

represent the optical depth function in different xy locations. The mean stratification is convectively unstable and remains highly dynamic.

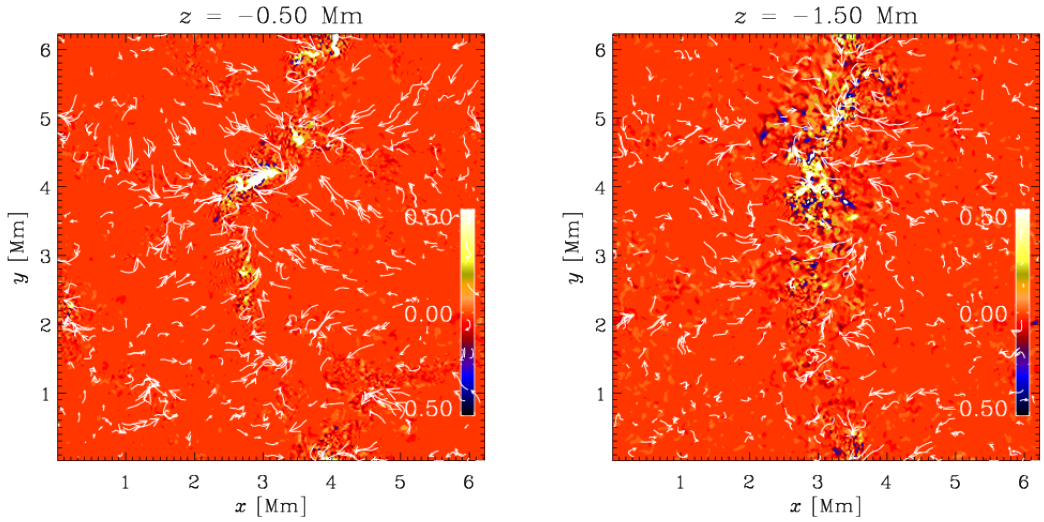

Figure 6.3: Vertical magnetic field component and velocity vectors in the xy plane for two depths ($z = -0.5\,\mathrm{Mm}$ left panel and $z = -1.5\,\mathrm{Mm}$ right panel).

A uniform vertical magnetic field is imposed. It gets advected into intergranular lanes where it becomes strongly amplified to field strengths of the order of up to five times the local equipartition field strength. In Figure 6.3 we show the formation of a spot like structure near the surface. The two different panels are for two different depths. Figure 6.4 shows the z component of the magnetic field in xz plane. Here one can see the large-scale circulation of velocity The thick blue line presents the position of the $\tau = 0$ surface. It can be seen that in the area with the magnetic field concentration this surface lies in lower layer. This is due to the Wilson depression (see Chapter 1.5).

Figure 6.5 is a zoomed demonstration of magnetic and velocity fields in the area where the structure forms. Here, the left panel shows large values of $|B_z|$ as dark shades together with vectors of the horizontal components of the magnetic field.

We need to find the best parameter regime in this model for which extended structures can form that consist of many turbulent eddies and are not just small concentrations of flux into individual downdrafts, which is similar to what was found by Kitiashvili et al. (2010). These were only the first steps toward investigating NEMPI with more realistic models and there are many more that one still can follow. Using a solar parameter regime, more realistic boundary conditions and combining NEMPI with other possible mechanisms is the main purpose of future work. For instance to achieve a more realistic model, we need to have higher Reynolds numbers and larger scale separations, i.e., a larger domain. On the other hand, high Reynolds numbers require higher resolution. The Reynolds number of the Sun (about 10^{11}) is impossible to reach, but by using more computing power to reach larger Reynolds numbers, we hope to be able to draw meaningful conclusions about solar surface activity and sunspots.

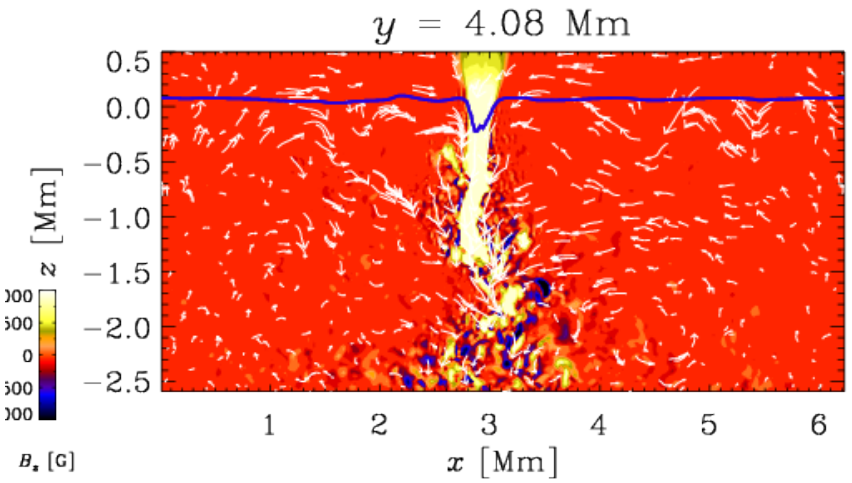

Figure 6.4: Vertical magnetic field component and velocity vectors in xz plane. There is a NEMPI-like structure near the surface (at $z = 0.5\,\mathrm{Mm}$).

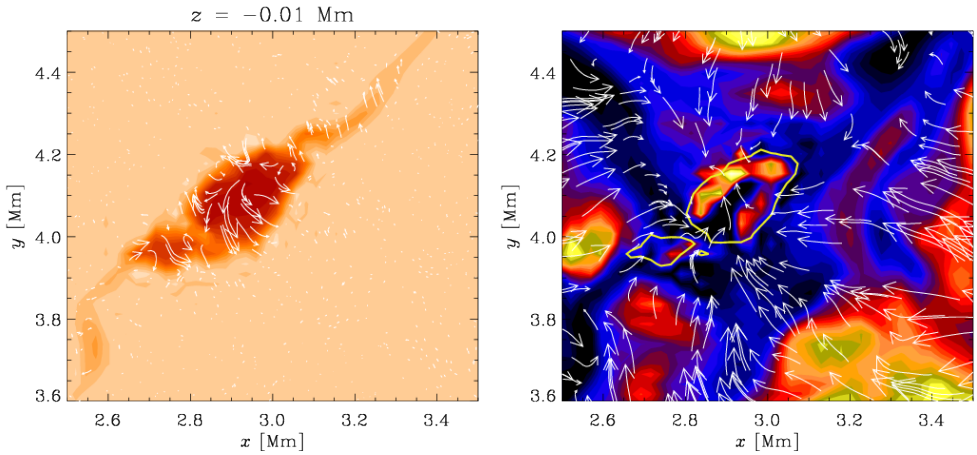

Figure 6.5: Vertical magnetic field component (large values are shown as dark shades) together with vectors of the horizontal components of the field in xy plane at the surface (left panel) and vertical velocity component together with the parallel components of the vectors in the same xy plane (right panel). The single yellow contour in the right panel presents the magnetic field at the 1000 G level.

My contribution to the papers

In Paper I, nearly all of the MFS simulations were performed and analyzed by me. The evaluation of the simulation results was done together with the other authors. I played an active role in the discussion of the content of the text and in the adaptations following the referee reports. Paper II is a follow up of Paper I and was completely conducted by me. I performed all the simulations both DNS and MFS and produced all plots of the paper. I wrote some sections in the paper, although they were largely rewritten and extended by the senior coauthors.

My contribution to Paper III was mostly through running both mean-field and direct numerical simulations. Findings from these simulations were then more rigorously analyzed by Axel, who also wrote most of the text in the paper. I also participated in the analysis of the result and produced some plots and tables of the paper.

Acknowledgments

I would like to thank my supervisor Axel for his guidance, understanding, patience, and most importantly, his friendship during my PhD studies until now. I also would like to thank all the members of Axel's research group for giving me the opportunity to act as a member of the group, guiding and helping me not just in science but also in life and for their friendship. I would like to express my deepest gratitude to Dhruba, Igor, Nathan and Matthias for their useful discussions. I am grateful to all students and staff members at Nordita and the Department of Astronomy, especially Sandra and Hans for always being there for me with solutions for all kinds of problems. I also want to express my gratitude to the examiner committee for their valuable time, useful input, discussions and accessibility. Finally, and most importantly, I would like to thank Gianni for his support, encouragement and patience.

Bibliography

Archontis, V., "Magnetic flux emergence and associated dynamic phenomena in the Sun," *Phil. Trans. Roy. Soc. A* **370**, 3088-3113 (2012).

Archontis, V., Hood, A. W. & Tsinganos, K., "The Emergence of Weakly Twisted Magnetic Fields in the Sun," *Astrophys. J.* **778**, 42 (2013).

Barekat, A., & Brandenburg, A., "Near-polytropic simulations with a radiative surface," *Astron. Astrophys.*, submitted (2014).

Brandenburg, A., "Turbulence and its parameterization in accretion discs," *Astron. Nachr.* **326**, 787-797 (2005).

Brandenburg, A., Chatterjee, P., Del Sordo, F., Hubbard, A., Käpylä, P. J., & Rheinhardt, M., "Turbulent transport in hydromagnetic flows," *Phys. Scr.* **T142**, 014028 (2010).

Brandenburg, A., Kleeorin, N., & Rogachevskii, I., "Large-scale magnetic flux concentrations from turbulent stresses," *Astron. Nachr.* **331**, 5-13 (2010).

Brandenburg, A., Kemel, K., Kleeorin, N., Mitra, D., & Rogachevskii, I., "Detection of negative effective magnetic pressure instability in turbulence simulations," *Astrophys. J. Lett.* **740**, L50 (2011)

Brandenburg, A., Kemel, K., Kleeorin, N., & Rogachevskii, I., "The negative effective magnetic pressure in stratified forced turbulence," *Astrophys. J.* **749**, 179 (2012).

Brandenburg, A., Kleeorin, N., & Rogachevskii, I., "Self-assembly of shallow magnetic spots through strongly stratified turbulence," *Astrophys. J.* **776**, L23 (2013).

Cheung, M. C. M., Rempel, M., Title, A. M., & Schüssler, M., "Simulation of the formation of a solar active region," *Astrophys. J.* **720**, 233-244 (2010).

Cheung, M. C. M., Schüssler, M., Tarbell, T. D., & Title, A. M., "Solar Surface Emerging Flux Regions: A Comparative Study of Radiative MHD Modeling and Hinode SOT Observations," *Astrophys. J.* **687**, 1373-1387 (2008).

Choudhuri, A., R., & D'Silva, S., "Influence of turbulence on rising flux tubes in the solar convection zone," *Astron. Astrophys.* **239**, 326-334 (1990).

D'Silva, S., & Choudhuri, A. R., "A theoretical model for tilts of bipolar magnetic regions," *Astron. Astrophys.* **272**, 621-633 (1993).

Evershed, J., "Radial movement in sun-spots," *Month. Not. Roy. Astron. Soc.* **69**, 454-457 (1909).

Fan, Y., "The emergence of a twisted Ω-tube into the solar atmosphere," *Astrophys. J.* **554**, L111-L114 (2001).

Fan, Y., "Magnetic Fields in the Solar Convection Zone," *Living Rev. Solar Phys.* **6**, 4 (2009).

Hale, G. E., "Solar vortices," *Astrophys. J.* **28**, 100-116 (1908a).

Hale, G. E., "On the Probable Existence of a Magnetic Field in Sunspots," *Astrophys. J.* **28**, 315-343 (1908b).

Hale, G. E., "The Magnetic Polarity of Sun-Spots," *Astrophys. J.* **49**, 153-178 (1919).

Heinemann, T., Dobler, W., Nordlund, Å., & Brandenburg, A., "Radiative transfer in decomposed domains," *Astron. Astrophys.* **448**, 731-737 (2006).

Heinemann, T., Nordlund, Å., Scharmer, G. B., & Spruit, H. C., "MHD simulations of penumbra fine structure," *Astrophys. J.* **669**, 1390-1394 (2007).

Hood, A. W., Archontis, V. & MacTaggart, D., "3D MHD Flux Emergence Experiments: Idealised Models and Coronal Interactions," *Solar Phys.* **278**, 3-31 (2012).

Käpylä, P. J., Brandenburg, A., Kleeorin, N. I., Mantere, M. J., & Rogachevskii, I., "Negative effective magnetic pressure in turbulent convection," *Month. Not. Roy. Astron. Soc.* **422**, 2465-2473 (2012).

Kemel, K., Brandenburg, A., Kleeorin, N., Mitra, D., & Rogachevskii, I., "Active region formation through the negative effective magnetic pressure instability," *Solar Phys.* **287**, 293-313 (2013b).

Kemel, K., Brandenburg, A., Kleeorin, N., Mitra, D., & Rogachevskii, I., "Spontaneous formation of magnetic flux concentrations in stratified turbulence," *Solar Phys.* **280**, 321-333 (2012b).

Kemel, K., Brandenburg, A., Kleeorin, N., & Rogachevskii, I., "Properties of the negative effective magnetic pressure instability," *Astron. Nachr.* **333**, 95-100 (2012a).

Kemel, K., Brandenburg, A., Kleeorin, N., & Rogachevskii, I., "Non-uniformity effects in the negative effective magnetic pressure instability," *Phys. Scr.* **T155**, 014027 (2013a).

Kitchatinov, L. L. & Mazur, M. V., "Stability and equilibrium of emerged magnetic flux," *Solar Phys.* **191**, 325-996 (2000).

Kitiashvili, I. N., Kosovichev, A. G., Wray, A. A., & Mansour, N. N., "Mechanism of spontaneous formation of stable magnetic structures on the Sun," *Astrophys. J.* **719**, 307-719 (2010).

Kleeorin, N., & Rogachevskii, I., "Effective Ampere force in developed magnetohydrodynamic turbulence," *Phys. Rev. E* **50**, 2716-2730 (1994).

Kleeorin, N., Rogachevskii, I., & Ruzmaikin, A. A., "Negative magnetic pressure as a trigger of large-scale magnetic instability in the solar convective zone," *Sov. Astron.* **15**, 274-276 (1989).

Kleeorin, N., Rogachevskii, I., & Ruzmaikin, A. A., "Magnetic force reversal and instability in a plasma with advanced magnetohydrodynamic turbulence," *Sov. Phys. JETP* **70**, 878-883 (1990).

Kleeorin, N., Mond, M., & Rogachevskii, I., "Magnetohydrodynamic instabilities in developed small-scale turbulence," *Phys. Fluids B* **5**, 4128-4134 (1993).

Kleeorin, N., Mond, M., & Rogachevskii, I., "Magnetohydrodynamic turbulence in solar convective zone as a source of oscillations and sunspot formation," *Astron. Astrophys.* **307**, 293-309 (1996).

Leenaarts, J., Carlsson, M., Hansteen, V., & Rouppe van der Voort, L., "Three-dimensional non-LTE radiative transfer computation of the Ca 8542 infrared line from a radiation-MHD simulation," *Astrophys. J. Lett.* **694**, L128-L131 (2009).

Losada, I. R., Brandenburg, A., Kleeorin, N., Mitra, D., & Rogachevskii, I., "Rotational effects on the negative magnetic pressure instability," *Astron. Astrophys.* **548**, A49 (2012).

Losada, I. R., Brandenburg, A., Kleeorin, N., & Rogachevskii, I., "Competition of rotation and stratification in flux concentrations," *Astron. Astrophys.* **556**, A83 (2013).

Mestel, L. *Stellar Magnetism*. Clarendon Press, Oxford (1999).

Meyer, F., & Schmidt, H. U., "A model for the Evershed flow in sunspots," *Astrophys. J.* **25**, 194-197 (1968).

Mitra, D., Brandenburg, A., Kleeorin, N., & Rogachevskii, I., "Intense bipolar structures from stratified helical dynamos," *Month. Not. Roy. Astron. Soc.*, submitted, arXiv:1404.3194 (2014).

Moffatt, H. K. *Magnetic Field Generation in Electrically Conducting Fluids*. Cambridge: Cambridge Univ. Press (1978).

Nordlund, Å., "Numerical Simulations of the Solar Granulation I. Basic Equations and Methods," *Astron. Astrophys.* **107**, 1-10 (1982).

Parker, E. N., "The Formation of Sunspots from the Solar Toroidal Field," *Astrophys. J.* **121**, 491-507 (1955a).

Parker, E. N., "Hydromagnetic Dynamo Models," *Astrophys. J.* **122**, 293-314 (1955b).

Parker, E. N., "The origin of solar activity," *Ann. Rev. Astron. Astrophys.* **15**, 45-68 (1977).

Parker, E. N., "Hydraulic concentration of magnetic fields in the solar photosphere. Adiabatic cooling and concentration in downdrafts," *Astrophys. J.* **221**, 368-377 (1978).

Parker, E. N., "Sunspots and the physics of magnetic flux tubes. The general nature of the sunspots. Aerodynamic drag," *Astrophys. J.* **230**, 905-923 (1979).

Parker, E. N., "Depth of origin of solar active regions," *Astrophys. J.* **280**, 423-427 (1984).

Rempel, M., "Subsurface magnetic field and flow structure of simulated sunspots," *Astrophys. J.* **740**, 15 (2011).

Rempel, M., & Cheung, M. C. M., "Numerical simulations of active region scale flux emergence: From spot formation to decay," *Astrophys. J.* **785**, 90 (2014).

Rempel, M., Schüssler, M., & Knölker, M., "Radiative Magnetohydrodynamic Simulation of Sunspot Structure," *Astrophys. J.* **691**, 640-649 (2009).

Rempel, M., & Schlichenmaier, R., "Sunspot modeling: From simplified models to radiative MHD simulations," *Living Rev. Solar Phys.* **8**, 3 (2011).

Rogachevskii, I., & Kleeorin, N., "Magnetic fluctuations and formation of large-scale inhomogeneous magnetic structures in a turbulent convection," *Phys. Rev. E* **76**, 056307 (2007).

Ruzmaikin, A., "Origin of sunspots," *Spa. Sci. Rev.* **95**, 43-53 (2001).

Scharmer, G. B., Nordlund, Å., & Heinemann, T., "Convection and the origin of Evershed flows in sunspot penumbrae," *Astrophys. J.* **677**, L149-L152 (2008).

Scharmer, G. B., "Recent Evidence for Convection in Sunspot Penumbrae," *Spa. Sci. Rev.* **144**, 229-247 (2009).

Scharmer, G. B., Henriques, V. M. J., Kiselman, D., & Rodrígue, J, "Detection of Convective Downflows in a Sunspot Penumbra," *Science* **333**, 316-319 (2011).

Schlichenmaier, R., "Penumbral fine structure: Theoretical understanding," *Astron. Nachr.* **323**, 303-308 (2002).

Schlichenmaier, R., "Sunspots: From small-scale inhomogeneities towards a global theory," *Spa. Sci. Rev.* **144**, 213-228 (2009).

Schlichenmaier, R., Jahn, K., & Schmidt, H. U., "A Dynamical Model for the Penumbral Fine Structure and the Evershed Effect in Sunspots," *Astrophys. J.* **493**, L149-L121 (1998).

Schrinner, M., Rädler, K.-H., Schmitt, D., Rheinhardt, M., & Christensen, U., "Mean-field view on rotating magnetoconvection and a geodynamo model," *Astron. Nachr.* **326**, 245-249 (2005).

Schrinner, M., Rädler, K.-H., Schmitt, D., Rheinhardt, M., & Christensen, U. R., "Mean-field concept and direct numerical simulations of rotating magnetoconvection and the geodynamo," *Geophys. Astrophys. Fluid Dynam.* **101**, 81-116 (2007).

Spruit, H. C., "Convective collapse of flux tubes," *Solar Phys.* **61**, 363-378 (1979).

Spruit, H. C., "Theories of the solar cycle and its effect on climate," *Progr. Theor. Phys. Suppl.* **195**, 185-200 (2012).

Spruit, H. C., Zweibel, E. G., "Convective instability of thin flux tubes," *Solar Phys.* **62**, 15-22 (1979).

Stein, R. F., & Nordlund, Å., "Topology of convection beneath the solar surface," *Astrophys. J. Lett.* **342**, L95-L98 (1989).

Stein, R. F., & Nordlund, Å., "Simulations of solar granulation: I. General properties," *Astrophys. J.* **499**, 914-933 (1998).

Stein, R. F., & Nordlund, Å., "Solar small-scale magnetoconvection," *Astrophys. J.* **642**, 1246-1255 (2006).

Stein, R. F., & Nordlund, Å., "On the formation of active regions," *Astrophys. J. Lett.* **753**, L13 (2012)

Stix, M. *The Sun: An Introduction.* Springer, Germany (2002).

Thomas, J. H., "Siphon flows in isolated magnetic flux tubes," *Astrophys. J.* **333**, 407-419 (1988).

Vögler, A., Shelyag, S., Schüssler, M., Cattaneo, F., Emonet, T., & Linde, T., "Simulations of magneto-convection in the solar photosphere. Equations, methods, and results of the MURaM code," *Astron. Astrophys.* **429**, 335-351 (2005).

Warnecke, J., Losada, I., Brandenburg, A., Kleeorin, N., & Rogachevskii, I., "Bipolar magnetic structures driven by stratified turbulence with a coronal envelope," *Astrophys. J.* **777**, L37 (2013).

Wedemeyer-Böhm, S., Scullion, E., Steiner, O., Rouppe van der Voort, L., de La Cruz Rodriguez, J., Fedun, V., & Erdélyi, R., "Magnetic tornadoes as energy channels into the solar corona," *Nature* **486**, 505-508 (2012).

Zahn, J.-P., Brun, A. S., Mathis, S., "On magnetic instabilities and dynamo action in stellar radiation zones," *Astron. Astrophys.* **474**, 145-154 (2007).

Zwaan, C., "On the appearance of magnetic flux in the solar photosphere," *Solar Phys.* **60**, 213-240 (1978).

Zwaan, C., "The emergence of magnetic flux," *Solar Phys.* **100**, 397-414 (1985).

Zwaan, C., "Elements and patterns in the solar magnetic field," *Ann. Rev. Astron. Astrophys.* **25**, 83-111 (1987).

I

A&A 556, A106 (2013)
DOI: 10.1051/0004-6361/201321353

Astronomy & Astrophysics

Surface flux concentrations in a spherical α^2 dynamo

S. Jabbari[1,2], A. Brandenburg[1,2], N. Kleeorin[1,3,4], D. Mitra[1], and I. Rogachevskii[1,3,4]

[1] Nordita, KTH Royal Institute of Technology and Stockholm University, Roslagstullsbacken 23, 10691 Stockholm, Sweden
e-mail: sarajab@kth.se
[2] Department of Astronomy, AlbaNova University Center, Stockholm University, 10691 Stockholm, Sweden
[3] Department of Mechanical Engineering, Ben-Gurion University of the Negev, POB 653, 84105 Beer-Sheva, Israel
[4] Department of Radio Physics, N. I. Lobachevsky State University of Nizhny Novgorod, Russia

Received 23 February 2013 / Accepted 31 May 2013

ABSTRACT

Context. In the presence of strong density stratification, turbulence can lead to the large-scale instability of a horizontal magnetic field if its strength is in a suitable range (around a few percent of the turbulent equipartition value). This instability is related to a suppression of the turbulent pressure so that the turbulent contribution to the mean magnetic pressure becomes negative. This results in the excitation of a negative effective magnetic pressure instability (NEMPI). This instability has so far only been studied for an imposed magnetic field.
Aims. We want to know how NEMPI works when the mean magnetic field is generated self-consistently by an α^2 dynamo, whether it is affected by global spherical geometry, and whether it can influence the properties of the dynamo itself.
Methods. We adopt the mean-field approach, which has previously been shown to provide a realistic description of NEMPI in direct numerical simulations. We assume axisymmetry and solve the mean-field equations with the Pencil Code for an adiabatic stratification at a total density contrast in the radial direction of $\approx$4 orders of magnitude.
Results. NEMPI is found to work when the dynamo-generated field is about 4% of the equipartition value, which is achieved through strong α quenching. This instability is excited in the top 5% of the outer radius, provided the density contrast across this top layer is at least 10. NEMPI is found to occur at lower latitudes when the mean magnetic field is stronger. For weaker fields, NEMPI can make the dynamo oscillatory with poleward migration.
Conclusions. NEMPI is a viable mechanism for producing magnetic flux concentrations in a strongly stratified spherical shell in which a magnetic field is generated by a strongly quenched α effect dynamo.

Key words. sunspots – Sun: dynamo – turbulence – magnetohydrodynamics (MHD) – hydrodynamics

1. Introduction

The magnetic field of stars with outer convection zones, including that of the Sun, is believed to be generated by differential rotation and cyclonic convection (see, e.g., Moffatt 1978; Parker 1979; Zeldovich et al. 1983; Brandenburg & Subramanian 2005). The latter leads to an α effect, which refers to an important new term in the averaged (mean-field) induction equation, quantifying the component of the mean electromotive force that is aligned with the mean magnetic field (see, e.g., Steenbeck et al. 1966; Krause & Rädler 1980; Brandenburg et al. 2013). However, what is actually observed are sunspots and active regions, and the description of these phenomena is not part of conventional mean-field dynamo theory (see, e.g., Priest 1982; Stix 1989; Ossendrijver 2003; Cally et al. 2003; Stenflo & Kosovichev 2012).

Flux tube models (Parker 1955, 1982, 1984; Spiegel & Weiss 1980; Spruit 1981; Schüssler et al. 1994; Dikpati & Charbonneau 1999) have been used to explain the formation of active regions and sunspots in an ad hoc manner. It is then simply assumed that a sunspot emerges when the magnetic field of the dynamo exceeds a certain threshold just above the bottom of the convection zone for the duration of about a month (Chatterjee et al. 2004). Such models assume the existence of strong magnetic flux tubes at the base of the convection zone. They require magnetic fields with a strength of about 10^5 Gauss (D'Silva & Choudhuri 1993). However, such strong magnetic fields are highly unstable (Arlt et al. 2005) and are also difficult to produce by dynamo action in turbulent convection (Guerrero & Käpylä 2011).

Another possible mechanism for producing magnetic flux concentrations is the negative effective magnetic pressure instability (NEMPI), which can occur in the presence of strong density stratification, i.e., usually near the stellar surface, on scales encompassing those of many turbulent eddies. NEMPI is caused by the suppression of turbulent magnetohydrodynamic pressure (the isotropic part of combined Reynolds and Maxwell stresses) by the mean magnetic field. At large Reynolds numbers, the negative turbulent contribution can become so large that the effective mean magnetic pressure (the sum of turbulent and nonturbulent contributions) is negative. This results in the excitation of NEMPI that causes formation of large-scale inhomogeneous magnetic structures. The instability mechanism is as follows. A rising magnetic flux tube expands, the field becomes weaker, but because of negative magnetic pressure, its magnetic pressure increases, so the density decreases, and it becomes lighter still and rises further. Conversely, a sinking tube contracts, the magnetic field increases, but the magnetic pressure decreases, so the density increases, and it becomes heavier and sinks further. The energy for this instability is supplied by the small-scale turbulence.

By contrast, the free energy in Parker's magnetic buoyancy instability or in the interchange instability in plasma, is drawn from the gravitational field (Newcomb 1961; Parker 1966).

Direct numerical simulations (DNS; see Brandenburg et al. 2011; Kemel et al. 2012a), mean-field simulations (MFS; see Brandenburg et al. 2010, 2012; Kemel et al. 2012b; Käpylä et al. 2012), and earlier analytic studies (Kleeorin et al. 1989, 1990, 1996; Kleeorin & Rogachevskii 1994; Rogachevskii & Kleeorin 2007) now provide conclusive evidence for the physical reality of NEMPI. However, open questions still need to be answered before it can be applied to detailed models of active regions and sunspot formation.

In the present paper we take a first step toward combining NEMPI, which is described well using mean-field theory, with the α effect in mean-field dynamos. To study the dependence of NEMPI on the magnetic field strength, we assume that α is quenched. This allows us to change the magnetic field strength by changing the quenching parameter. We employ spherical coordinates (r, θ, ϕ), with radius r, colatitude θ, and azimuthal angle ϕ. We assume axisymmetry, i.e., $\partial/\partial\phi = 0$. Furthermore, α is a pseudo-scalar that changes sign at the equator, so we assume that α is proportional to $\cos\theta$, where θ is the colatitude (Roberts 1972). We arrange the quenching of α such that the resulting mean magnetic field is in the appropriate interval to allow NEMPI to work. This means that the effective (mean-field) magnetic pressure locally has a negative derivative with respect to increasing normalized field strength (Kemel et al. 2012b), so the mean toroidal magnetic field must be less than about 20% of the equipartition field strength.

The choice of using spherical geometry is taken because the dynamo-generated magnetic field depends critically on the geometry. Therefore, to have a more realistic field structure, we felt it profitable to carry out our investigations in spherical geometry. Guided by the insights obtained from such studies, it will in future be easier to design simpler Cartesian models to address specific questions regarding the interaction between NEMPI and the dynamo instability.

In the calculations presented below we use the Pencil Code[1], which has been used in DNS of magneto-hydrodynamics in spherical coordinates (Mitra et al. 2009) and also in earlier DNS and MFS of NEMPI. Unlike most of the earlier calculations, we adopt an adiabatic equation of state. This results in a stratification such that the temperature declines approximately linearly toward the surface, so the scale height becomes shorter and the stratification stronger toward the top layers. This is done to have a clear segregation between the dynamo in the bulk and NEMPI near the surface, where the stratification is strong enough for NEMPI to operate. The gravitational potential is that of a point mass. This is justified because the mass in the convection zone is negligible compared to the one below. The goal of the present work is to produce reference cases in spherical geometry and to look for new effects of spherical geometry. We begin by describing the basic model.

2. The model

The evolution equations for mean vector potential $\overline{\boldsymbol{A}}$, mean velocity $\overline{\boldsymbol{U}}$, and mean density $\overline{\rho}$, are

$$\frac{\partial \overline{\boldsymbol{A}}}{\partial t} = \overline{\boldsymbol{U}} \times \overline{\boldsymbol{B}} + \alpha \overline{\boldsymbol{B}} - \eta_{\rm T} \overline{\boldsymbol{J}}, \tag{1}$$

$$\frac{{\rm D}\overline{\boldsymbol{U}}}{{\rm D}t} = \frac{1}{\overline{\rho}} \left[\overline{\boldsymbol{J}} \times \overline{\boldsymbol{B}} + \boldsymbol{\nabla}(q_{\rm p} \overline{\boldsymbol{B}}^2/2\mu_0) \right] - \nu_{\rm T} \overline{\boldsymbol{Q}} - \boldsymbol{\nabla} \overline{H}, \tag{2}$$

$$\frac{{\rm D}\overline{\rho}}{{\rm D}t} = -\overline{\rho} \boldsymbol{\nabla} \cdot \overline{\boldsymbol{U}}, \tag{3}$$

where ${\rm D}/{\rm D}t = \partial/\partial t + \overline{\boldsymbol{U}} \cdot \boldsymbol{\nabla}$ is the advective derivative, $\overline{\rho}$ is the mean density, $\overline{H} = \overline{h} + \Phi$ is the mean reduced enthalpy with $\overline{h} = c_{\rm p} \overline{T}$ the mean enthalpy, $\overline{T} \propto \overline{\rho}^{\gamma-1}$ the mean temperature, $\gamma = c_{\rm p}/c_{\rm v}$ is the ratio of specific heats at constant pressure and constant density, respectively, Φ is the gravitational potential, $\eta_{\rm T} = \eta_{\rm t} + \eta$ and $\nu_{\rm T} = \nu_{\rm t} + \nu$ are the sums of turbulent and microphysical values of magnetic diffusivity and kinematic viscosities, respectively, α is the aforementioned coefficient in the α effect, $\overline{\boldsymbol{J}} = \boldsymbol{\nabla} \times \overline{\boldsymbol{B}}/\mu_0$ is the mean current density, μ_0 is the vacuum permeability,

$$-\overline{\boldsymbol{Q}} = \nabla^2 \overline{\boldsymbol{U}} + \tfrac{1}{3} \boldsymbol{\nabla} \boldsymbol{\nabla} \cdot \overline{\boldsymbol{U}} + 2 \overline{\mathsf{S}} \boldsymbol{\nabla} \ln \overline{\rho} \tag{4}$$

is a term appearing in the viscous force, where $\overline{\mathsf{S}}$ is the traceless rate of strain tensor of the mean flow with components $\overline{\mathsf{S}}_{ij} = \frac{1}{2}(\overline{U}_{i,j} + \overline{U}_{j,i}) - \frac{1}{3}\delta_{ij} \boldsymbol{\nabla} \cdot \overline{\boldsymbol{U}}$, and finally $\boldsymbol{\nabla}(q_{\rm p} \overline{\boldsymbol{B}}^2/2\mu_0)$ determines the turbulent contribution to the mean Lorentz force. Here, $q_{\rm p}$ depends on the local field strength (see below). This term enters with a plus sign, so positive values of $q_{\rm p}$ correspond to a suppression of the total turbulent pressure. The net effect of the mean field leads to an effective mean magnetic pressure $p_{\rm eff} = (1 - q_{\rm p}) \overline{\boldsymbol{B}}^2/2\mu_0$, which becomes negative for $q_{\rm p} > 1$, which can indeed be the case for magnetic Reynolds numbers well above unity (Brandenburg et al. 2012).

Following Kemel et al. (2012c), the function $q_{\rm p}(\beta)$ is approximated by

$$q_{\rm p}(\beta) = \frac{q_{\rm p0}}{1 + \beta^2/\beta_{\rm p}^2} = \frac{\beta_\star^2}{\beta_{\rm p}^2 + \beta^2}, \tag{5}$$

where $q_{\rm p0}$, $\beta_{\rm p}$, and $\beta_\star = \beta_{\rm p} q_{\rm p0}^{1/2}$ are constants, $\beta = |\overline{\boldsymbol{B}}|/B_{\rm eq}$ is the modulus of the normalized mean magnetic field, and $B_{\rm eq} = \sqrt{\mu_0 \rho}\, u_{\rm rms}$ is the equipartition field strength.

NEMPI can occur at a depth where the derivative, ${\rm d}p_{\rm eff}/{\rm d}\beta^2$, is negative. Since the spatial variation of β is caused mainly by the increase in density with depth, the value of the mean horizontal magnetic field essentially determines the location where NEMPI can occur. Therefore, the field strength has to be in a suitable range such that NEMPI occurs within the computational domain. Unlike the Cartesian cases investigated in earlier work (Brandenburg et al. 2010, 2012; Kemel et al. 2012c), where it is straightforward to impose a magnetic field, in a sphere it is easier to generate a magnetic field by a mean-field dynamo. This is why we include a term of the form $\alpha \overline{\boldsymbol{B}}$ in the expression for the mean electromotive force (second term on the righthand side of Eq. (1)). When the mean magnetic field is generated by a dynamo, the resulting magnetic field strength depends on the nonlinear suppression of the dynamo. We assume here a simple quenching function for the α effect, i.e.,

$$\alpha(\theta, \beta) = \frac{\alpha_0 \cos\theta}{1 + Q_\alpha \beta^2}, \tag{6}$$

where Q_α is a quenching parameter that determines the typical field strength, which is expected to be on the order of $Q_\alpha^{-1/2} B_{\rm eq}$. The value of Q_α must be chosen large enough so that the nonlinear equilibration of the dynamo process results in a situation such that ${\rm d}p_{\rm eff}/{\rm d}\overline{B}$ is indeed negative within the computational

[1] http://pencil-code.googlecode.com

Table 1. Dependence of the density contrast on the value of $r_\star$.

$r_\star/R$	$H_{\rm p}({\rm top})/R$	$H_{\rm p0}/R$	$\rho_{\rm max}/\rho_{\rm min}$
1.100	3.6×10^{-2}	0.052	1.4×10^{1}
1.010	4.0×10^{-3}	0.023	2.9×10^{2}
1.001	4.0×10^{-4}	0.019	8.9×10^{3}

domain. In analogy with the $\beta_{\rm p}$ parameter in Eq. (5), we can define a parameter $\beta_\alpha = Q_\alpha^{-1/2}$, which will be quoted occasionally.

The strength of the dynamo is also determined by the dynamo number,

$$C_\alpha = \alpha_0 R/\eta_{\rm T}. \tag{7}$$

For our geometry with $0.7 \le r/R \le 1$, the critical value of C_α for the onset of dynamo action is around 18. The excitation conditions for dipolar and quadrupolar parities are fairly close together. This is because the magnetic field is strongest at high latitudes, so the hemispheric coupling is weak. In the following we restrict ourselves to solutions with dipolar parity. We adopt the value $C_\alpha = 30$, so the dynamo is nearly twice supercritical.

As mentioned before, our gravitational potential Φ is that of a point mass. We define Φ such that it vanishes at a radius $r_\star$, i.e.

$$\Phi(r) = -GM\left(\frac{1}{r} - \frac{1}{r_\star}\right), \tag{8}$$

where G is Newton's constant and M is the mass of the sphere. The radial component of the gravitational acceleration is then $g = -GM/r^2$. We adopt an initially adiabatic stratification with $c_{\rm p}\overline{T} = -\Phi(r)$, so $\overline{T}$ vanishes at $r = r_\star$. To avoid singularities, the value of $r_\star$ has to be chosen some distance above $r = R$. The radius $r_\star$ is used to set the density contrast. Table 1 gives the density contrast for different values of $r_\star$. We vary $r_\star$ between $1.001\,R$, which corresponds to our reference model with a density contrast of 8900, and $1.1\,R$, where the density contrast is 14. The pressure scale height is given by

$$H_{\rm p}(r) = \frac{r(1 - r/r_\star)}{n+1}, \tag{9}$$

where $n = 1/(\gamma-1) = 3/2$ is the polytropic index for an adiabatic stratification with $\gamma = 5/3$. The density scale height is $H_\rho = r(1 - r/r_\star)/n$. The initial density profile is given by

$$\overline{\rho}/\rho_0 = (-\Phi/nc_{\rm s0}^2)^n. \tag{10}$$

Radial profiles of $\overline{\rho}/\rho_0$ and the inverse pressure scale height $H_{\rm p0}/H_{\rm p}(r)$, are shown in Fig. 1 for $r_\star/R$ varying between 1.1 and 1.001. Here, $H_{\rm p0} = H_{\rm p}(r_{\rm ref})$ is the pressure scale height at the reference radius $r_{\rm ref} = 0.95\,R$, corresponding to a depth of 35 Mm in the Sun.

The analytic estimate of the growth rate of NEMPI, λ, based on an isothermal layer with $H_{\rm p} = H_\rho = $ const. is given by (Kemel et al. 2012b)

$$\lambda \approx \beta_\star \frac{u_{\rm rms}}{H_{\rm p}} - \eta_{\rm t} k^2. \tag{11}$$

Assume that this equation also applies to the current case where $H_{\rm p}$ depends on r, and setting $k = H_{\rm p0}^{-1}$, the normalized growth rate is

$$\frac{\lambda H_{\rm p0}}{\beta_\star u_{\rm rms}} = \frac{H_{\rm p0}}{H_{\rm p}} - \frac{\eta_{\rm t}}{\beta_\star u_{\rm rms} H_{\rm p0}}. \tag{12}$$

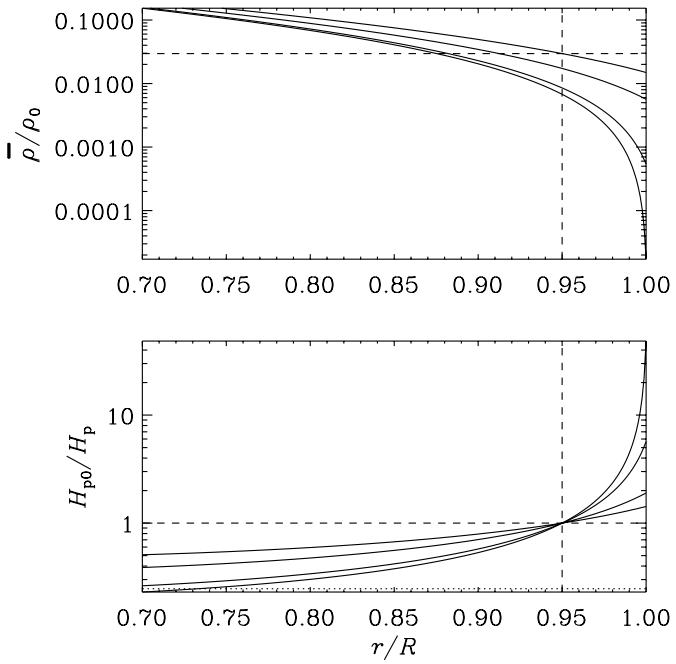

Fig. 1. Initial stratification of density and inverse scale height for $r_\star/R = 1.001$ (strongest stratification), 1.01, 1.05, and 1.1. The dashed lines mark the position of the reference radius $r_{\rm ref} = 0.95\,R$, where $\rho/\rho_0 \approx 0.0068$ for $r_\star/R = 1.001$ and $H_{\rm p}(r) = H_{\rm p0}$ by definition. The dotted line marks the value of $\eta_{\rm t}/\beta_\star u_{\rm rms} H_{\rm p0}$.

In Fig. 1 we compare therefore $H_{\rm p0}/H_{\rm p}$ with $\eta_{\rm t}/\beta_\star u_{\rm rms} H_{\rm p0}$ and see that the former exceeds the latter in our reference model with $r_\star/R = 1.001$. This suggests that NEMPI should be excited in the outer layers.

As nondimensional measures of $\eta_{\rm t}$ and $u_{\rm rms}$, we define

$$\tilde{\eta}_{\rm t} = \eta_{\rm t}/\sqrt{GMR}, \quad \tilde{u}_{\rm rms} = u_{\rm rms}/\sqrt{GM/R}, \tag{13}$$

for which we take the values $\tilde{\eta}_{\rm t} = 2\times10^{-4}$ and $\tilde{u}_{\rm rms} = 0.07$, respectively. Using the estimate $\eta_{\rm t} = u_{\rm rms}/3k_{\rm f}$ (Sur et al. 2008), our choice of $\eta_{\rm t}$ implies that the normalized wavenumber of the energy-carrying eddies is $k_{\rm f}R = \tilde{u}_{\rm rms}/3\tilde{\eta}_{\rm t} \approx 120$ and that $k_{\rm f}H_{\rm p0}$ varies between 6.2 (for $r_\star/R = 1.1$) and 2.3 (for $r_\star/R = 1.001$).

For the magnetic field, we adopt perfect conductor boundary conditions on the inner and outer radii, $r_0 = 0.7\,R$ and R, respectively, i.e.,

$$\frac{\partial \overline{A}_r}{\partial r} = \overline{A}_\theta = \overline{A}_\phi = 0, \quad \text{on } r = r_0, R. \tag{14}$$

On the pole and the equator, we assume

$$\frac{\partial \overline{A}_r}{\partial \theta} = \overline{A}_\theta = \frac{\partial \overline{A}_\phi}{\partial \theta} = 0, \quad \text{on } \theta = 0^\circ \text{ and } 90^\circ. \tag{15}$$

Since our simulations are axisymmetric, the magnetic field is conveniently represented via $\overline{B}_\phi$ and $\overline{A}_\phi$. In particular, contours of $r\sin\theta\overline{A}_\phi$ give the magnetic field lines of the poloidal magnetic field, $\overline{\boldsymbol{B}}_{\rm pol} = \boldsymbol{\nabla}\times(\overline{A}_\phi\hat{\boldsymbol{\phi}})$.

In all cases presented in this paper, we adopt a numerical resolution of 256×1024 mesh points in the r and θ directions. This is significantly higher than what has been used previously, even in mean field calculations with stratification and hydrodynamical feedback included; see Brandenburg et al. (1992), where a resolution of just 41×81 meshpoints was used routinely. In

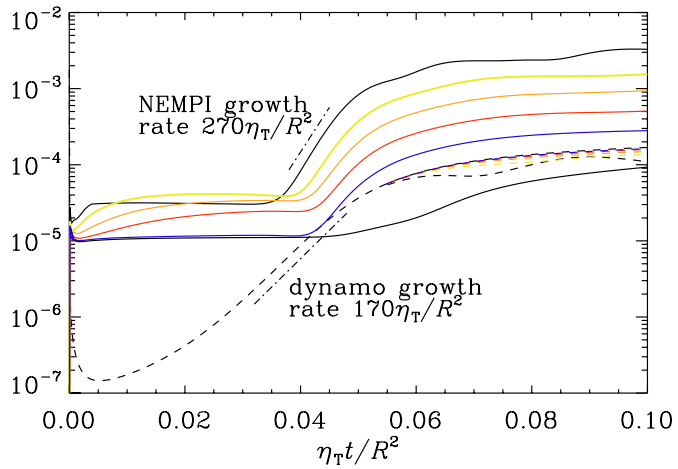

Fig. 2. Dependence of $\overline{B}_{\rm rms}$ (dashed lines) and $\overline{U}_{\rm rms}$ (solid lines) on time in units of η_T/R^2 for $q_{p0} = 0$ (black); 5 (blue); 10 (red); 20 (orange); 40 (yellow); and 100 (upper black line for $\overline{B}_{\rm rms}$). The results for $\overline{U}_{\rm rms}$ depend only slightly on q_{p0}, and this only when the dynamo is saturated.

principle, lower resolutions are possible, but in some cases we found certain properties of the solutions to be sensitive to the resolution.

3. Results

In our model, the dynamo growth rate is about $170\,\eta_T/R^2$. Although both dynamo and NEMPI are linear instabilities, this is no longer the case in our coupled system, because NEMPI depends on the magnetic field strength, and only in the nonlinear regime of the dynamo does the field reach values high enough for NEMPI to overcome turbulent magnetic diffusion. This is shown in Fig. 2 where we plot the growth of the magnetic field and compare with runs with different values of q_{p0}. For $q_{p0} = 100$ we find a growth rate of about $270\,\eta_T/R^2$. This value is significantly more than the dynamo growth rate, and the growth occurs at the time when structures form, so we associate this higher growth rate with that of NEMPI.

We now discuss the resulting magnetic field structure. We begin by discussing the effects of varying the stratification. To see the effect of NEMPI more clearly, we consider a somewhat optimistic set of parameters describing NEMPI, namely $q_{p0} = 100$ and $\beta_p = 0.05$, which yields $\beta_\star = 0.5$; see Eq. (5). This is higher than the values 0.23 and 0.33 found from numerical simulations with and without small-scale dynamo action, respectively (Brandenburg et al. 2012). The effect of lowering the value of q_{p0} can be seen in Fig. 2 and is also discussed below. We choose $Q_\alpha = 1000$ for the α quenching parameter so that the local value of $\overline{B}_\phi/B_{\rm eq}$ near the surface is between 10 and 20 percent, which is suitable for exciting NEMPI (Kemel et al. 2012b). Meridional cross-sections of $\overline{B}_\phi/B_{\rm eq0}$ together with magnetic field lines of $\overline{\boldsymbol{B}}_{\rm pol}$ are shown in Fig. 3. Note that a magnetic flux concentration develops near the surface at latitudes between 70° and 76° for weak and strong stratification, respectively. Structure formation from NEMPI occurs in the top 5% by radius, and the flux concentration is most pronounced when $r_\star \le 1.01$.

Next, if we increase the magnetic field strength by making Q_α smaller, we see that the magnetic flux concentrations move toward lower latitudes down to about 49° for $Q_\alpha = 100$; see Fig. 4. However, while this is potentially interesting for the

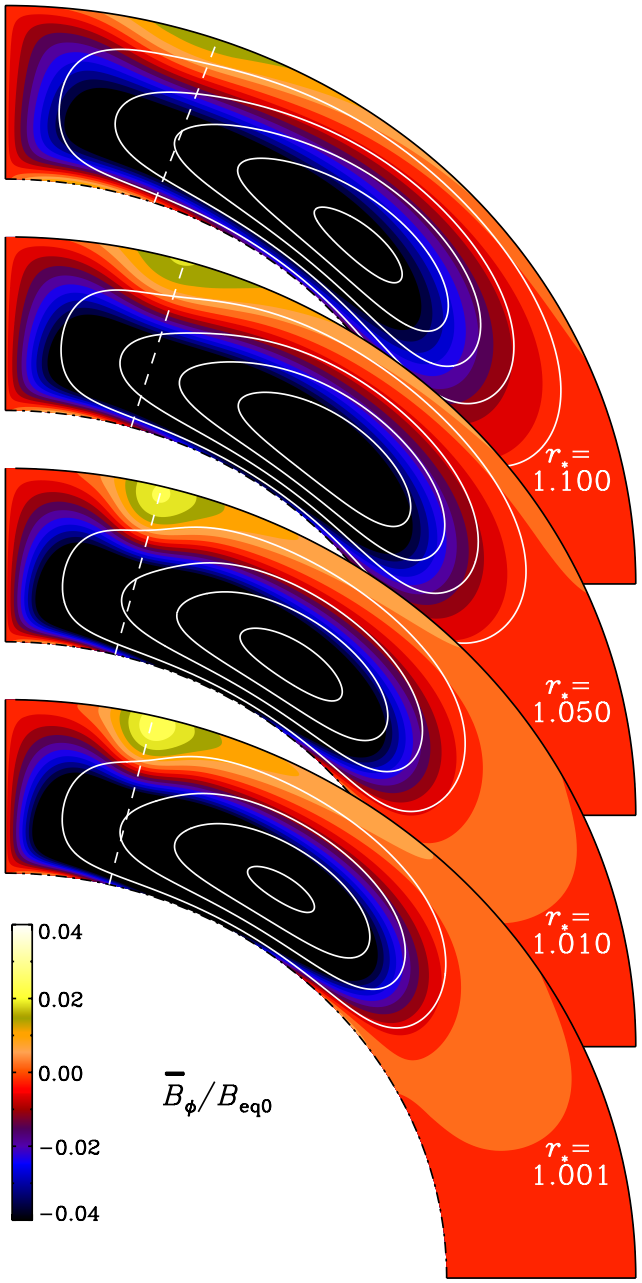

Fig. 3. Meridional cross-sections of $\overline{B}_\phi/B_{\rm eq}$ (color coded) together with magnetic field lines of $\overline{\boldsymbol{B}}_{\rm pol}$ for different stratification parameters $r_\star$ and $Q_\alpha = 10^3$. The dashed lines indicate the latitudes 70.3°, 73.4°, 75.6°, and 76.4°.

Sun, where sunspots are known to occur primarily at low latitudes, the magnetic flux concentrations also become weaker at the same time, making this feature less interesting from an astrophysical point of view. For comparison with the parameter $\beta_p = 0.05$ in Eq. (5) we note that $\beta_\alpha = Q_\alpha^{-1/2}$ takes the values 0.1, 0.07, 0.04, and 0.03 for $Q_\alpha = 100$, 200, 500, and 1000, respectively. Thus, for these models the quenchings of the nondiffusive turbulence effects in the momentum and induction equations are similar.

Also, if we decrease q_{p0} to more realistic values, we expect the magnetic flux concentrations to become weaker. This is indeed borne out by the simulations; see Fig. 5, where we show meridional cross-sections for q_{p0} in the range $40 \le q_{p0} \le 100$ for $Q_\alpha = 10^3$. This corresponds to the range $0.32 \le \beta_\star \le 0.5$.

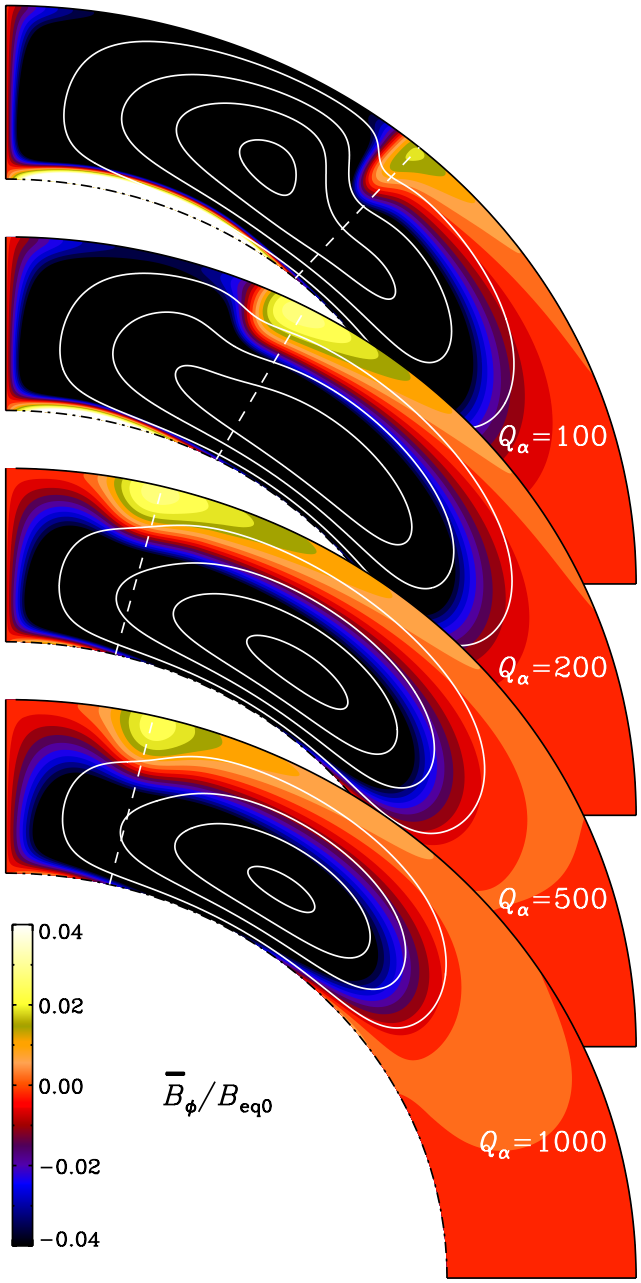

Fig. 4. Meridional cross-sections for different values of Q_α, for $r_\star = 1.001$. The dashed lines indicate the latitudes 49°, 61.5°, 75.6°, and 76.4°.

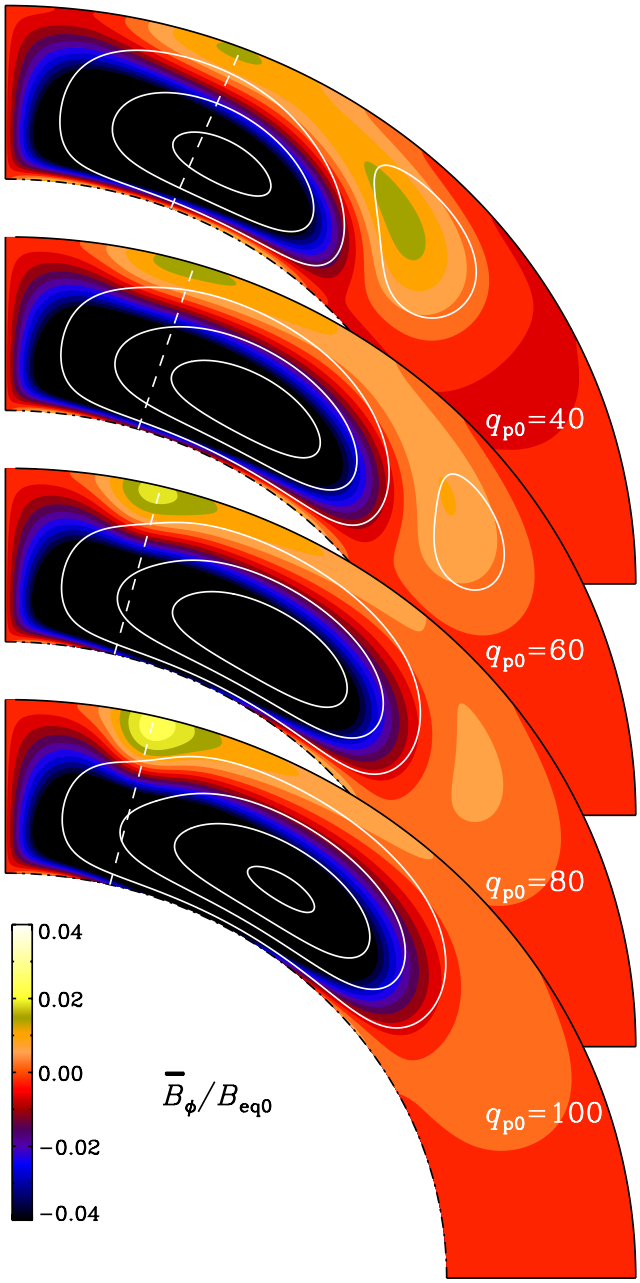

Fig. 5. Meridional cross-sections for different values of the parameter $q_{\rm p0}$ in the range $40 \le q_{\rm p0} \le 100$ for $Q_\alpha = 10^3$. The dashed lines indicate the latitudes 68°, 72.5°, 75.7°, and 76.3°.

For weaker magnetic fields, i.e., for higher values of the quenching parameter Q_α, we find that NEMPI has a modifying effect on the dynamo in that it can now become oscillatory. A butterfly diagram of $\overline{B}_r$ and $\overline{B}_\phi$ is shown in Fig. 6. Meridional cross-sections of the magnetic field at different times covering half a magnetic cycle are shown in Fig. 7. It turns out that, at sufficiently weak magnetic field strengths, NEMPI produces oscillatory solutions with poleward-migrating flux belts. The reason for this is not understood very well, but it is reminiscent of the poleward migration observed in the presence of weak rotation (Losada et al. 2012). Had this migration been equatorward, it might have been tempting to associate it with the equatorward migration of the sunspot belts in the Sun.

Finally, we discuss the change of kinetic, magnetic, and current helicities due to NEMPI. We do this by using a model that is close to our reference model with $r_\star/R = 1.001$ and $Q_\alpha = 1000$, except that $q_{\rm p0} = 0$ in the beginning, and then at time t_0 we change it to $q_{\rm p0} = 100$. The two inverse length scales based on magnetic and current helicities,

$$k_{\rm M} = \left(\frac{\int_V \overline{\boldsymbol{A}} \cdot \overline{\boldsymbol{B}} \, {\rm d}V}{\int_V \overline{\boldsymbol{B}}^2 \, {\rm d}V} \right)^{-1} \quad \text{and} \quad k_{\rm C} = \mu_0 \frac{\int_V \overline{\boldsymbol{J}} \cdot \overline{\boldsymbol{B}} \, {\rm d}V}{\int_V \overline{\boldsymbol{B}}^2 \, {\rm d}V}, \tag{16}$$

increase by 25%, while the inverse length scale based on the kinetic helicity,

$$k_{\rm K} = \frac{\int_V \overline{\boldsymbol{W}} \cdot \overline{\boldsymbol{U}} \, {\rm d}V}{\int_V \overline{\boldsymbol{U}}^2 \, {\rm d}V}, \tag{17}$$

drops to very low values after introducing NEMPI, see e.g. Fig. 8. Here, $\overline{\boldsymbol{W}} = \boldsymbol{\nabla} \times \overline{\boldsymbol{U}}$ is the mean vorticity. This behavior

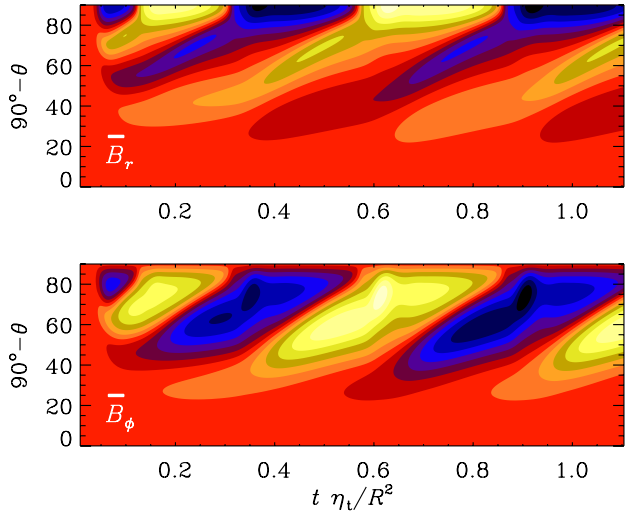

Fig. 6. Butterfly diagram of $\overline{B}_r$ (upper panel) and $\overline{B}_\phi$ (lower panel) for $Q_\alpha = 10^4$, $r_\star = 1.001$, $\omega = 11.3\,\eta_t/R^2$.

of k_K is surprising, but it seems to be associated with an increase in kinetic energy. The reason for the increase in the two inverse magnetic length scales, on the other hand, might be understandable as the consequence of increasing gradients associated with the resulting flux concentrations.

4. Conclusions

The present investigations have shown that NEMPI can occur in conjunction with the dynamo; that is, both instabilities can work at the same time and can even modify each other. It was already clear from earlier work that NEMPI can only work in a limited range of magnetic field strengths. We therefore adopted a simple α quenching prescription to arrange the field strength to be in the desired range. Furthermore, unlike much of the earlier work on NEMPI, we used an adiabatic stratification here instead of an isothermal one; see Brandenburg et al. (2010) and Käpylä et al. (2012) for earlier examples with adiabatic stratification in Cartesian geometry. An adiabatic stratification implies that the pressure scale height is no longer constant and now much shorter in the upper layers than in the bulk of the domain. This favors the appearance of NEMPI in the upper layers, because the growth rate is inversely proportional to the pressure scale height.

There are two lines of future extensions of the present model. On the one hand, it is important to study the interplay between NEMPI and the dynamo instability in more detail. This is best done in the framework of a local Cartesian model, which is more easily amenable to analytic treatment. Another important extension would be to include differential rotation. At the level of a dynamically self-consistent model, where the flow speed is a solution of the momentum equation, differential rotation is best implemented by including the Λ effect (Rüdiger 1980, 1989). This is a parameterization of the Reynolds stress that is in some ways analogous to the parameterization of the electromotive force via the α effect.

Mean-field models with both α and Λ effects have been considered before (Brandenburg et al. 1992; Rempel 2006), so the main difference would be the additional parameterization of magnetic effects in the Reynolds stress that gives rise to NEMPI. In both cases, our models would be amenable to verification using DNS by driving turbulence through a helical forcing function. In the case of a spherical shell, this can easily be done in

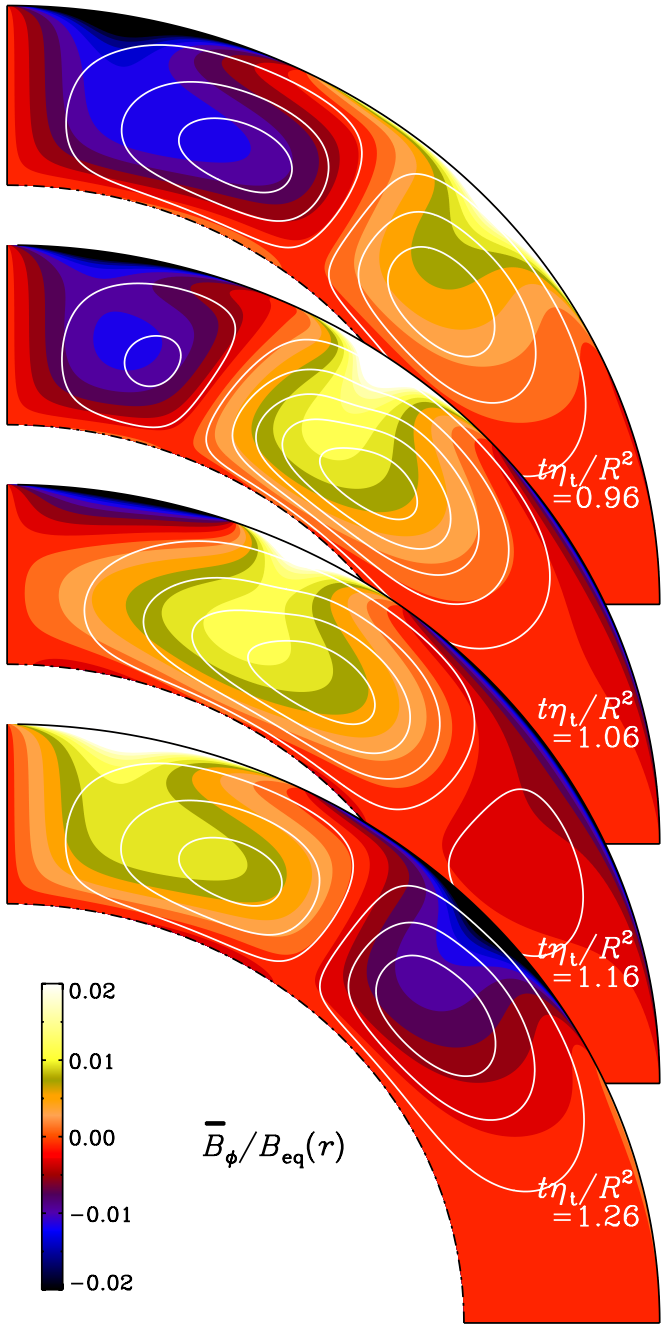

Fig. 7. Meridional cross-sections of $\overline{\boldsymbol{B}}/B_{\rm eq0}$ at different times, for $Q_\alpha = 10^4$, $r_\star = 1.001$. The cycle frequency here is $\omega = 11.3\eta_t/R^2$. Furthermore, the toroidal field is normalized by the local equipartition value, i.e., the colors indicate $\overline{B}_\phi/B_{\rm eq}(r)$.

wedge geometry where the polar regions are excluded. In that case the mean-field dynamo solutions are oscillatory with equatorward migration (Mitra et al. 2010). At an earlier phase of the present investigations we studied NEMPI in the corresponding mean-field models and found that NEMPI can reverse the propagation of the dynamo wave from equatorward to poleward. However, owing to time dependence, the effects of NEMPI are then harder to study, which is why we have refrained from studying such models in further detail.

In the case of a Cartesian domain, helically forced DNS with an open upper layer have been considered by Warnecke & Brandenburg (2010). In this model, plasmoid ejections can

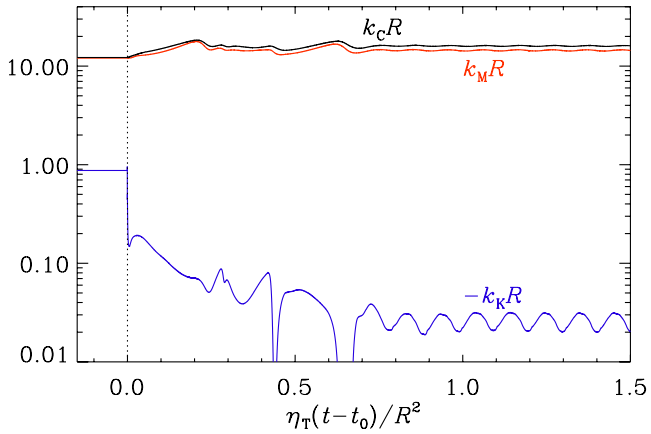

Fig. 8. The three inverse length scales k_C, k_M, and k_K as a function of time. At time t_0, the value of q_{p0} has been changed from 0 to 100.

occur and provide a more natural boundary. A more physical alternative is to use only nonhelical forcing, but to include rotation to produce helicity in conjunction with the stratification. Such models have recently been considered by Losada et al. (2013), who found that NEMPI begins to be suppressed by rotation at Coriolis numbers somewhat below those where α^2-type dynamo action sets in. Furthermore, there is now evidence that the combined action of NEMPI and the dynamo instability has a lower threshold than the dynamo alone. Those models provide an ideal setup for future studies of the interaction between both instabilities.

Acknowledgements. This work was supported in part by the European Research Council under the AstroDyn Research Project No. 227952, by the National Science Foundation under Grant No. NSF PHY05-51164 (AB), by EU COST Action MP0806, by the European Research Council under the Atmospheric Research Project No. 227915, and by a grant from the Government of the Russian Federation under contract No. 11.G34.31.0048 (NK, IR). We acknowledge the allocation of computing resources provided by the Swedish National Allocations Committee at the Center for Parallel Computers at the Royal Institute of Technology in Stockholm and the Nordic Supercomputer Center in Reykjavik.

References

Arlt, R., Sule, A., & Rüdiger, G. 2005, A&A 441, 1171
Brandenburg, A., & Subramanian, K. 2005, Phys. Rep., 417, 1
Brandenburg, A., Moss, D., & Tuominen, I. 1992, A&A, 265, 328
Brandenburg, A., Kleeorin, N., & Rogachevskii, I. 2010, Astron. Nachr., 331, 5
Brandenburg, A., Kemel, K., Kleeorin, N., Mitra, D., & Rogachevskii, I. 2011, ApJ, 740, L50
Brandenburg, A., Kemel, K., Kleeorin, N., & Rogachevskii, I. 2012, ApJ, 749, 179
Brandenburg, A., Gressel O., Käpylä, P. J., et al. 2013, ApJ, 762, 127
Cally, P. S., Dikpati, M., & Gilman, P. A. 2003, ApJ, 582, 1190
Chatterjee, P., Nandy, D., & Choudhuri, A. R. 2004, A&A, 427, 1019
Dikpati, M., & Charbonneau, P. 1999, ApJ, 518, 508
D'Silva, S., & Choudhuri, A. R. 1993, A&A, 272, 621
Guerrero, G., & Käpylä, P. J. 2011, A&A, 533, A40
Käpylä, P. J., Brandenburg, A., Kleeorin, N., Mantere, M. J., & Rogachevskii, I. 2012, MNRAS, 422, 2465
Kemel, K., Brandenburg, A., Kleeorin, N., Mitra, D., & Rogachevskii, I. 2012a, Sol. Phys., 280, 321
Kemel, K., Brandenburg, A., Kleeorin, N., Mitra, D., & Rogachevskii, I. 2012b, Sol. Phys., DOI:10.1007/s11207-012-0031-8
Kemel, K., Brandenburg, A., Kleeorin, N., & Rogachevskii, I. 2012c, Astron. Nachr., 333, 95
Kleeorin, N., & Rogachevskii, I. 1994, Phys. Rev. E, 50, 2716
Kleeorin, N. I., Rogachevskii, I. V., & Ruzmaikin, A. A. 1989, Sov. Astron. Lett., 15, 274
Kleeorin, N. I., Rogachevskii, I. V., & Ruzmaikin, A. A. 1990, Sov. Phys. JETP, 70, 878
Kleeorin, N., Mond, M., & Rogachevskii, I. 1996, A&A, 307, 293
Krause, F., & Rädler, K.-H. 1980, Mean-field magnetohydrodynamics and dynamo theory (Oxford: Pergamon Press)
Losada, I. R., Brandenburg, A., Kleeorin, N., Mitra, D., & Rogachevskii, I. 2012, A&A, 548, A49
Losada, I. R., Brandenburg, A., Kleeorin, N., & Rogachevskii, I. 2013, A&A, 556, A83
Mitra, D., Tavakol, R., Brandenburg, A., & Moss, D. 2009, ApJ, 697, 923
Mitra, D., Tavakol, R., Käpylä, P. J., & Brandenburg, A. 2010, ApJ, 719, L1
Moffatt, H. K. 1978, Magnetic field generation in electrically conducting fluids (Cambridge: Cambridge University Press)
Newcomb, W. A. 1961, Phys. Fluids, 4, 391
Ossendrijver, M. 2003, A&ARv, 11, 287
Parker, E. N. 1955, ApJ, 121, 491
Parker, E.N. 1966, ApJ, 145, 811
Parker, E. N. 1979, Cosmical magnetic fields (New York: Oxford University Press)
Parker, E. N. 1982, ApJ, 256, 302
Parker, E. N. 1984, ApJ, 283, 343
Priest, E. R. 1982, Solar Magnetohydrodynamics (Dordrecht: D. Reidel Publ. Co.)
Rempel, M. 2006, ApJ, 647, 662
Roberts, P. H. 1972, Phil. Trans. R. Soc., A272, 663
Rogachevskii, I., & Kleeorin, N. 2007, Phys. Rev. E, 76, 056307
Rüdiger, G. 1980, Geophys. Astrophys. Fluid Dyn., 16, 239
Rüdiger, G. 1989, Differential rotation and stellar convection: Sun and solar-type stars (New York: Gordon & Breach)
Schüssler, M., Caligari P., Ferriz-Mas A., & Moreno-Insertis F. 1994, A&A, 281, L69
Spiegel, E. A., & Weiss, N. O. 1980, Nature, 287, 616
Spruit, H. C. 1981, A&A, 98, 155
Sur, S., Brandenburg, A., & Subramanian, K. 2008, MNRAS, 385, L15
Steenbeck, M., Krause, F., & Rädler, K.-H. 1966, Z. Naturforsch., 21, 369
Stenflo, J. O., & Kosovichev, A. G. 2012, ApJ, 745, 129
Stix, M. 1989, The Sun: An Introduction (Berlin and Heidelberg: Springer)
Warnecke, J., & Brandenburg, A. 2010, A&A, 523, A19
Zeldovich, Ya. B., Ruzmaikin, A. A., & Sokoloff, D. D. 1983, Magnetic fields in astrophysics (New York: Gordon & Breach)

II

Astronomy & Astrophysics manuscript no. paper
April 23, 2014

Magnetic flux concentrations from dynamo-generated fields

S. Jabbari[1,2], A. Brandenburg[1,2], I. R. Losada[1,2], N. Kleeorin[3,1,4], and I. Rogachevskii[3,1,4]

[1] Nordita, KTH Royal Institute of Technology and Stockholm University, Roslagstullsbacken 23, 10691 Stockholm, Sweden
[2] Department of Astronomy, AlbaNova University Center, Stockholm University, 10691 Stockholm, Sweden
[3] Department of Mechanical Engineering, Ben-Gurion University of the Negev, POB 653, Beer-Sheva 84105, Israel
[4] Department of Radio Physics, N. I. Lobachevsky State University of Nizhny Novgorod, Russia

April 23, 2014, Revision: 1.129

ABSTRACT

Context. The mean-field theory of magnetized stellar convection gives rise to the two possibility of distinct instabilities: the large-scale dynamo instability, operating in the bulk of the convection zone and a negative effective magnetic pressure instability (NEMPI) operating in the strongly stratified surface layers. The latter might be important in connection with magnetic spot formation. However, the growth rate of NEMPI is suppressed with increasing rotation rates. On the other hand, recent direct numerical simulations (DNS) have shown a subsequent increase in the growth rate.
Aims. We examine quantitatively whether this increase in the growth rate of NEMPI can be explained by an α^2 mean-field dynamo, and whether both NEMPI and the dynamo instability can operate at the same time.
Methods. We use both DNS and mean-field simulations (MFS) to solve the underlying equations numerically either with or without an imposed horizontal field. We use the test-field method to compute relevant dynamo coefficients.
Results. DNS show that magnetic flux concentrations are still possible up to rotation rates above which the large-scale dynamo effect produces mean magnetic fields. The resulting DNS growth rates are quantitatively well reproduced with MFS. As expected, for weak or vanishing rotation, the growth rate of NEMPI increases with increasing gravity, but there is a correction term for strong gravity and large turbulent magnetic diffusivity.
Conclusions. Magnetic flux concentrations are still possible for rotation rates above which dynamo action takes over. For the solar rotation rate, the corresponding turbulent turnover time is about 5 hours, with dynamo action commencing in the layers beneath.

Key words. Sun: sunspots – Sun: dynamo – turbulence – magnetohydrodynamics (MHD) – hydrodynamics

1. Introduction

The appearance of surface magnetic field in the Sun presents some peculiar characteristics, such as being strongly concentrated into discrete spots. The origin and depth of such magnetic flux concentrations has long been subject to considerable speculation. A leading theory by Parker (1955) interprets the emergence of such spots as the result of magnetically buoyant flux tubes at a depth of some 20 Mm. This magnetic field must be the result of a dynamo, but magnetic buoyancy also leads to the buoyant rise and subsequent loss of those magnetic structures. It was therefore thought that the dynamo should operate mainly at or even below the bottom of the convection zone where magnetic buoyancy could be stabilized by a subadiabatic temperature gradient (Parker, 1975). This led eventually to the idea that sunspots might be a direct consequence of dynamo-generated flux tubes that rise all the way from the bottom of the convection zone to the surface (e.g. Caligari et al., 1995). However, Schüssler (1980, 1983) emphasized already early on that such fields would easily be "brain-washed" and would lose their systematic east–west orientation while ascending through the turbulent convection zone. D'Silva & Choudhuri (1993) estimated that a magnetic field strength of about $100\,\mathrm{kG}$ would be needed to preserve not only the overall east–west orientation (Hale et al., 1919), but also to produce the observed tilt angle of active regions known as Joy's law.

A great deal of effort has gone into determining the conditions under which magnetic flux ropes may or may not be able to rise buoyantly across the convection zone. Emonet et al. (1998) determined for the first time the basic minimum twist thresholds for the survival of twisted magnetic flux ropes during the rise. Subsequent studies were based on different types of numerical simulations, which tested the underlying hypotheses and looked for other effects, such as the robustness against background convective motions (Jouve et al., 2013) and magnetic flux erosion by reconnection with the background dynamo field (Pinto et al., 2013). These studies, as well as many others (see, e.g., Fan, 2008, 2009, and references therein) specifically looked at what flux-rope configurations are able to reproduce the observed emergent polarity tilt angles (Joy's law).

The observed variation in the number of sunspots in time and latitude is expected to be linked to some kind of large-scale dynamo, as it has been modeled by Leighton et al. (1969) and Steenbeck & Krause (1969) long ago. This led Schüssler (1980) to propose a so-called flux-tube dynamo approach that would couple the buoyant rise of thin flux tubes to their regeneration. However, even today the connection between dynamos and flux tubes is done "by hand" (see, e.g., Choudhuri et al., 2007; Miesch & Dikpati, 2014), which means that some ad hoc procedure is invoked to link flux tube emergence to a mean-field dynamo. Of course, such tubes, or at least bipolar regions, should eventually emerge from a sufficiently well-resolved and realistic simulation of solar convection. While global convective dynamo simulations of Nelson et al. (2011, 2013, 2014) show magnetically buoyant magnetic flux tubes of $\approx 40\,\mathrm{kG}$ field strength, they do not yet address bipolar region formation. Indeed, solar surface simulations of Cheung et al. (2010) and Rempel &

Cheung (2014) demonstrate that bipolar spots do form once a magnetic flux tube of 10 kG field strength is injected at the bottom of their domain. On the other hand, the deep solar simulations of Stein & Nordlund (2012) develop a bipolar active region with just 1 kG magnetic field injected at the bottom of their domain. While these simulations taken together outline what might occur in the Sun, they do not necessarily support the description of spots as a direct result of thin flux tubes piercing the surface (e.g. Caligari et al., 1995).

A completely different suggestion is that sunspots develop locally at the solar surface, and that their east–west orientation would reflect the local orientation of the mean magnetic field close to the surface. The tilt angle would then be determined by latitudinal shear producing the observed orientation of the meridional component of the magnetic field (Brandenburg, 2005a). One of the possible mechanisms of local spot formation is the negative effective magnetic pressure instability (NEMPI; see Kleeorin et al., 1989, 1990; Kleeorin & Rogachevskii, 1994; Kleeorin et al., 1996; Rogachevskii & Kleeorin, 2007). Another potential mechanism of flux concentration is related to a turbulent thermo-magnetic instability in turbulence with radiative boundaries caused by the suppression of turbulent heat flux through the large-scale magnetic field (Kitchatinov & Mazur, 2000). The latter instability has so far only been found in mean-field simulations (MFS), but not in direct numerical simulations (DNS) nor in large-eddy simulations (LES). By contrast, NEMPI has recently been found in DNS (Brandenburg et al., 2011) and LES (Brandenburg et al., 2014) of strongly stratified fully developed turbulence.

NEMPI can lead to the formation of equipartition-strength magnetic spots (Brandenburg et al., 2013, 2014), which are reminiscent of sunspots. Even bipolar spots can form in the presence of a horizontal magnetic field near the surface; see (Warnecke et al., 2013). For this idea to be viable, NEMPI and the dynamo instability would need to operate in reasonable proximity of each other, so that the dynamo can supply the magnetic field that would be concentrated into spots, as was recently demonstrated by Mitra et al. (2014). In studying this process in detail, we have a chance of detecting new joint effects resulting from the two instabilities, which is one of the goals of the present paper. However, these two instabilities may also compete against each other, as was already noted by Losada et al. (2013). The large-scale dynamo effect relies on the combined presence of rotation and stratification, while NEMPI requires stratification and large enough scale separation. NEMPI is being suppressed by even a moderate amount of rotation. This was shown by Losada et al. (2012), who found significant suppression of NEMPI when the Coriolis number $\mathrm{Co}=2\Omega\tau$ is larger than about 0.03. Here, Ω is the angular velocity and τ the turnover time of the turbulence, which is related to the rms velocity $u_{\rm rms}$ and the wavenumber $k_{\rm f}$ of the energy-carrying eddies via $\tau=(u_{\rm rms}k_{\rm f})^{-1}$. For the solar convection zone, the Coriolis number,

$$\mathrm{Co}=2\Omega/u_{\rm rms}k_{\rm f}, \tag{1}$$

varies from 2×10^{-3} (at the surface using $\tau=5\,\mathrm{min}$) to 5 (at the bottom of the convection zone using $\tau=10\,\mathrm{days}$). The value $\mathrm{Co}=0.03$ corresponds to a turnover time as short as two hours, which is the case at a depth of $\approx10\,\mathrm{Mm}$.

The strength of stratification, on the other hand, is quantified by the nondimensional parameter

$$\mathrm{Gr}=g/c_{\rm s}^2k_{\rm f}\equiv(k_{\rm f}H_\rho)^{-1}, \tag{2}$$

where $H_\rho=c_{\rm s}^2/g$ is the density scale height, $c_{\rm s}$ is the sound speed, and g is the gravitational acceleration. In the cases considered by Losada et al. (2012, 2013), the stratification parameter was $\mathrm{Gr}=0.03$, which is rather small compared with the estimated solar value of $\mathrm{Gr}=0.16$; see the conclusions of Losada et al. (2013). One may expect that larger values of Gr would result in correspondingly larger values of the maximum permissible value of Co, for which NEMPI is still excited, but this has not yet been investigated in detail.

The goal of the present paper is to study rotating stratified hydromagnetic turbulence in a parameter regime that we expect to be at the verge between NEMPI and dynamo instabilities. We do this by performing DNS and MFS. In MFS, the study of combined NEMPI and dynamo instability requires suitable parameterizations of the negative effective magnetic pressure and α effects using suitable turbulent transport coefficients.

2. DNS study

We begin by reproducing first some of the DNS results of Losada et al. (2013), who found the suppression of the growth rate of NEMPI with increasing values of Co and a subsequent enhancement at larger values, which they interpreted as being the result of dynamo action in the presence of an externally applied magnetic field. We also use DNS to determine independently the expected efficiency of the dynamo by estimating the α effect from kinetic helicity measurements and by computing both α effect and turbulent diffusivity directly using the test-field method (TFM).

2.1. Basic equations

In DNS of an isothermally stratified layer (Losada et al., 2013) we solve the equations for the velocity $\boldsymbol{U}$, the magnetic vector potential $\boldsymbol{A}$, and the density ρ in the presence of rotation Ω,

$$\frac{\mathrm{D}\boldsymbol{U}}{\mathrm{D}t} = \frac{1}{\rho}\boldsymbol{J}\times\boldsymbol{B}-2\boldsymbol{\Omega}\times\boldsymbol{U}-\nu\boldsymbol{Q}+\boldsymbol{F}+\boldsymbol{f}, \tag{3}$$

$$\frac{\partial\boldsymbol{A}}{\partial t} = \boldsymbol{U}\times\boldsymbol{B}-\eta\boldsymbol{J}, \tag{4}$$

$$\frac{\partial\rho}{\partial t} = -\boldsymbol{\nabla}\cdot\rho\boldsymbol{U}, \tag{5}$$

where $\mathrm{D}/\mathrm{D}t=\partial/\partial t+\boldsymbol{U}\cdot\boldsymbol{\nabla}$ is the advective derivative, $\boldsymbol{\Omega}=\Omega\hat{\boldsymbol{z}}$ is the angular velocity,

$$\boldsymbol{F}=\boldsymbol{g}-c_{\rm s}^2\boldsymbol{\nabla}\ln\rho \tag{6}$$

determines the hydrostatic force balance, ν is the kinematic viscosity, η is the magnetic diffusivity due to Spitzer conductivity of the plasma,

$$-\boldsymbol{Q} = \nabla^2\boldsymbol{U}+\boldsymbol{\nabla}\boldsymbol{\nabla}\cdot\boldsymbol{U}/3+2\mathsf{S}\boldsymbol{\nabla}\ln\rho, \tag{7}$$

$$-\boldsymbol{J} = \nabla^2\boldsymbol{A}-\boldsymbol{\nabla}\boldsymbol{\nabla}\cdot\boldsymbol{A}, \tag{8}$$

are the modified vorticity and the current density, respectively, where the vacuum permeability μ_0 has been set to unity,

$$\boldsymbol{B}=\boldsymbol{B}_0+\boldsymbol{\nabla}\times\boldsymbol{A} \tag{9}$$

is the total magnetic field, $\boldsymbol{B}_0=(0,B_0,0)$ is the imposed uniform field, and

$$\mathsf{S}_{ij}=\tfrac{1}{2}(\partial_jU_i+\partial_iU_j)-\tfrac{1}{3}\delta_{ij}\boldsymbol{\nabla}\cdot\boldsymbol{U} \tag{10}$$

is the traceless rate-of-strain tensor. The forcing function $\boldsymbol{f}$ consists of random, white-in-time, plane, nonpolarized waves with a certain average wavenumber $k_{\rm f}$. The turbulent rms velocity is

approximately independent of z with $u_{\rm rms}=\langle \boldsymbol{u}^2\rangle^{1/2}\approx 0.1\,c_{\rm s}$. The gravitational acceleration $\boldsymbol{g}=(0,0,-g)$ is chosen such that $k_1H_\rho=1$, so the density contrast between bottom and top is $\exp(2\pi)\approx 535$ in a domain $-\pi\leq k_1z\leq\pi$. Here, $H_\rho=c_{\rm s}^2/g$ is the density scale height and $k_1=2\pi/L$ is the smallest wavenumber that fits into the cubic domain of size L^3. We adopt Cartesian coordinates (x,y,z), with periodic boundary conditions in the x- and y-directions and stress-free, perfectly conducting boundaries at top and bottom ($z=\pm L_z/2$). In most of the calculations, we use a scale separation ratio $k_{\rm f}/k_1$ of 30, so Gr $=0.03$ is still the same as in earlier calculations. We use a fluid Reynolds number Re $\equiv u_{\rm rms}/\nu k_{\rm f}$ of 36, and a magnetic Prandtl number ${\rm Pr}_M=\nu/\eta$ of 0.5. The magnetic Reynolds number is therefore ${\rm Re}_M={\rm Pr}_M{\rm Re}=18$. These values are a compromise between having both $k_{\rm f}$ and Re large enough for NEMPI to develop at an affordable numerical resolution. The value of B_0 is specified in units of $B_{\rm eq0}=\sqrt{\rho_0}\,u_{\rm rms}$, where $\rho_0=\langle\rho\rangle$ is the volume-averaged density, which is constant in time. The local equipartition field strength is $B_{\rm eq}(z)=\sqrt{\rho}\,u_{\rm rms}$. In our units, $k_1=c_{\rm s}=\mu_0=\rho_0=1$. However, time is specified as the turbulent-diffusive time $t\,\eta_{\rm t0}k_1^2$, where $\eta_{\rm t0}=u_{\rm rms}/3k_{\rm f}$ is the estimated turbulent diffusivity. We also use DNS to compute these values more accurately with the TFM. The simulations are performed with the PENCIL CODE (http://pencil-code.googlecode.com), which uses sixth-order explicit finite differences in space and a third-order accurate time-stepping method. We use a numerical resolution of 256^3 mesh points, which was found to be sufficient for the parameter regime specified above.

2.2. At the verge between NEMPI and dynamo

The work of Losada et al. (2013) suggested that for Gr $=0.03$ and Co ≥ 0.03, NEMPI becomes strongly suppressed, and that for still larger values, the growth rate increases again. This was tentatively associated with dynamo action, but it was not investigated in further detail. We now consider such a case with Co $=0.09$. This is a value that resulted in a rather low growth rate, while the estimated growth rate would be still subcritical for dynamo action. Following the work of Losada et al. (2013), we impose here a horizontal magnetic field in the y direction with a strength of $0.05B_{\rm eq0}$, which was previously found to be in the optimal range for NEMPI to develop (Kemel et al., 2012a).

To bring out the structures more clearly, it was found to be advantageous to present mean magnetic fields by averaging over the y direction and over a certain time interval Δt. We denote such averages by an overbar, e.g., $\overline{B}_y$. Once a dynamo develops, we expect a Beltrami-type magnetic field with a $\overline{B}_x$ component that is phase shifted relative to $\overline{B}_y$ by $\pi/2$. These are force-free fields with $\boldsymbol{\nabla}\times\overline{\boldsymbol{B}}=k\overline{\boldsymbol{B}}$ such as $\overline{\boldsymbol{B}}\propto(\sin kz,\cos kz,0)$, for example.

Figure 1 shows visualizations of $\overline{B}_x$ and $\overline{B}_y$ together with the effective magnetic pressure, $\mathcal{P}_{\rm eff}$ (defined below), at different times for a value of Co that is around the point where we expect onset of dynamo action. As in earlier work without rotation (Kemel et al., 2013), $\overline{B}_y$ varies between 0 to $2B_0$. Furthermore, $\overline{B}_x$ is found to vary in the range $\pm2B_0$. In Fig. 2, the x extent of the domain is twice as big: $-2\pi<k_1x<2\pi$. In Fig. 3 we show the result for Co $=0.22$, where a Beltrami-type field with a $\pi/2$ phase shift between $\overline{B}_x$ and $\overline{B}_y$ is well developed. For smaller values of Co, there are structures (e.g., for $t/\tau=1.8$ at $x/H_\rho\approx1.5$ and for $t/\tau=2.4$ at $x/H_\rho\approx1.5$ and -2) that are reminiscent of those associated with NEMPI; compare Fig. 1 with Fig. 4 of Kemel et al. (2013) or Fig. 3 of Losada et al. (2013). When the domain is twice as wide, the number of structures simply doubles. A similar phenomenon was also seen in the simulations of Kemel et al. (2012b). For larger values of Co, NEMPI is suppressed and the α^2 dynamo, which generates the mean magnetic field of Beltrami-type structure, becomes more strongly excited.

The effective magnetic pressure shown in Figs. 1–3 is estimated by computing the xx-component of the total stress from the fluctuating velocity and magnetic fields as

$$\Delta\overline{\Pi}^{\rm f}_{xx}=\overline{\rho}\,(\overline{u_x^2}-\overline{u_{0x}^2})+\tfrac{1}{2}(\overline{\boldsymbol{b}^2}-\overline{\boldsymbol{b}_0^2})-(\overline{b_x^2}-\overline{b_{0x}^2}),\tag{11}$$

where the subscript 0 refers to the case with $B_0=0$. We then calculate (Brandenburg et al., 2012a)

$$q_{\rm p}=-2\Delta\overline{\Pi}^{\rm f}_{xx}/\overline{\boldsymbol{B}}^2.\tag{12}$$

Here, $q_{\rm p}(\beta)$ is a function of $\beta=\overline{B}/B_{\rm eq}(z)$. We then calculate $\mathcal{P}_{\rm eff}=\frac{1}{2}(1-q_{\rm p})\beta^2$, which is the effective magnetic pressure divided by $B_{\rm eq}^2$. Note that $\mathcal{P}_{\rm eff}$ shows a systematic z dependence and is negative in the upper part. Variations in the x direction are comparatively weak and do therefore not show a clear correspondence with the horizontal variations of $\overline{B}_y$.

As in earlier work (Brandenburg et al., 2011), we characterize the strength of resulting structures by an amplitude B_k of a suitable low wavenumber Fourier mode ($k/k_1=1$ or 2), which is based on the magnetic field in the upper part of the domain, $2\leq z/H_\rho\leq\pi$. In Fig. 4 we compare the evolution of $B_k/B_{\rm eq0}$ for runs with different values of Co. For comparison, we also reproduce the first few runs for Co $=0.006$–0.13, where we used $k/k_1=1$ in all cases. It turns out that for the new cases with Co $=0.09$ and 0.22, the growth of $B_k/B_{\rm eq0}$ is not as strong as for the cases with smaller Co. Furthermore, as is also evident from Figs. 1 and 2, the structures are now characterized by $k/k_1=2$, while for Co $=0.22$ they are still characterized by $k/k_1=1$. The growth for all three cases (Co $=0.09$, both for normal and wider domains, as well as Co $=0.22$) is similar. However, given that the typical NEMPI structures are not well seen for Co $=0.22$, it is possible that the growth of structures is simply overwhelmed by the much stronger growth due to the dynamo, which is not reflected in the growth of $B_k/B_{\rm eq0}$, whose growth is still mainly indicative of NEMPI. In this sense, there is some evidence for the occurrence of NEMPI in both cases.

2.3. Kinetic helicity

We begin by considering a fixed value of Gr equal to that used by Losada et al. (2013) and vary Co. For small values of Co, their data agreed with the MFS of Losada et al. (2012). For faster rotation, one crosses eventually the dynamo threshold. This is also the point at which the growth rate begins to increase again, although it now belongs to a different instability than for small values of Co. The underlying mechanism is the α^2-dynamo, which is characterized by the dynamo number

$$C_\alpha=\alpha/\eta_{\rm T}k_1,\tag{13}$$

where α is the typical value of the α effect (here assumed spatially constant), $\eta_{\rm T}=\eta_{\rm t}+\eta$ is the sum of turbulent and microphysical magnetic diffusivities, and k_1 is the lowest wavenumber of the magnetic field that can be fitted into the domain. For isotropic turbulence, α and $\eta_{\rm t}$ are respectively proportional to the negative kinetic helicity and the mean squared velocity (Moffatt,

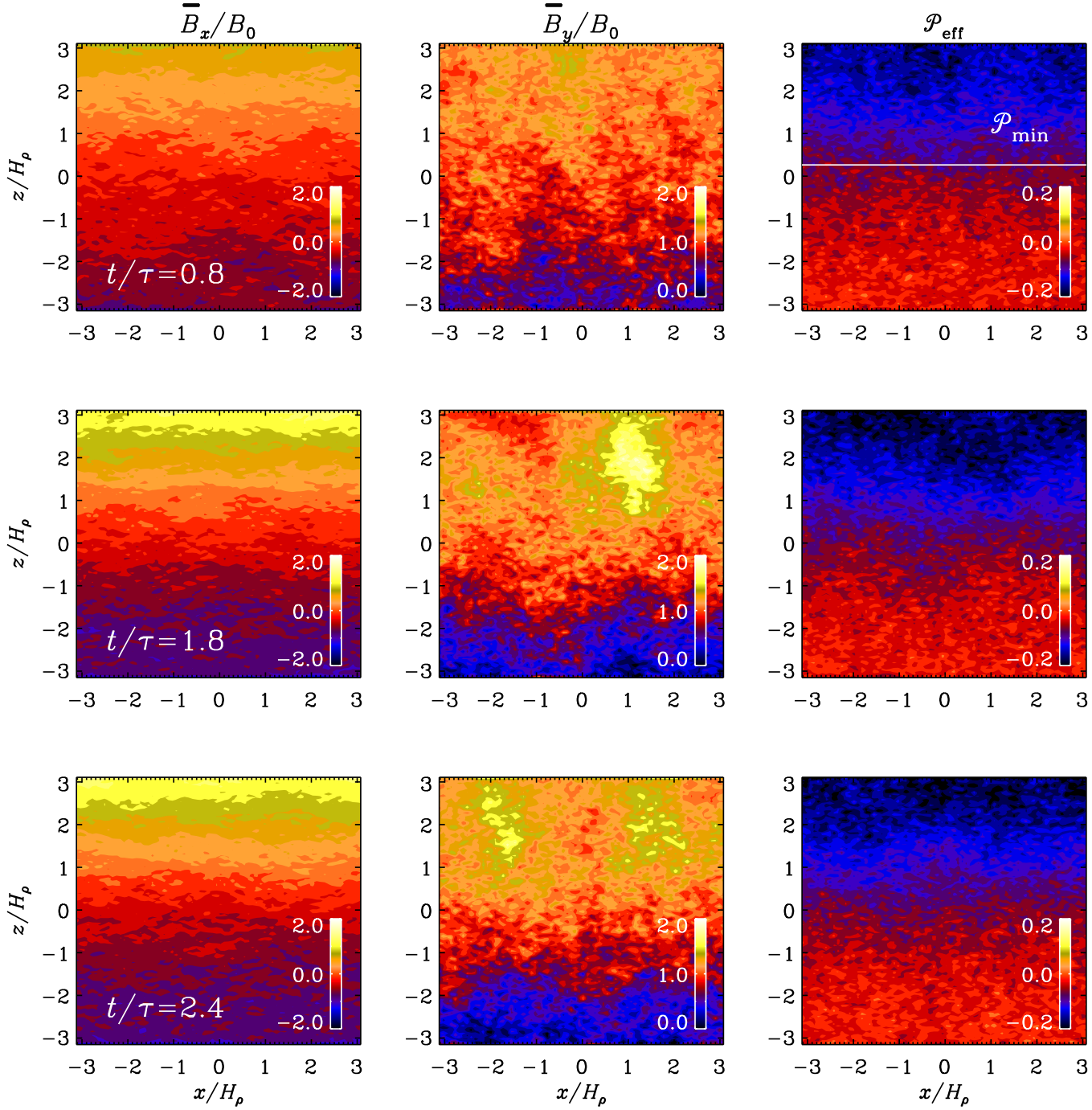

Fig. 1. Visualization of $\overline{B}_x/B_{\rm eq0}$ and $\overline{B}_y/B_0$ together with effective magnetic pressure for different times. Here $\Omega = 0.15$, Co $= 0.09$, Gr $= 0.033$, and $k_{\rm f}/k_1 = 30$.

1978; Krause & Rädler, 1980; Rädler et al., 2003; Kleeorin & Rogachevskii, 2003)

$$\alpha \approx \alpha_0 \equiv -\tfrac{1}{3}\tau\overline{\boldsymbol{\omega}\cdot\boldsymbol{u}}, \quad \eta_{\rm t} \approx \eta_{\rm t0} \equiv \tfrac{1}{3}\tau\overline{\boldsymbol{u}^2}, \tag{14}$$

where $\tau = (u_{\rm rms}k_{\rm f})^{-1}$, so that (Blackman & Brandenburg, 2002; Candelaresi & Brandenburg, 2013)

$$C_\alpha = -\epsilon_k\epsilon_{\rm f}k_{\rm f}/k_1. \tag{15}$$

Here, ϵ_k is a free parameter characterizing possible dependencies on the forcing wavenumber, and $\epsilon_{\rm f}$ is a measure for the relative kinetic helicity. Simulations of Brandenburg et al. (2012b) and Losada et al. (2013) showed that

$$\epsilon_{\rm f} \equiv \overline{\boldsymbol{\omega}\cdot\boldsymbol{u}}/k_{\rm f}u_{\rm rms}^2 \approx \epsilon_{\rm f0}\,{\rm Gr\,Co} \quad ({\rm Gr\,Co} \lesssim 0.1), \tag{16}$$

where $\epsilon_{\rm f0}$ is yet another non-dimensional parameter of the order of unity that may depend weakly on the scale separation ratio, $k_{\rm f}/k_1$, and is slightly different with and without imposed field. In the absence of an imposed field, Brandenburg et al. (2012b) found $\epsilon_{\rm f0} \approx 2$ using $k_{\rm f}/k_1 = 5$. However, both an imposed field and a larger value of $k_{\rm f}/k_1$ lead to a slightly increased value of $\epsilon_{\rm f0}$. Our results are summarized in Fig. 5 for cases with

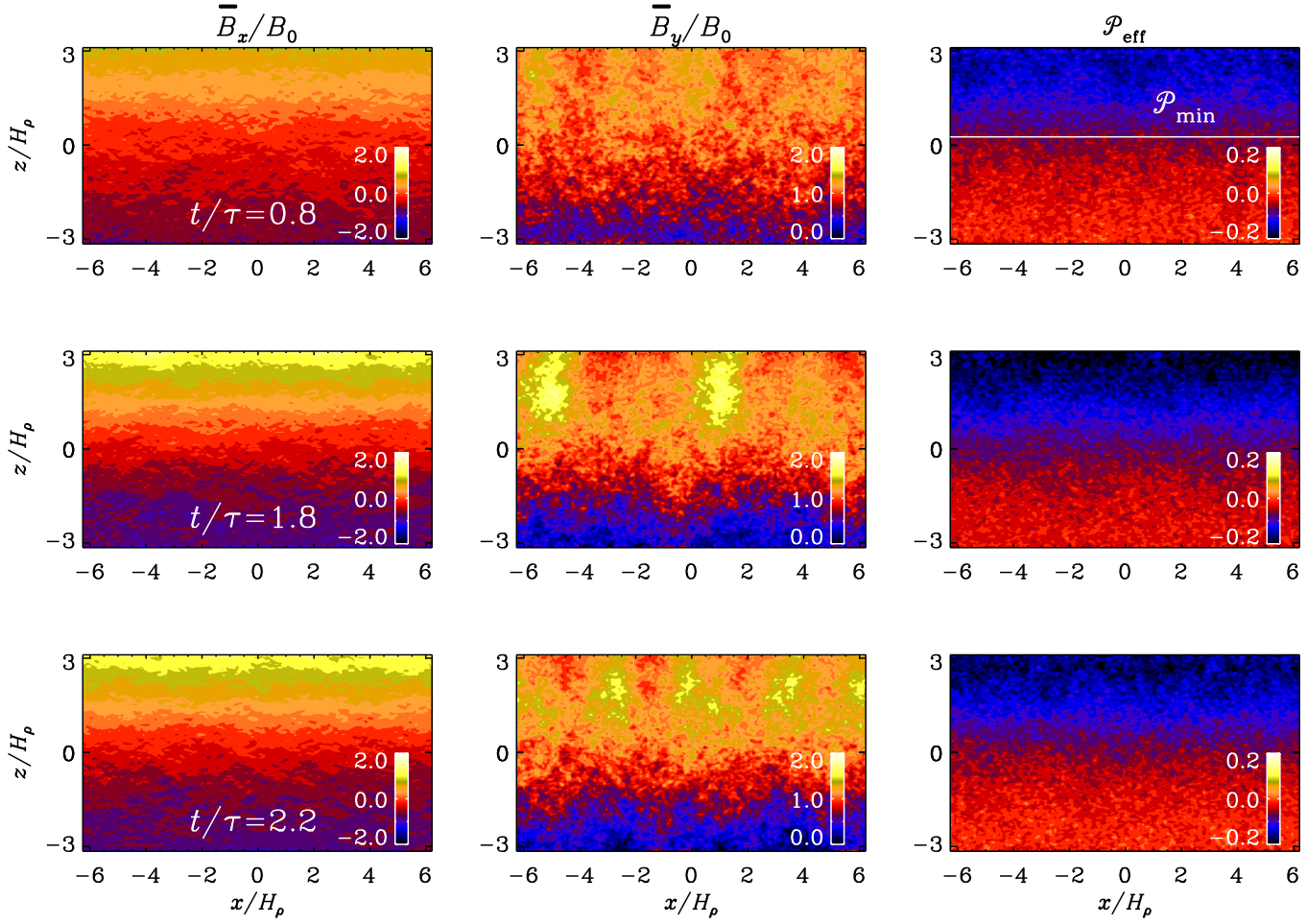

Fig. 2. Like Fig. 1, but for a wider domain.

and without imposed magnetic field. Error bars are estimated as the largest departure of any one third of the full time series. The relevant points of Losada et al. (2013) give $\epsilon_{\rm f0} \approx 2.8$. For Gr Co $\gtrsim 0.5$, the results of Brandenburg et al. (2012b) show a maximum with a subsequent decline of $\epsilon_{\rm f}$ with increasing values of Co. However, although it is possible that the position of this maximum may be different for other values of Gr, it is unlikely to be relevant to our present study where we focus on smaller values of C_α near dynamo onset. Thus, in conclusion, Eq. (16) seems to be a useful approximation that has now been verified over a range of different values of $k_{\rm f}/k_1$.

2.4. Test-field results

Our estimate for C_α is based on the reference values α_0 and $\eta_{\rm t0}$ that are defined in Eq. (14) and represent approximations obtained from earlier simulations of helically forced turbulence (Sur et al., 2008). In the present study, helicity is self-consistently generated from the interaction between rotation and stratification. As an independent way of computing α and $\eta_{\rm t}$, we now use the test-field method (TFM). It consists of solving auxiliary equations describing the evolution of magnetic fluctuations, $\boldsymbol{b}^{pq}$, resulting from a set of several prescribed mean or test fields, $\overline{\boldsymbol{B}}^{pq}$. We solve for the corresponding vector potential $\boldsymbol{a}^{pq}$ with $\boldsymbol{b}^{pq}=\boldsymbol{\nabla}\times\boldsymbol{a}^{pq}$,

$$\frac{\partial \boldsymbol{a}^{pq}}{\partial t} = \boldsymbol{u}\times\overline{\boldsymbol{B}}^{pq} + \overline{\boldsymbol{U}}\times\boldsymbol{b}^{pq} + (\boldsymbol{u}\times\boldsymbol{b}^{pq})' + \eta\nabla^2\boldsymbol{a}^{pq}, \quad (17)$$

where $(\boldsymbol{u}\times\boldsymbol{b}^{pq})' = \boldsymbol{u}\times\boldsymbol{b}^{pq} - \overline{\boldsymbol{u}\times\boldsymbol{b}^{pq}}$ is the fluctuating part of the electromotive force and

$$\overline{\boldsymbol{B}}^{ic} = \hat{\boldsymbol{x}}_i\cos kz, \quad \overline{\boldsymbol{B}}^{is} = \hat{\boldsymbol{x}}_i\sin kz, \quad i=1,2, \quad (18)$$

are the four test fields, which can show a cosine or sine variation with z, while $\hat{\boldsymbol{x}}_1=(1,0,0)$ and $\hat{\boldsymbol{x}}_2=(0,1,0)$ are unit vectors in the two horizontal coordinate directions. The resulting $\boldsymbol{b}^{pq}$ are used to compute the electromotive force, $\overline{\boldsymbol{\mathcal{E}}}^{pq}=\overline{\boldsymbol{u}\times\boldsymbol{b}^{pq}}$, which is then expressed in terms of $\overline{\boldsymbol{B}}^{pq}$ and $\overline{\boldsymbol{J}}^{pq}=\boldsymbol{\nabla}\times\overline{\boldsymbol{B}}^{pq}$ as

$$\overline{\mathcal{E}}_i^{pq} = \alpha_{ij}\overline{B}_j^{pq} - \eta_{ij}\overline{J}_j^{pq}. \quad (19)$$

By doing this for all four test field vectors, the x and y components of each of them gives eight equations for the eight unknowns, α_{11}, α_{12}, ..., η_{22}; see Brandenburg (2005b) for further details.

With the TFM, we obtain the kernels α_{ij} and η_{ij}, from which we compute

$$\alpha = \tfrac{1}{2}(\alpha_{11}+\alpha_{22}), \quad \eta_{\rm t} = \tfrac{1}{2}(\eta_{11}+\eta_{22}), \quad (20)$$

$$\gamma = \tfrac{1}{2}(\alpha_{21}-\alpha_{12}), \quad \delta = \tfrac{1}{2}(\eta_{21}-\eta_{12}). \quad (21)$$

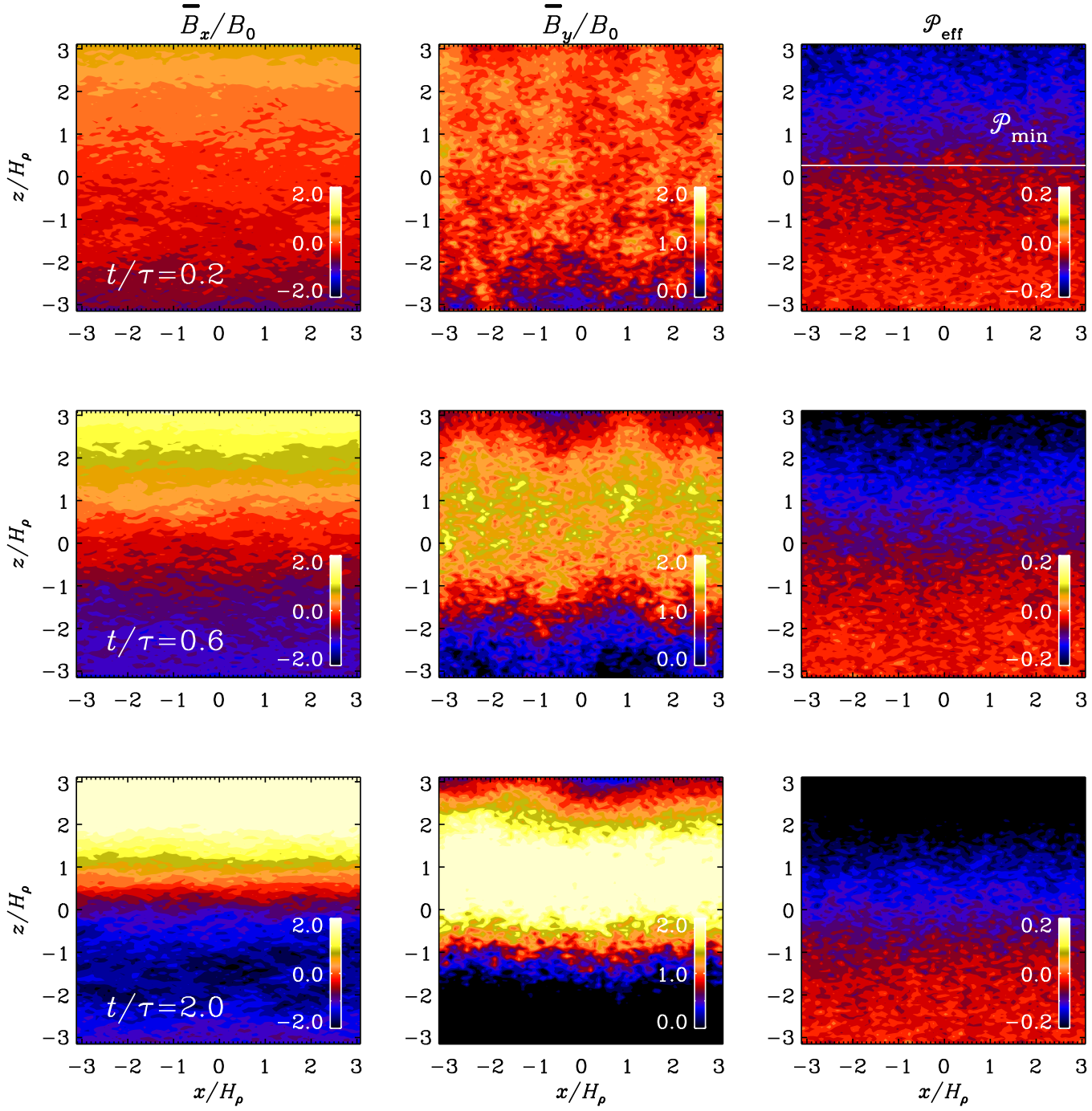

Fig. 3. Like Fig. 1, but for $\Omega = 0.35$, so Co $= 0.22$.

We normalize α and $\eta_{\rm t}$ by their respective values obtained for large magnetic Reynolds numbers defined in Eq. (14), and denote them by a tilde, i.e., $\tilde{\alpha} = \alpha/\alpha_0$ and $\tilde{\eta}_{\rm t} = \eta_{\rm t}/\eta_{\rm t0}$. We use the latter normalization also for δ, i.e., $\tilde{\delta} = \delta/\eta_{\rm t0}$, but expect its value to vanish in the limit of zero angular velocity. No standard turbulent pumping velocity is expected (Krause & Rädler, 1980; Moffatt, 1978), because the rms turbulent velocity is independent of height. However, this is not quite true. To show this, we normalize γ by $u_{\rm rms}$ and present $\tilde{\gamma} = \gamma/u_{\rm rms}$. In this normalization, the molecular value is given by $\eta/\eta_0 = 3/{\rm Re}_M$.

We consider test fields that are constant in time and vary sinusoidally in the z direction. We choose certain values of k between 1 and 60 and also vary the value of Co between 0 and about 1.06 while keeping Gr $= 0.033$ fixed. In all cases where the scale separation ratio is held fixed, we used $k_{\rm f}/k_1 \approx 30$, which is larger than what has been used in earlier studies (Brandenburg et al., 2008b), where $k_{\rm f}/k_1$ was typically 5.

In Figure 6 we show the dependence of the coefficients on the normalized wavenumber of the test field, $k/k_{\rm f}$. The three coefficients $\tilde{\alpha}$, $\tilde{\eta}_{\rm t}$, and $\tilde{\delta}$ show the same behavior of the form of:

$$\tilde{\sigma} = \tilde{\sigma}_0/\left(1+\ell_\sigma^2 k^2\right), \tag{22}$$

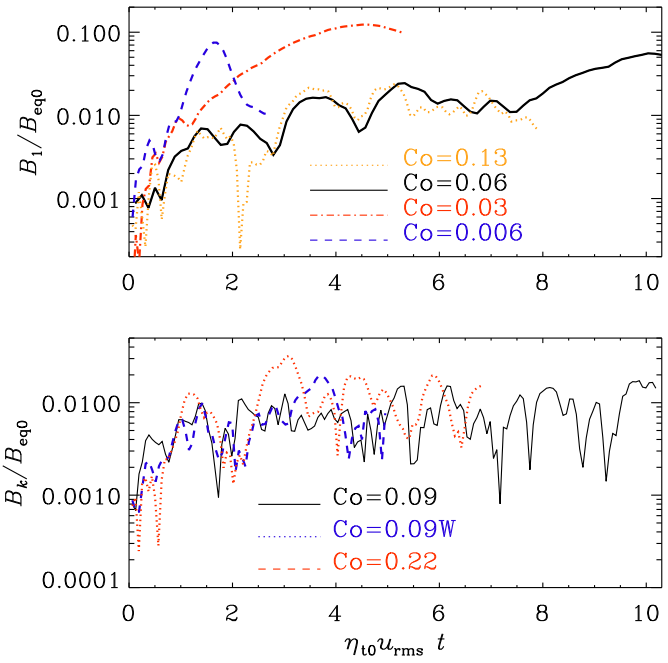

Fig. 4. Comparison of the evolution of $B_k/B_{\rm eq0}$ for runs with different values of Co. In the first panel, $k/k_1 = 1$, while in the second panel, $k/k_1 = 2$ for the two runs with Co $= 0.09$ (label W refers to the wider box in the x direction), and $k/k_1 = 1$ for the run with Co $= 0.22$.

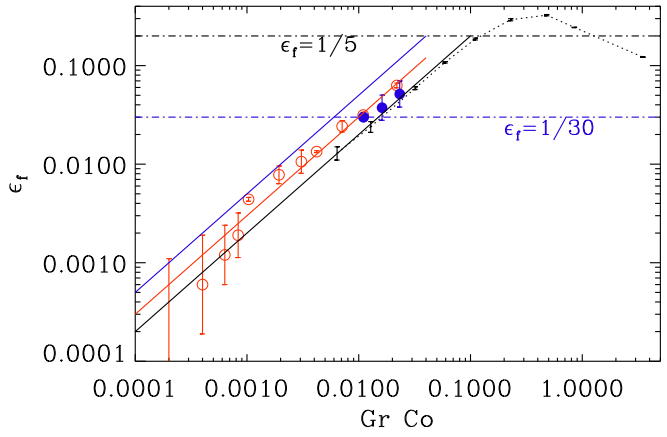

Fig. 5. Dependence of $\epsilon_{\rm f}$ on Gr Co obtained in DNS with imposed field (open symbols, red) and without (closed symbols, blue), for $k_{\rm f}/k_1 = 30$. The black symbols connected by a dotted line correspond to the values of Brandenburg et al. (2012b) for $k_{\rm f}/k_1 = 5$. The horizontal lines correspond to the dynamo threshold for the two values of $k_{\rm f}/k_1$.

for $\tilde{\sigma} = \tilde{\alpha}$, $\tilde{\eta}_{\rm t}$, or $\tilde{\delta}$, while for $\tilde{\gamma}$ we use

$$\tilde{\gamma} = \tilde{\gamma}_0 + \tilde{\gamma}_2 \ell_\gamma^2 k^2 / \left(1 + \ell_\gamma^2 k^2\right), \quad (23)$$

where $\tilde{\gamma}_0 = 0.01$, $\tilde{\gamma}_2 = 0.06$, and $\ell_\gamma = 2.5$. These results have been obtained for Co $= 0.59$ and $B_{0y}/B_{\rm eq0} = 0.05$. Again, error bars are estimated as the largest departure of any one third of the full time series.

Most of the coefficients are only weakly dependent on the value of Co, except γ and δ. The former varies approximately like

$$\tilde{\gamma} = \tilde{\gamma}_0 + \tilde{\gamma}_\Omega^2 {\rm Co}^2, \quad (24)$$

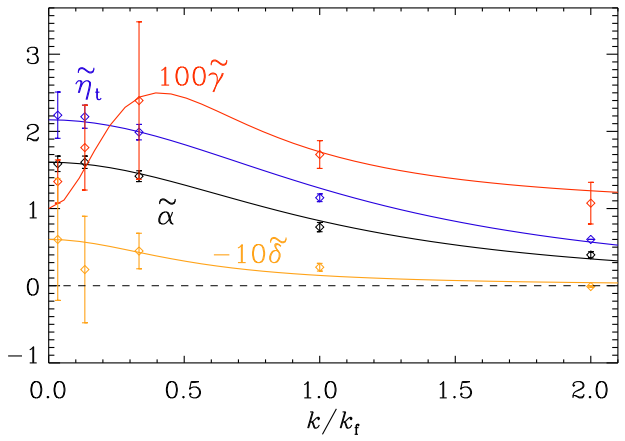

Fig. 6. TFM coefficients versus scale separation ratio, $k/k_{\rm f}$, for Co $=$ 0.59, ${\rm Re}_M = 18$, $B_{0y}/B_{\rm eq0} = 0.05$, $\tilde{g} = 1$ and $\eta k_1/c_{\rm s} = 2 \times 10^{-4}$.

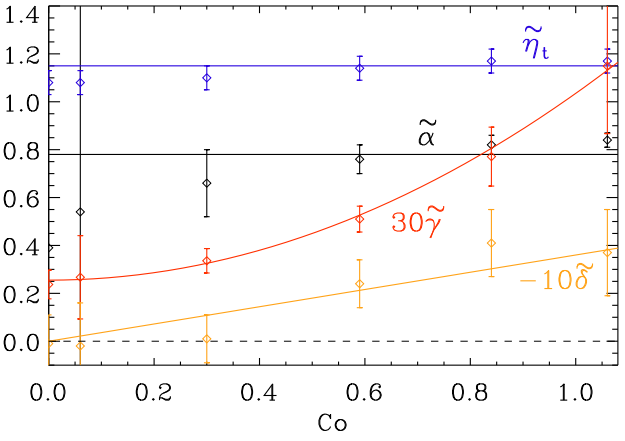

Fig. 7. TFM coefficients versus Coriolis number, Co, for $k/k_{\rm f} = 1$, ${\rm Re}_M = 18$, $B_{0y}/B_{\rm eq0} = 0.05$, $\tilde{g} = 1$, and $\eta k_1/c_{\rm s} = 2 \times 10^{-4}$.

where $\tilde{\gamma}_0 = 0.85$ and $\tilde{\gamma}_\Omega^2 = 2.6$. Here and in the following, we keep $k/k_{\rm f} = 1/30$. For the same value of $k/k_{\rm f}$, the functional form for δ shows a linear increase with Co, i.e., $\tilde{\delta} = \tilde{\delta}_0 {\rm Co}$ where $\tilde{\delta}_0 = 0.036$. Figure 7 shows that $\tilde{\alpha}$ is nearly independent of the Coriolis number. This result should be compared with Figs. 2a, 3a, and 4a of Kleeorin & Rogachevskii (2003), where a theory of the α versus the Coriolis number was developed for large fluid and magnetic Reynolds numbers. It turns out that the new values of α and $\eta_{\rm t}$ that have been obtained now with the TFM are somewhat different from previous TFM studies that originally estimated ($\tilde{\alpha} \approx 0.8$ and $\tilde{\eta}_{\rm t} \approx 1.15$). The TFM results now suggest $\epsilon_k = 0.6$ in Eq. (15). The reason for this discrepancy cannot just be the fact that helicity is now self-consistently generated, because this was also the case in the earlier work of Brandenburg et al. (2012b). The only plausible reason is the large value of $k_{\rm f}/k_1$ that is now much larger than before (30 compared to 5 in most previous studies), which explains the reason for our choice of the subscript in ϵ_k.

The origin of weak pumping found in Figs. 6 and 7 is unclear. For a weak mean magnetic field, pumping of the magnetic field can cause not only inhomogeneous distributions of the velocity fluctuations (Krause & Rädler, 1980; Moffatt, 1978) or magnetic fluctuations (Rädler et al., 2003), but also non-uniform distribu-

tion of the fluid density in the presence either of small-scale dynamo or turbulent convection (Rogachevskii & Kleeorin, 2006). In our simulations there is no small-scale dynamo effect, because Re_M is too low. There is also no turbulent convection possible in our setup. The pumping effect is also not connected with the nonlinear effects; see Fig. 2 in Rogachevskii & Kleeorin (2004).

3. MFS study

We now want to see whether the suppression of NEMPI and the subsequent increase in the resulting growth rate can be reproduced in MFS. In addition to a parameterization for the negative effective magnetic pressure in the momentum equation, we add one for the electromotive force. The important terms here are the α effect and the turbulent magnetic diffusivity, whose combined effect is captured by the quantity C_α, which is defined in Eq. (13) and related to DNS parameters in Eq. (15). In contrast to DNS, the advantage of MFS is that they can more easily be extended to astrophysically interesting conditions of large Reynolds numbers and more complex geometries.

3.1. The model

Our MFS model is in many ways the same as that of Jabbari et al. (2013), where parameterizations for negative effective magnetic pressure and electromotive force where, for the first time, considered in combination with each other. Their calculations where performed in spherical shells without Coriolis force, while here we apply instead Cartesian geometry and do include the Coriolis force. The evolution equations for mean velocity $\overline{\boldsymbol{U}}$, mean vector potential $\overline{\boldsymbol{A}}$, and mean density $\overline{\rho}$, are thus

$$\frac{\mathrm{D}\overline{\boldsymbol{U}}}{\mathrm{D}t}=\frac{1}{\overline{\rho}}\left(\overline{\boldsymbol{J}}\times\overline{\boldsymbol{B}}+\boldsymbol{\nabla}\frac{q_\mathrm{p}\overline{\boldsymbol{B}}^2}{2}\right)-2\boldsymbol{\Omega}\times\overline{\boldsymbol{U}}-\nu_\mathrm{T}\overline{\boldsymbol{Q}}+\overline{\boldsymbol{F}}, \quad (25)$$

$$\frac{\partial\overline{\boldsymbol{A}}}{\partial t}=\overline{\boldsymbol{U}}\times\overline{\boldsymbol{B}}+\alpha\overline{\boldsymbol{B}}-\eta_\mathrm{T}\overline{\boldsymbol{J}}, \quad (26)$$

$$\frac{\mathrm{D}\overline{\rho}}{\mathrm{D}t}=-\overline{\rho}\boldsymbol{\nabla}\cdot\overline{\boldsymbol{U}},$$

where $\mathrm{D}/\mathrm{D}t=\partial/\partial t+\overline{\boldsymbol{U}}\cdot\boldsymbol{\nabla}$ is the advective derivative,

$$\overline{\boldsymbol{F}}=\boldsymbol{g}-c_\mathrm{s}^2\boldsymbol{\nabla}\ln\overline{\rho} \quad (27)$$

is the mean-field hydrostatic force balance, $\eta_\mathrm{T}=\eta_\mathrm{t}+\eta$ and $\nu_\mathrm{T}=\nu_\mathrm{t}+\nu$ are the sums of turbulent and microphysical values of magnetic diffusivity and kinematic viscosities, respectively, α is the aforementioned coefficient in the α effect, $\overline{\boldsymbol{J}}=\boldsymbol{\nabla}\times\overline{\boldsymbol{B}}$ is the mean current density,

$$-\overline{\boldsymbol{Q}}=\nabla^2\overline{\boldsymbol{U}}+\tfrac{1}{3}\boldsymbol{\nabla}\boldsymbol{\nabla}\cdot\overline{\boldsymbol{U}}+2\overline{\mathsf{S}}\boldsymbol{\nabla}\ln\overline{\rho} \quad (28)$$

is a term appearing in the viscous force, where $\overline{\mathsf{S}}$ is the traceless rate of strain tensor of the mean flow with components $\overline{\mathsf{S}}_{ij}=\frac{1}{2}(\overline{U}_{i,j}+\overline{U}_{j,i})-\frac{1}{3}\delta_{ij}\boldsymbol{\nabla}\cdot\overline{\boldsymbol{U}}$, and finally $\boldsymbol{\nabla}(q_\mathrm{p}\overline{\boldsymbol{B}}^2/2)$ determines the turbulent contribution to the mean Lorentz force. Here, q_p depends on the local field strength and is approximated by (Kemel et al., 2012a)

$$q_\mathrm{p}(\beta)=\frac{q_\mathrm{p0}}{1+\beta^2/\beta_\mathrm{p}^2}=\frac{\beta_\star^2}{\beta_\mathrm{p}^2+\beta^2}, \quad (29)$$

where q_p0, β_p, and $\beta_\star=\beta_\mathrm{p}q_\mathrm{p0}^{1/2}$ are constants, $\beta=|\overline{\boldsymbol{B}}|/B_\mathrm{eq}$ is the normalized mean magnetic field, and $B_\mathrm{eq}=\sqrt{\rho}\,u_\mathrm{rms}$ is the equipartition field strength. For $\mathrm{Re}_M\lesssim 60$, Brandenburg et al. (2012a) found $\beta_\star\approx 0.33$ and $\beta_\mathrm{p}\approx 1.05/\mathrm{Re}_M$. We use as our reference model the parameters for $\mathrm{Re}_M=18$, used also by Losada et al. (2013), which yields

$$\beta_\mathrm{p}=0.058,\quad \beta_\star=0.33 \quad \text{(reference model)}. \quad (30)$$

In some cases we also compare with $\beta_\star=0.44$, which was found to match more closely the measured dependence of the effective magnetic pressure on β by Losada et al. (2013). For vertical magnetic fields, MFS for a range of model parameters have been given by Brandenburg et al. (2014). In the MFS, we use (Sur et al., 2008)

$$\eta_\mathrm{t}\approx\eta_\mathrm{t0}\equiv u_\mathrm{rms}/3k_\mathrm{f}, \quad (31)$$

to replace $k_\mathrm{f}=u_\mathrm{rms}/3\eta_\mathrm{t}$, so

$$\mathrm{Gr}=3\eta_\mathrm{t}/u_\mathrm{rms}H_\rho \quad (32)$$

and (Losada et al., 2013)

$$\mathrm{Co}=2\Omega/u_\mathrm{rms}k_\mathrm{f}=6\Omega\eta_\mathrm{t}/u_\mathrm{rms}^2. \quad (33)$$

We now consider separately cases where we vary either Co or Gr. In addition, we also vary the scale separation ratio k_f/k_1, which is essentially a measure of the inverse turbulent diffusivity, i.e.,

$$k_\mathrm{f}/k_1=u_\mathrm{rms}/3\eta_\mathrm{t}k_1; \quad (34)$$

see Eq. (31).

3.2. Fixed value of Gr

The work of Losada et al. (2012) has shown that the growth rate of NEMPI, λ, decreases with increasing values of the rotation rate. They found it to be advantageous to express λ in terms of the quantity

$$\lambda_{*0}=\beta_\star u_\mathrm{rms}/H_\rho. \quad (35)$$

As discussed above, the normalized growth rate λ/λ_{*0} shows first a decline with increasing values of Co, but then, for $\mathrm{Co}>0.13$ or so, an increase, that was argued to be a result of the dynamo effect (Losada et al., 2013). This curve has a minimum at $\mathrm{Co}\approx 0.13$. As rotation is increased further, the combined action of stratification and rotation leads to increased kinetic helicity and thus eventually to the onset of mean-field α^2 dynamo action.

Owing to the effects of turbulent diffusion, the actual value of the growth rate of NEMPI is always expected to be less than λ_{*0}. Kemel et al. (2013) proposed an empirical formula replacing λ by $\lambda+\eta_\mathrm{t}k^2$, where k is the relevant wavenumber. This would lead to

$$\lambda/\lambda_{*0}\propto 1-\mathrm{Gr}_*/\mathrm{Gr}, \quad (36)$$

with a coefficient $\mathrm{Gr}_*=\tilde{\eta}_\mathrm{t}/3\beta_\star\mathrm{Ma}$. However, as we will see below, this expression is not found to be consistent with our numerical data.

The onset of the dynamo instability is governed by the dynamo number

$$C_\alpha=\epsilon_\mathrm{f0}\,\mathrm{Gr}\,\mathrm{Co}\,k_\mathrm{f}/k_1. \quad (37)$$

For a cubic domain, large-scale dynamo action occurs for $C_\alpha>1$, which was confirmed by Losada et al. (2013), who found the typical Beltrami fields for two supercritical cases. They used

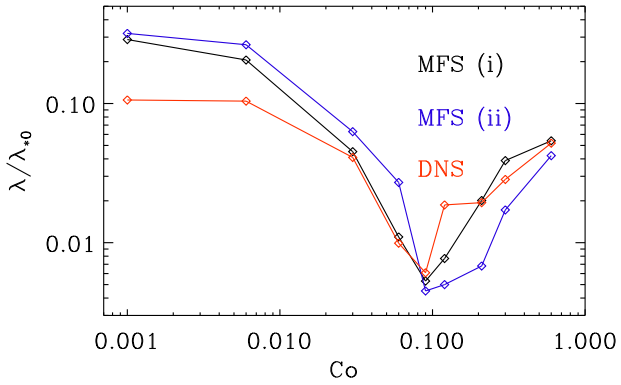

Fig. 8. Non-dimensional growth rate of NEMPI versus Co for MFS(i) with $\beta_\star = 0.33$ and MFS(ii) with $\beta_\star = 0.44$, as well as DNS for $\mathrm{Gr} = 0.033$ and $\beta_0 = 0.05$.

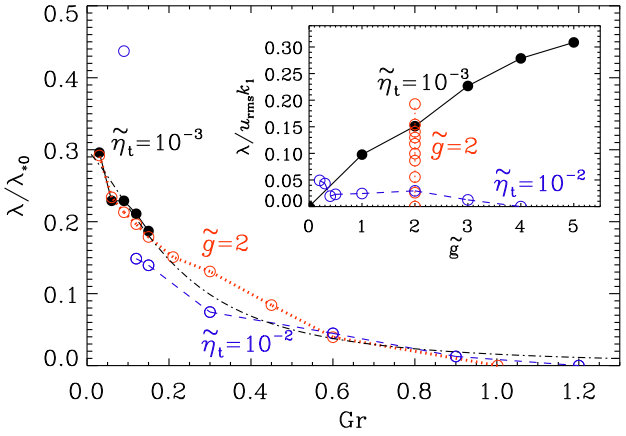

Fig. 9. Normalized growth rate of NEMPI versus stratification parameter Gr that varies with changing gravity, g, for $\mathrm{Co} = 0$, constant $\tilde{\eta}_\mathrm{t}$ ($\tilde{\eta}_\mathrm{t} = 10^{-3}$ black, filled symbols and $\tilde{\eta}_\mathrm{t} = 10^{-2}$ blue, open symbols), or it changes with different $\eta_\mathrm{t} = \nu_\mathrm{t}$ for constant $\tilde{g} = 2$ (red, open symbols). The dash-dotted line shows the approximate fit given by Eq. (40). The inset shows the growth rate normalized by the turnover time as a function of $\tilde{g}$.

the parameters $\mathrm{Gr} = 0.033$ and values of Co up to 0.6. Here we present MFS in two- and three-dimensional domains for the same values of Gr and a similar range of Co values. In Fig. 8, we compare the DNS of Losada et al. (2013) with our reference model defined through Eq. (30) and referred to as MFS(i) as well as with the case $\beta_\star = 0.44$, referred to as MFS(ii).

3.3. Larger stratification, smaller scale separation

The theoretically expected maximum growth rate of NEMPI is given by Eq. (35). At zero rotation, we thus expect $\lambda/\lambda_{*0} \approx 1$. To check this, we have performed two-dimensional MFS in a squared domain of size $(2\pi)^2$. The result is shown in Fig. 9 for the model parameters given in Eq. (30). When Gr is small, we find that $\lambda/\lambda_{*0} \approx 0.3$, which is below the expected value. As we increase Gr, λ/λ_{*0} decreases until NEMPI can no longer be detected for $\mathrm{Gr} \gtrsim 1.2$.

It is conceivable that this decrease may have been caused by the following two facts. Firstly, the growth rate is expected to increase with Gr, but for fixed scale separation, the resulting density contrast becomes huge. Finite resolution might therefore have caused inaccuracies. Secondly, although the growth rate should not depend on B_0 (Kemel et al., 2012a), we need to make sure that the mode is fully contained within the domain. In other words, we are interested in the largest growth rate as we vary the value of B_0. Again, to limit computational expense, we have tried only a small number of runs, keeping the size of the domain the same. This may have caused additional uncertainties. However, it turns out that our results are independent of whether Gr is changed by changing g or η_t ($= \nu_\mathrm{t}$). This suggests that our results for large values of g shown in Fig. 9 may in fact be accurate. To illustrate this more clearly, we rewrite

$$\mathrm{Gr} = \frac{3\eta_\mathrm{t}}{u_\mathrm{rms} H_\rho} = \frac{3\tilde{\eta}_\mathrm{t}}{k_1}\,\frac{c_\mathrm{s}}{u_\mathrm{rms}}\,\frac{g}{c_\mathrm{s}^2} = 3\tilde{\eta}_\mathrm{t}\tilde{g}/\mathrm{Ma}, \tag{38}$$

where we have defined

$$\tilde{\eta}_\mathrm{t} = \eta_\mathrm{t} k_1/c_\mathrm{s}, \quad \tilde{g} = g/c_\mathrm{s}^2 k_1 \equiv (k_1 H_\rho)^{-1}. \tag{39}$$

Fig. 9 shows that λ/λ_{*0} is indeed independent of the individual values of $\tilde{\eta}_\mathrm{t}$ and $\tilde{g}$ as long as Gr is the same. For small values of $\tilde{g}$ and large diffusivity ($\tilde{\eta}_\mathrm{t} = 10^{-2}$), the velocity evolves in an oscillatory fashion with a rapid growth and a gradual subsequent decline. In Fig. 9, the isolated data point at $\lambda/\lambda_{*0} \approx 0.44$ reflects the speed of growth during the periodic rise phase, but it is unclear whether or not it is related to NEMPI.

In the inset, we plot $\lambda/u_\mathrm{rms} k_\mathrm{f}$ versus $\tilde{g}$ itself. This shows that the growth rate (in units of the inverse turnover time) increases with increasing $\tilde{g}$ when $\tilde{\eta}_\mathrm{t}$ is small. However, the growth rate decreases with increasing $\tilde{\eta}_\mathrm{t}$. When $\tilde{\eta}_\mathrm{t}$ is larger (corresponding to smaller scale separation), the growth rate of NEMPI is reduced for the same value of $\tilde{g}$ and it decreases with $\tilde{g}$ when $\tilde{g} \gtrsim 2$.

The decrease of λ/λ_{*0} with increasing values of Gr can be approximated by the formula

$$\lambda/\lambda_{*0} \approx 0.3\,/\left[1 + 2\mathrm{Gr} + (4\mathrm{Gr})^2\right], \tag{40}$$

which is shown in Fig. 9 as a dash-dotted lined. This expression is qualitatively different from the earlier, more heuristic expression proposed by Kemel et al. (2013) where the dimensional growth rate was simply modified by an ad hoc diffusion term of the form $\eta_\mathrm{t} k^2$. In that case, contrary to our MFS, the normalized growth rate would actually increase with increasing values of Gr; see Eq. (36).

3.4. Co dependence at larger stratification

We consider the normalized growth rate of the combined NEMPI and dynamo instabilities as a function of Co for different values of Gr. As it is clear from Fig. 9, using a fixed value of g and varying η_t gives us the possibility to increase Gr to larger values of up to 1. In the following we used this procedure to compare the behavior of the growth rate versus Co for three values of Gr, 0.12, 0.21, and 1; see Fig. 10. It can be seen that the behavior of the curves is independent of the values of Gr, but the points where the minima of the curves occur moves toward bigger values of Co as Gr increases. This also happens in the case when there is only dynamo action without imposed magnetic field (dashed lines in Fig. 10). One also sees that the increase of the growth rate with increasing Co is much stronger in the case of larger Gr (compare the lines for $\mathrm{Gr} = 0.12$ with those for 0.21 and 1). Finally, comparing runs with and without imposed magnetic

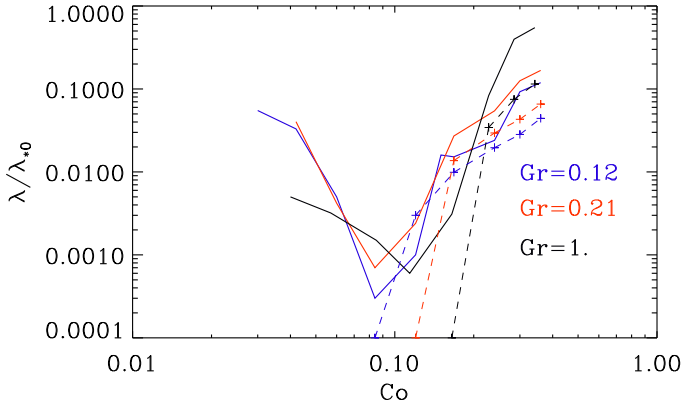

Fig. 10. Normalized growth rate of the combined NEMPI and dynamo instability (solid lines) together with cases with pure dynamo instability (no imposed field, dashed lines) versus Co for three different value of Gr, Gr $= 0.12$ (blue) and Gr $= 0.21$ (red) and Gr $= 1.0$ (black). In these simulations $\tilde{g} = 4$ and $\tilde{\eta}_t = 10^{-3}$ (blue line), $\tilde{g} = 3.5$, $\tilde{\eta}_t = 2 \times 10^{-3}$ (red line) and $\tilde{g} = 3.5$, $\tilde{\eta}_t = 9.5 \times 10^{-3}$ (black line).

field, but the same value of Gr, the growth rate of NEMPI is in most cases below that of the coupled system with NEMPI and dynamo instability.

In Fig. 10 we see that the dependence of λ/λ_{*0} on Gr is opposite for small and large values of Co. When Co $\lesssim 0.05$, an increase in Gr leads to a decrease in λ/λ_{*0} (compare the Gr $= 1$ line with that for 0.21 along a cut through Co $= 0.05$ in Fig. 10), while for Co $\gtrsim 0.2$, an increase in Gr leads to an increase in λ/λ_{*0} (compare all three lines in Fig. 10 along a cut through Co $= 0.3$). The latter is caused by the increase of the dynamo number C_α, which is directly proportional to Gr; see Eq. (37). On the other hand, for small values of Co, only NEMPI operates, but if Gr in Eq. (38) is increased by increasing $\tilde{\eta}_t$ rather than $\tilde{g}$, the dynamo is suppressed by enhanced turbulent diffusion; see also Fig. 9. This is related to the fact that the properties of the system depend not just on Gr and Co, but also on k_f/k_1 or C_α, which is proportional to all three parameters; see Eq. (37).

4. Discussion and conclusions

The present work has been a step further in trying to determine whether the observable solar activity such as sunspots and active regions could be the result of surface effects associated with strong stratification. A particularly important aspect has been the interaction with a dynamo process that must eventually be responsible for generating the overall magnetic field. Recent global convective dynamo simulations of Nelson et al. (2011, 2013, 2014) have demonstrated that flux tubes with $\approx 40\,\mathrm{kG}$ field strength can be produced in the solar convection zone. This is almost as strong as the $\approx 100\,\mathrm{kG}$ magnetic flux tubes anticipated from earlier investigations of rising flux tubes requiring them to not break up and to preserve their east–west orientation D'Silva & Choudhuri (1993). Would we then still need surface effects such as NEMPI to produce sunspots? The answer might well be yes, because the flux ropes that have been isolated in the visualizations of Nelson et al. (2011, 2013, 2014) appear to have cross-sections that are much larger than sunspots at the solar surface. Further concentration into thinner tubes would be required if they were to explain sunspots by just letting them pierce the surface.

Realistic hydromagnetic simulations of the solar surface are now beginning to demonstrate that $\approx 10\,\mathrm{kG}$ fields at a depth of $\approx 10\,\mathrm{Mm}$ can produce sunspot-like appearances at the surface (Rempel & Cheung, 2014). However, we have to ask about the physical process contributing to this phenomenon. A purely descriptive analysis of simulation data cannot replace the need for a more prognostic approach that tries to reproduce the essential physics using simpler models. Although Rempel & Cheung (2014) propose a mechanism involving mean-field terms in the induction equation, they do not show that their model equations can actually describe the process of magnetic flux concentration. In fact, their description is somewhat reminiscent of flux expulsion, which was invoked earlier by Tao et al. (1998) to explain the segregation of magneto-convection into magnetized and unmagnetized regions. In this context, NEMPI provides such an approach that can be used prognostically rather than diagnostically. However, this approach has problems of its own, some of which are now addressed in the present work. Does NEMPI stop working when Co $\gtrsim 0.03$? How does it interact with the underlying dynamo? Such a dynamo is believed to control the overall sunspot number and the concentration of sunspots to low latitudes.

Our new DNS suggest that, although rotation tends to suppress NEMPI, magnetic flux concentrations can still form at Coriolis numbers of Co ≈ 0.1. This is slightly larger than what was previously found from MFS both with horizontal and vertical magnetic fields and the same value of Gr. For the solar rotation rate of $\Omega \approx 3 \times 10^{-6}\,\mathrm{s}^{-1}$, a value of Co $\equiv 2\Omega\tau = 0.1$ corresponds to $\tau = 5\,\mathrm{h}$, which is longer than the earlier MFS values of $2\,\mathrm{h}$ for a horizontal field (Losada et al., 2013) and $30\,\mathrm{min}$ for a vertical field (Brandenburg et al., 2014).

Using the TFM, we have confirmed earlier findings about α and η_t, although for our new simulations both coefficients are somewhat larger, which is presumably due to the larger scale separation. The ratio between α and η_t determines the dynamo number and is now about 40% below previous estimates. There is no evidence for other important mean-field effects that could change our conclusion about a cross-over from suppressed NEMPI to increased dynamo activity. We now confirm quantitatively that the enhanced growth past the initial suppression of NEMPI is indeed caused by mean-field dynamo action in the presence of a weak magnetic field. The position of the minimum in the growth rate coincides with the onset of mean-field dynamo action that takes the α effect into account.

For weak or no rotation, we find that the normalized NEMPI growth rate is well described by a single parameter Gr, which is proportional to the product of gravity and turbulent diffusivity, where the latter is a measure of the inverse scale separation ratio. This normalization takes into account that the growth rate increases with increasing gravity. The growth rate 'compensated' in that way shows a decrease with increasing gravity and turbulent diffusivity that is different from an earlier, more heuristic, expression proposed by Kemel et al. (2013). The reason for this departure is not quite clear. One possibility is some kind of 'gravitational quenching', because the suppression is well described by a quenching factor that becomes important when Gr exceeds a value of around 0.5. This quenching is probably not important for stellar convection where the estimated value of Gr is 0.17 (Losada et al., 2013). It might, however, help explaining mismatches in the theoretically expected growth rate that was found to be proportional to Gr (Kemel et al., 2013) and that determined from recent DNS (Brandenburg et al., 2014).

An important question is whether NEMPI will really be strong enough to produce sunspots with super-equipartition

strength. It was always clear that NEMPI can only work for a magnetic fields strength is a small fraction of the local equipartition field value. However, super-equipartition fields are being produced if the magnetic field is vertical (Brandenburg et al., 2013). Subsequent work showed quantitatively that NEMPI does indeed work at sub-equipartition field strengths, but since mass flows mainly along magnetic field lines, the reduced pressure leads to suction with tends to evacuate the upper parts of the tube (Brandenburg et al., 2014). This is similar to the "hydraulic effect" envisaged by Parker (1976), who predicted such downflows along flux tubes. In a later paper Parker (1978), gives more realistic estimates, but the source of downward flows remained unclear. Meanwhile, the flux emergence simulations of Rempel & Cheung (2014) show at first upflows in their magnetic spots (see their Fig. 5), but as the spots mature, a downflow develops (see their Fig. 7). In their case, because they have convection, those downflows can also be ascribed to supergranular downflows, as was done by Stein & Nordlund (2012). Nevertheless, in the isothermal simulations of Brandenburg et al. (2013, 2014), this explanation would not apply. Thus, we now know that the required downflows *can* be caused by NEMPI, but he do not know whether this is also what is happening in the Sun.

Coming back to our paper, where NEMPI is coupled to a dynamo, the recent work of Mitra et al. (2014) is relevant because it shows that intense bipolar spots can be generated in an isothermal simulation with strongly stratified non-helically driven turbulence in the upper part and a helical dynamo in the lower part. The resulting surface structure resembles so-called δ spots that have previously only been found in the presence of strongly twisted and kink-unstable flux tubes (Linton et al., 1998). While the detailed mechanism of this work is not yet understood, it reminds us that it is too early to draw strong conclusions about NEMPI as long as not all its aspects have been explored in sufficient detail.

Acknowledgements. This work was supported in part by the European Research Council under the AstroDyn Research Project No. 227952, the Swedish Research Council under the grants 621-2011-5076 and 2012-5797, the Research Council of Norway under the FRINATEK grant 231444 (AB, IR), and a grant from the Government of the Russian Federation under contract No. 11.G34.31.0048 (NK, IR). We acknowledge the allocation of computing resources provided by the Swedish National Allocations Committee at the Center for Parallel Computers at the Royal Institute of Technology in Stockholm and the Nordic Supercomputer Center in Reykjavik.

References

Blackman, E. G., & Brandenburg, A. 2002, ApJ, 579, 359
Brandenburg, A. 2005a, ApJ, 625, 539
Brandenburg, A. 2005b, Astron. Nachr., 326, 787
Brandenburg, A., Gressel, O., Jabbari, S., Kleeorin, N., & Rogachevskii, I. 2014, A&A, 562, A53
Brandenburg, A., Kemel, K., Kleeorin, N., Mitra, D., & Rogachevskii, I. 2011, ApJ, 740, L50
Brandenburg, A., Kemel, K., Kleeorin, N., & Rogachevskii, I. 2012a, ApJ, 749, 179
Brandenburg, A., Kleeorin, N., & Rogachevskii, I. 2013, ApJ, 776, L23
Brandenburg, A., Rädler, K.-H., & Kemel, K. 2012b, A&A, 539, A35
Brandenburg, A., Rädler, K.-H., Rheinhardt, M., & Käpylä, P. J. 2008a, ApJ, 676, 740
Brandenburg, A., Rädler, K.-H., & Schrinner, M. 2008b, A&A, 482, 739
Caligari, P., Moreno-Insertis, F., & Schüssler, M. 1995, ApJ, 441, 886
Candelaresi, S., & Brandenburg, A. 2013, Phys. Rev. E, 87, 043104
Cheung, M. C. M., Rempel, M., Title, A. M., & Schüssler, M. 2010, ApJ, 720, 233
Choudhuri, A. R., Chatterjee, P., & Jiang, J. 2007, Phys. Rev. Lett., 98, 131103
D'Silva, S., & Choudhuri, A. R. 1993, A&A, 272, 621
Emonet, T., & Moreno-Insertis, F. 1998, ApJ, 492, 804
Fan, Y. 2008, ApJ, 676, 680
Fan, Y. 2009, Living Rev. Solar Phys., 6, 4
Hale, G. E., Ellerman, F., Nicholson, S. B., & Joy, A. H. 1919, ApJ, 49, 153
Jabbari, S., Brandenburg, A., Kleeorin, N., Mitra, D., & Rogachevskii, I. 2013, A&A, 556, A106
Jouve, L., Brun, A. S., & Aulanier, G. 2013, ApJ, 762, 23
Kemel, K., Brandenburg, A., Kleeorin, N., & Rogachevskii, I. 2012a, Astron. Nachr., 333, 95
Kemel, K., Brandenburg, A., Kleeorin, N., Mitra, D., & Rogachevskii, I. 2012b, Solar Phys., 280, 321
Kemel, K., Brandenburg, A., Kleeorin, N., Mitra, D., & Rogachevskii, I. 2013, Solar Phys., 287, 293
Kitchatinov, L. L. & Mazur, M. V. 2000, Solar Phys., 191, 325
Kleeorin, N., & Rogachevskii, I. 1994, Phys. Rev. E, 50, 2716
Kleeorin, N., & Rogachevskii, I. 2003, Phys. Rev. E, 67, 026321
Kleeorin, N., Mond, M., & Rogachevskii, I. 1996, A&A, 307, 293
Kleeorin, N.I., Rogachevskii, I.V., & Ruzmaikin, A.A. 1989, Sov. Astron. Lett., 15, 274
Kleeorin, N. I., Rogachevskii, I. V., Ruzmaikin, A. A. 1990, Sov. Phys. JETP, 70, 878
Krause, F., & Rädler, K.-H. 1980, Mean-field Magnetohydrodynamics and Dynamo Theory (Oxford: Pergamon Press)
Leighton, R. B. 1969, ApJ, 156, 1
Linton, M. G., Dahlburg, R. B., Fisher, G. H., & Longcope, D. W. 1998, ApJ, 507, 404
Losada, I. R., Brandenburg, A., Kleeorin, N., Mitra, D., & Rogachevskii, I. 2012, A&A, 548, A49
Losada, I. R., Brandenburg, A., Kleeorin, N., & Rogachevskii, I. 2013, A&A, 556, A83
Miesch, M. S., & Dikpati, M. 2014, ApJ, 785, L8
Mitra, D., Brandenburg, A., Kleeorin, N., & Rogachevskii, I. 2014, MNRAS, submitted, arXiv:1404.3194
Moffatt, H.K. 1978, Magnetic Field Generation in Electrically Conducting Fluids (Cambridge: Cambridge Univ. Press)
Nelson, N. J., Brown, B. P., Brun, A. S., Miesch, M. S., & Toomre, J. 2011, ApJ, 739, L38
Nelson, N. J., Brown, B. P., Brun, A. S., Miesch, M. S., & Toomre, J. 2013, ApJ, 762, 73
Nelson, N. J., Brown, B. P., Brun, A. S., Miesch, M. S., & Toomre, J. 2014, Solar Phys., 289, 441
Parker, E. N. 1955, ApJ, 121, 491
Parker, E. N. 1975, ApJ, 198, 205
Parker, E. N. 1976, ApJ, 210, 816
Parker, E. N. 1978, ApJ, 221, 368
Pinto, R. F., & Brun, A. S. 2013, ApJ, 772, 55
Rädler, K.-H., Kleeorin, N., & Rogachevskii, I. 2003, Geophys. Astrophys. Fluid Dyn., 97, 249
Rempel, M., & Cheung, M. C. M. 2014, ApJ, 785, 90
Roberts, P. H. & Soward, A. M. 1975, Astron. Nachr., 296, 49
Rogachevskii, I., & Kleeorin, N. 2004, Phys. Rev. E, 70, 046310
Rogachevskii, I. & Kleeorin, N., 2006, Geophys. Astrophys. Fluid Dyn., 100, 243
Rogachevskii, I., & Kleeorin, N. 2007, Phys. Rev. E, 76, 056307
Schüssler, M. 1980, Nature, 288, 150
Schüssler, M. 1983, in Solar and stellar magnetic fields: origins and coronal effects, ed. J. O. Stenflo (Reidel), 213
Steenbeck, M., & Krause, F. 1969, Astron. Nachr., 291, 49
Stein, R. F., & Nordlund, Å. 2012, ApJ, 753, L13
Sur, S., Brandenburg, A., & Subramanian, K. 2008, MNRAS, 385, L15
Tao, L., Weiss, N. O., Brownjohn, D. P., & Proctor, M. R. E. 1998, ApJ, 496, L39
Warnecke, J., Losada, I. R., Brandenburg, A., Kleeorin, N., & Rogachevskii, I. 2013, ApJ, 777, L37

III

A&A 562, A53 (2014)
DOI: 10.1051/0004-6361/201322681

Astronomy & Astrophysics

Mean-field and direct numerical simulations of magnetic flux concentrations from vertical field

A. Brandenburg[1,2], O. Gressel[1,3], S. Jabbari[1,2], N. Kleeorin[4,1,5], and I. Rogachevskii[4,1,5]

[1] Nordita, KTH Royal Institute of Technology and Stockholm University, Roslagstullsbacken 23, 10691 Stockholm, Sweden
e-mail: brandenb@nordita.org
[2] Department of Astronomy, AlbaNova University Center, Stockholm University, 10691 Stockholm, Sweden
[3] Niels Bohr International Academy, Niels Bohr Institute, Blegdamsvej 17, 2100 Copenhagen Ø, Denmark
[4] Department of Mechanical Engineering, Ben-Gurion University of the Negev, POB 653, 84105 Beer-Sheva, Israel
[5] Department of Radio Physics, N. I. Lobachevsky State University of Nizhny Novgorod, Russia

Received 16 September 2013 / Accepted 4 December 2013

ABSTRACT

Context. Strongly stratified hydromagnetic turbulence has previously been found to produce magnetic flux concentrations if the domain is large enough compared with the size of turbulent eddies. Mean-field simulations (MFS) using parameterizations of the Reynolds and Maxwell stresses show a large-scale negative effective magnetic pressure instability and have been able to reproduce many aspects of direct numerical simulations (DNS) regarding growth rate, shape of the resulting magnetic structures, and their height as a function of magnetic field strength. Unlike the case of an imposed horizontal field, for a vertical one, magnetic flux concentrations of equipartition strength with the turbulence can be reached, resulting in magnetic spots that are reminiscent of sunspots.
Aims. We determine under what conditions magnetic flux concentrations with vertical field occur and what their internal structure is.
Methods. We use a combination of MFS, DNS, and implicit large-eddy simulations (ILES) to characterize the resulting magnetic flux concentrations in forced isothermal turbulence with an imposed vertical magnetic field.
Results. Using DNS, we confirm earlier results that in the kinematic stage of the large-scale instability the horizontal wavelength of structures is about 10 times the density scale height. At later times, even larger structures are being produced in a fashion similar to inverse spectral transfer in helically driven turbulence. Using ILES, we find that magnetic flux concentrations occur for Mach numbers between 0.1 and 0.7. They occur also for weaker stratification and larger turbulent eddies if the domain is wide enough. Using MFS, the size and aspect ratio of magnetic structures are determined as functions of two input parameters characterizing the parameterization of the effective magnetic pressure. DNS, ILES, and MFS show magnetic flux tubes with mean-field energies comparable to the turbulent kinetic energy. These tubes can reach a length of about eight density scale heights. Despite being $\lesssim$1% equipartition strength, it is important that their lower part is included within the computational domain to achieve the full strength of the instability.
Conclusions. The resulting vertical magnetic flux tubes are being confined by downflows along the tubes and corresponding inflow from the sides, which keep the field concentrated. Application to sunspots remains a viable possibility.

Key words. sunspots – Sun: magnetic fields – turbulence – magnetic fields – hydrodynamics

1. Introduction

Sunspots and active regions are generally thought to be the result of magnetic fields emerging from deep at the bottom of the solar convection zone (Fan 2009). Alternatively, solar magnetic activity may be a shallow phenomenon (Brandenburg 2005). Several recent simulations with realistic physics of solar turbulent convection with radiative transfer have demonstrated the appearance of magnetic flux concentrations either spontaneously (Kitiashvili et al. 2010; Stein & Nordlund 2012) or as a result of suitable initial conditions (Cheung et al. 2010; Rempel 2011). There is also the phenomenon of magnetic flux expulsion, which has been invoked as an explanation of the segregation of magneto-convection into magnetized, non-convecting regions and non-magnetized, convecting ones (Tao et al. 1998).

The magneto-hydrothermal structure of sunspots has been studied using the thin flux tube approximation (Spruit 1981), in which the stability and buoyant rise of magnetic fields in the solar convection zone has been investigated. This theory has been also applied to vertical magnetic flux tubes, which open up toward the surface. An important property of such tubes is the possibility of thermal collapse, caused by an instability that leads to a downward shift of gas and a more compressed magnetic field structure; see Spruit (1979), who adopted a realistic equation of state including hydrogen ionization. On the other hand, sunspot simulations of Rempel (2011) and others must make an ad hoc assumption about converging flows outside the tube to prevent it from disintegrating due to turbulent convection. This approach also does not capture the generation process, that is now implicitly seen to operate in some of the simulations of Kitiashvili et al. (2010) and Stein & Nordlund (2012).

To understand the universal physical mechanism of magnetic flux concentrations, which has been argued to be a minimal model of magnetic spot formation in the presence of a vertical magnetic field (Brandenburg et al. 2013), we consider here forced turbulence in a strongly stratified isothermal layer without radiation. In the past few years, there has been significant progress in modelling the physics of the resulting magnetic flux concentrations in strongly stratified turbulence via the negative effective magnetic pressure instability (NEMPI). The

physics behind this mechanism is the suppression of total (hydrodynamic plus magnetic) turbulent pressure by a large-scale magnetic field. At large enough magnetic Reynolds numbers, well above unity, the suppression of the total turbulent pressure can be large, leading to a negative net effect. In particular, the effective magnetic pressure (the sum of non-turbulent and turbulent contributions) becomes negative, so that the large-scale negative effective magnetic pressure instability is excited (Kleeorin et al. 1989, 1990, 1993, 1996; Kleeorin & Rogachevskii 1994; Rogachevskii & Kleeorin 2007).

Hydromagnetic turbulence has been studied for decades (Biskamp 1993), but the effects of a large-scale magnetic field on the total pressure are usually ignored, because in the incompressible case the pressure can be eliminated from the problem. This changes when there is gravitational density stratification, even in the limit of small Mach number, because $\boldsymbol{\nabla}\cdot\rho\boldsymbol{U}=0$ implies that $\boldsymbol{\nabla}\cdot\boldsymbol{U}=U_z/H_\rho\neq 0$. Here, $\boldsymbol{U}$ is the velocity, $H_\rho=|\mathrm{d}\ln\rho/\mathrm{d}z|^{-1}$ is the density scale height, and gravity points in the negative z direction. When domain size and gravitational stratification are big enough, the system can become unstable with respect to NEMPI, which leads to a spontaneous accumulation of magnetic flux. Direct numerical simulations (DNS) with large scale separation have been used to verify this mechanism for horizontal magnetic fields (Brandenburg et al. 2011; Kemel et al. 2012a, 2013). In that case significant progress has been made in establishing the connection between DNS and related mean-field simulations (MFS). Both approaches show that the resulting magnetic flux concentrations are advected downward in the nonlinear stage of NEMPI. This is because the effective magnetic pressure is negative, so when the magnetic field increases inside a horizontal flux structure, gas pressure and density are locally increased to achieve pressure equilibrium, thus making the effective magnetic buoyancy force negative. This results in a downward flow ("potato-sack" effect). Horizontal mean magnetic fields are advected downward by this flow and never reach much more than a few percent of the equipartition field strength.

The situation is entirely different for vertical magnetic fields. The downflow draws gas downward along magnetic field lines, creating an underpressure in the upper parts, which concentrates the magnetic field to equipartition field strength with respect to the turbulent kinetic energy density (Brandenburg et al. 2013). The resulting magnetic flux concentrations have superficially the appearance of sunspots. For horizontal fields, spots can also form and they have the appearance of bipolar regions, as has been found in simulations with a coronal layer above a turbulent region (Warnecke et al. 2013). However, to address the exciting possibility of explaining the occurrence of sunspots by this mechanism, we need to know more about the operation of NEMPI with a vertical magnetic field. In particular, we need to understand how it is possible to obtain magnetic field strengths much larger than the optimal magnetic field strength at which NEMPI is excited. We will do this through a detailed examination of magnetic flux concentrations in MFS, where the origin of flows can be determined unambiguously owing to the absence of the much stronger turbulent convective motions.

We complement our studies with DNS and so-called "implicit large-eddy" simulations (ILES), which are comparable to DNS in that they aim to resolve the inertial range of the forced turbulence. ILES differ from DNS in that one does not attempt to resolve the dissipation scale, which is numerically expensive due to resolution requirements. In short, ILES are DNS without explicit physical dissipation coefficients. However, unlike large-eddy simulations, no turbulence parameterization model is used at all to represent the unresolved scales. Lacking explicit dissipation, ILES instead rely on suitable properties of the truncation error of the numerical scheme (Grinstein et al. 2005), which guarantees that kinetic and magnetic energies are dissipated near the grid scale. In the finite-volume code N (Ziegler 2004) that we use for ILES here, dissipation occurs in the averaging step of the Godunov scheme. The advantage of the finite-volume scheme is the ability to capture shocks without explicit or artificial viscosity. This allows us to probe the regime of higher Mach numbers without the requirement to adjust the Reynolds number or grid resolution.

Following earlier work of Brandenburg et al. (2011), we will stick to the simple setup of an isothermal layer. This is not only a computational convenience, but it is also conceptually significant, because it allows us to disentangle competing explanations for sunspot and active region formation. One of them is the idea that active regions are being formed and held in place by the more deeply rooted supergranulation network at 20–40 Mm depth (Stein & Nordlund 2012). In a realistic simulation there will be supergranulation and large-scale downdrafts, but NEMPI also produces large-scale downdrafts in the nonlinear stage of the evolution. However, by using forced turbulence simulations in an isothermal layer, an explanation in terms of supergranulation would not apply.

We emphasize that an isothermal layer can be infinitely extended. Furthermore, the stratification is uniform in the sense that the density scale height is independent of height. Nevertheless, the density varies, so the equipartition magnetic field strength also varies. Therefore, the ratio of the imposed magnetic field strength to the equipartition value varies with height. NEMPI is excited at the height where this ratio is around 3% (Losada et al. 2013). This explains why NEMPI can be arranged to work at any field strength if only the domain is tall enough.

At large domain size, DNS and ILES become expensive and corresponding MFS are an ideal tool to address questions concerning the global shape of magnetic flux concentrations. In that case, significant conceptual simplifications can be achieved by making use of the axisymmetry of the resulting magnetic flux concentrations. We also need to know more about the operation of NEMPI under conditions closer to reality. For example, how does it operate in the presence of larger gravity, larger Mach numbers, and smaller scale separation? This aspect is best being addressed through ILES, where significant dissipation only occurs in shocks.

We consider three-dimensional (3D) domains and compare in some cases with MFS in two-dimensions (2D) using axisymmetry or Cartesian geometry. Here, axisymmetry is adequate for vertical tubes while Cartesian geometry is adequate for vertical sheets of horizontal magnetic field. The MFS provide guidance that is useful for understanding the results of DNS and ILES, so in this paper we begin with MFS, discuss the mechanism of NEMPI and then focus on the dependencies on gravity, scale separation, and Mach numbers using DNS. Finally, we assess the applicability of NEMPI to sunspot formation.

2. Mean-field study of NEMPI

For the analytical study of NEMPI with a vertical field we consider the equations of mean-field MHD for mean magnetic field $\overline{\boldsymbol{B}}$, mean velocity $\overline{\boldsymbol{U}}$, and mean density $\overline{\rho}$ in the anelastic approximation for low Mach numbers, and for large fluid and

magnetic Reynolds numbers,

$$\frac{\partial \overline{\boldsymbol{B}}}{\partial t} = \boldsymbol{\nabla} \times \left(\overline{\boldsymbol{U}} \times \overline{\boldsymbol{B}} - \eta_{\rm t} \mu_0 \overline{\boldsymbol{J}} \right), \tag{1}$$

$$\overline{\rho} \frac{{\rm D}\overline{\boldsymbol{U}}}{{\rm D}t} = -\boldsymbol{\nabla} \overline{p}_{\rm tot} + \mu_0^{-1} (\overline{\boldsymbol{B}} \cdot \boldsymbol{\nabla}) \overline{\boldsymbol{B}} + \overline{\rho} \boldsymbol{g} - \nu_{\rm t} \overline{\rho} \overline{\boldsymbol{Q}}, \tag{2}$$

$$0 = -\boldsymbol{\nabla} \cdot \overline{\rho}\, \overline{\boldsymbol{U}}, \tag{3}$$

where ${\rm D}/{\rm D}t = \partial/\partial t + \overline{\boldsymbol{U}} \cdot \boldsymbol{\nabla}$ is the advective derivative, $\overline{p}_{\rm tot} = \overline{p} + p_{\rm eff}$ is the mean total pressure, $\overline{p}$ is the mean gas pressure,

$$p_{\rm eff} = (1 - q_{\rm p}) \overline{\boldsymbol{B}}^2 / 2\mu_0 \tag{4}$$

is the effective magnetic pressure (Kleeorin et al. 1990, 1993, 1996), $\overline{\rho}$ is the mean density, $\overline{\boldsymbol{B}} = \boldsymbol{\nabla} \times \overline{\boldsymbol{A}} + \hat{\boldsymbol{z}} B_0$ is the mean magnetic field with an imposed constant field pointing in the z direction, $\overline{\boldsymbol{J}} = \boldsymbol{\nabla} \times \overline{\boldsymbol{B}} / \mu_0$ is the mean current density, μ_0 is the vacuum permeability, $\boldsymbol{g} = (0, 0, -g)$ is the gravitational acceleration, $\eta_{\rm t}$ is the turbulent magnetic diffusivity, $\nu_{\rm t}$ is the turbulent viscosity,

$$-\overline{\boldsymbol{Q}} = \nabla^2 \overline{\boldsymbol{U}} + \tfrac{1}{3} \boldsymbol{\nabla} \boldsymbol{\nabla} \cdot \overline{\boldsymbol{U}} + 2 \overline{\mathsf{S}} \boldsymbol{\nabla} \ln \overline{\rho} \tag{5}$$

is a term appearing in the viscous force with

$$\mathsf{S}_{ij} = \tfrac{1}{2} (\overline{U}_{i,j} + \overline{U}_{j,i}) - \tfrac{1}{3} \delta_{ij} \boldsymbol{\nabla} \cdot \overline{\boldsymbol{U}} \tag{6}$$

being the traceless rate-of-strain tensor of the mean flow.

We adopt an isothermal equation of state with $p = \rho c_{\rm s}^2$, where $c_{\rm s} = {\rm const.}$ is the sound speed. In the absence of a magnetic field, the hydrostatic equilibrium solution is then given by $\overline{\rho} = \rho_0 \exp(-z/H_\rho)$, where $H_\rho = c_{\rm s}^2 / g$ is the density scale height.

2.1. Analytical estimates of growth rate of NEMPI

We linearize the mean-field Eqs. (1)–(3) around the equilibrium: $\overline{\boldsymbol{U}}_0 = \boldsymbol{0}$, $\overline{\boldsymbol{B}} = \overline{\boldsymbol{B}}_0 = {\rm const.}$ The equations for small perturbations (denoted by a tilde) can be rewritten in the form

$$\frac{\partial \tilde{\boldsymbol{B}}}{\partial t} = \boldsymbol{\nabla} \times \left(\tilde{\boldsymbol{U}} \times \overline{\boldsymbol{B}}_0 \right), \tag{7}$$

$$\boldsymbol{\nabla} \cdot \tilde{\boldsymbol{U}} = \frac{\tilde{U}_z}{H_\rho}, \tag{8}$$

$$\frac{\partial \tilde{\boldsymbol{U}}}{\partial t} = \frac{1}{\overline{\rho}} \left[\mu_0^{-1} (\overline{\boldsymbol{B}}_0 \cdot \boldsymbol{\nabla}) \tilde{\boldsymbol{B}} - \boldsymbol{\nabla} \tilde{p}_{\rm eff} \right], \tag{9}$$

where

$$\tilde{p}_{\rm tot} = \tilde{p}_{\rm eff} = \frac{2 \overline{B}_0 \tilde{B}_z}{\mu_0} \left(\frac{{\rm d}\mathcal{P}_{\rm eff}}{{\rm d}\beta^2} \right)_{\beta = \beta_0} \tag{10}$$

with $\beta = \overline{B} / B_{\rm eq}$ and $B_{\rm eq} = \sqrt{\mu_0 \overline{\rho}}\, u_{\rm rms}$ is the local equipartition field strength, and $u_{\rm rms}$ is assumed to be a constant in the present mean-field study. Here, the effective magnetic pressure is written in normalized form as

$$\mathcal{P}_{\rm eff}(\beta) \equiv \mu_0 p_{\rm eff} / B_{\rm eq}^2 = \tfrac{1}{2} \left[1 - q_{\rm p}(\beta) \right] \beta^2. \tag{11}$$

In this section, we neglect dissipative terms such as the turbulent viscosity term in the momentum equation and the turbulent magnetic diffusion term in the induction equation. We consider the axisymmetric problem, use cylindrical coordinates r, φ, z and introduce the magnetic vector potential and stream function:

$$\tilde{\boldsymbol{B}} = \boldsymbol{\nabla} \times \left(A \mathsf{e}_\varphi \right), \quad \overline{\rho}\, \tilde{\boldsymbol{U}} = \boldsymbol{\nabla} \times \left(\Psi \mathsf{e}_\varphi \right). \tag{12}$$

Using the radial component of Eqs. (7) and (9) we arrive at the following equation for the function $\Phi(t, r, z) = \overline{\rho}^{-1} \nabla_z \Psi$:

$$\frac{\partial^2 \Phi}{\partial t^2} = v_{\rm A}^2(z) \left[\nabla_z^2 + 2 \left(\frac{{\rm d}\mathcal{P}_{\rm eff}}{{\rm d}\beta^2} \right)_{\beta = \beta_0} \Delta_{\rm s} \right] \Phi, \tag{13}$$

where $v_{\rm A}(z) = \overline{B}_0 / \sqrt{\mu_0 \overline{\rho}(z)}$ is the mean Alfvén speed, $\Delta_{\rm s}$ is the radial part of the Stokes operator,

$$\Delta_{\rm s} = \frac{1}{r} \frac{\partial}{\partial r} \left(r \frac{\partial}{\partial r} \right) - \frac{1}{r^2},$$

and we have used an exponential profile for the density stratification in an isothermal layer,

$$\overline{\rho} = \overline{\rho}_0 \exp(-z/H_\rho). \tag{14}$$

We seek solutions of Eq. (13) in the form

$$\Phi(t, r, z) = \exp(\lambda t)\, J_1(\sigma r / R)\, \Phi_0(z), \tag{15}$$

where $J_1(x)$ is the Bessel function of the first kind, which satisfies the Bessel equation: $\Delta_s J_1(ar) = -a^2 J_1(ar)$. Substituting Eq. (15) into Eq. (13), we obtain the equation for the function $\Phi_0(z)$:

$$\frac{{\rm d}^2 \Phi_0}{{\rm d}z^2} - \left[\frac{\lambda^2}{v_{\rm A}^2(z)} + \frac{2\sigma^2}{R^2} \left(\frac{{\rm d}\mathcal{P}_{\rm eff}}{{\rm d}\beta^2} \right)_{\beta = \beta_0} \right] \Phi_0 = 0. \tag{16}$$

For $R^2 \Phi_0''(z) / \Phi_0 \ll 1$, the growth rate of NEMPI is given by

$$\lambda = \frac{v_{\rm A} \sigma}{R} \left[-2 \left(\frac{{\rm d}\mathcal{P}_{\rm eff}}{{\rm d}\beta^2} \right)_{\beta = \beta_0} \right]^{1/2}. \tag{17}$$

This equation shows that, compared to the case of a horizontal magnetic field, where there was a factor H_ρ in the denominator, in the case of a vertical field the relevant length is R/σ. Introducing as a new variable $X = \beta_0^2(z)$, we can rewrite Eq. (16) in the form

$$X^3 \frac{{\rm d}^2 \Phi_0}{{\rm d}X^2} + X^2 \frac{{\rm d}\Phi_0}{{\rm d}X} - \left(\frac{\lambda^2 H_\rho^2}{u_{\rm rms}^2} + \frac{2\sigma^2 H_\rho^2}{R^2} X \frac{{\rm d}\mathcal{P}_{\rm eff}}{{\rm d}X} \right) \Phi_0 = 0. \tag{18}$$

We now need to make detailed assumptions about the functional form of $\mathcal{P}_{\rm eff}(\beta^2)$. A useful parameterization of $q_{\rm p}$ in Eq. (4) is (Kemel et al. 2012b)

$$q_{\rm p} = \frac{q_{\rm p0}}{1 + \beta^2 / \beta_{\rm p}^2} \equiv \frac{\beta_\star^2}{\beta_{\rm p}^2 + \beta^2}, \tag{19}$$

where $\beta_\star = \sqrt{q_{\rm p0}} \beta_{\rm p}$. It is customary to obtain approximate analytic solutions to Eq. (18) as marginally bound states of the associated Schrödinger equation, $\Psi_0'' - \tilde{U}(X) \Psi_0 = 0$, via the transformation $\Phi_0 = \Psi_0 / \sqrt{X}$, where

$$\tilde{U}(X) = \frac{\lambda^2 H_\rho^2}{u_{\rm rms}^2 X^3} - \frac{1}{4X^2} + \frac{\sigma^2 H_\rho^2}{R^2 X^2} \left(1 - \frac{q_{\rm p0}}{(1 + X^2 / \beta_{\rm p}^2)^2} \right), \tag{20}$$

where primes denote a derivative with respect to X. The potential $\tilde{U}(X)$ has the following asymptotic behavior: $\tilde{U} \to \lambda^2 H_\rho^2 / (u_{\rm rms}^2 X^3)$ for small X, and $\tilde{U}(X) \to (\sigma^2 H_\rho^2 / R^2 - 1/4) X^{-2}$ for large X. For the existence of an instability, the potential $\tilde{U}(R)$ should have a negative minimum. However, the exact values of the growth rate of NEMPI, the scale at which the growth rate attains the maximum value, and how the resulting magnetic field structure looks like in the nonlinear saturated regime of NEMPI can only be obtained numerically using MFS.

2.2. MFS models

For consistency with earlier studies, we keep the governing MFS parameters equal to those used in a recent study by Losada et al. (2013). Thus, unless stated otherwise, we use the values

$$q_{\rm p0} = 32, \quad \beta_{\rm p} = 0.058 \quad \text{(reference model)}, \tag{21}$$

which are based on Eq. (22) of Brandenburg et al. (2012), applied to $\mathrm{Re}_M = 18$.

The mean-field equations are solved numerically without making the anelastic approximation, i.e., we solve

$$\frac{\partial \overline{\rho}}{\partial t} = -\boldsymbol{\nabla}\cdot\overline{\rho}\,\overline{\boldsymbol{U}} \tag{22}$$

together with the equations for the mean vector potential $\overline{\boldsymbol{A}}$ such that $\overline{\boldsymbol{B}} = \boldsymbol{B}_0 + \boldsymbol{\nabla}\times\overline{\boldsymbol{A}}$ is divergence-free, the mean velocity $\overline{\boldsymbol{U}}$, and the mean density $\overline{\rho}$, using the Pencil Code[1], which has a mean-field module built in and is used for calculations both in Cartesian and cylindrical geometries. Here, $\boldsymbol{B}_0 = (0, 0, B_0)$ is the imposed uniform vertical field. The respective coordinate systems are (x, y, z) and (r, φ, z). In the former case we use periodic boundary conditions in the horizontal directions, $-L_\perp/2 < (x, y) < L_\perp/2$, while in the latter we adopt perfect conductor, free-slip boundary conditions at the side walls at $r = L_r$ and regularity conditions on the axis. On the upper and lower boundaries at $z = z_{\rm top}$ and $z = z_{\rm bot}$ we use in both geometries stress-free conditions, $\hat{\boldsymbol{z}}\times\partial\overline{\boldsymbol{U}}/\partial z = \boldsymbol{0}$ and $\hat{\boldsymbol{z}}\cdot\overline{\boldsymbol{U}} = 0$, and assume the magnetic field to be normal to the boundary, i.e., $\hat{\boldsymbol{z}}\times\overline{\boldsymbol{B}} = \boldsymbol{0}$.

Following earlier work, we display results for the magnetic field either by normalizing with B_0, which is a constant, or by normalizing with $B_{\rm eq}$, which decreases with height. The strength of the imposed field is often specified in terms of $B_{\rm eq0} = B_{\rm eq}(z = 0)$.

2.3. Nondimensionalization

Nondimensional parameters are indicated by tildes and hats, and include $\tilde{B}_0 = B_0/(\mu_0\rho_0 c_{\rm s}^2)^{1/2}$ and $\tilde{\eta}_{\rm t} = \eta_{\rm t}/c_{\rm s}H_\rho$, in addition to parameters in Eq. (21) characterizing the functional form of $q_{\rm p}(\beta)$. Additional quantities include $\tilde{k}_{\rm f} = k_{\rm f}H_\rho$ and $\hat{k}_{\rm f} = k_{\rm f}/k_1$, where a hat is used to indicate nondimensionalization that uses quantities other than $c_{\rm s}$ and H_ρ, such as $k_1 = 2\pi/L_\perp$, which is the lowest horizontal wavenumber in a domain with horizontal extent $L_\perp$. For example, $\hat{g} = g/c_{\rm s}^2 k_1$, is nondimensional gravity and $\hat{\lambda} = \lambda H_\rho^2/\eta_{\rm t}$ is the nondimensional growth rate. It is convenient to quote also $B_0/B_{\rm eq0}$ with $B_{\rm eq0} = B_{\rm eq}(z = 0)$. Note that $B_0/B_{\rm eq0}$ is larger than $\tilde{B}_0$ by the inverse of the turbulent Mach number, $\mathrm{Ma} = u_{\rm rms}/c_{\rm s}$. It is convenient to normalize the mean flow by $u_{\rm rms}$ and denote it by a hat, i.e., $\hat{\overline{U}} = \overline{U}/u_{\rm rms}$. Likewise, we define $\hat{\overline{B}} = \overline{B}/B_{\rm eq}$.

In MFS, the value of $\eta_{\rm t}$ is assumed to be given by $\eta_{\rm t0} = u_{\rm rms}/3k_{\rm f}$. Using the test-field method, Sur et al. (2008) found this to be an accurate approximation of $\eta_{\rm t}$. Thus, we have to specify both Ma and $\tilde{k}_{\rm f}$. In most of our runs we use $\mathrm{Ma} = 0.1$ and $\tilde{k}_{\rm f} = 33$, corresponding to $\tilde{\eta}_{\rm t} = 10^{-3}$. Furthermore, $k_{\rm f}$ and H_ρ are in principle not independent of each other either. In fact, mixing length theory suggests $k_{\rm f}H_\rho \approx 6.5$ (Losada et al. 2013), but it would certainly be worthwhile to compute this quantity from high-resolution convection simulations spanning multiple scale heights. However, in this paper, different values of $k_{\rm f}H_\rho$ are considered. With these preparations in place, we can now address questions concerning the horizontal wavelength of the instability and the vertical structure of the magnetic flux tubes.

[1] http://pencil-code.googlecode.com

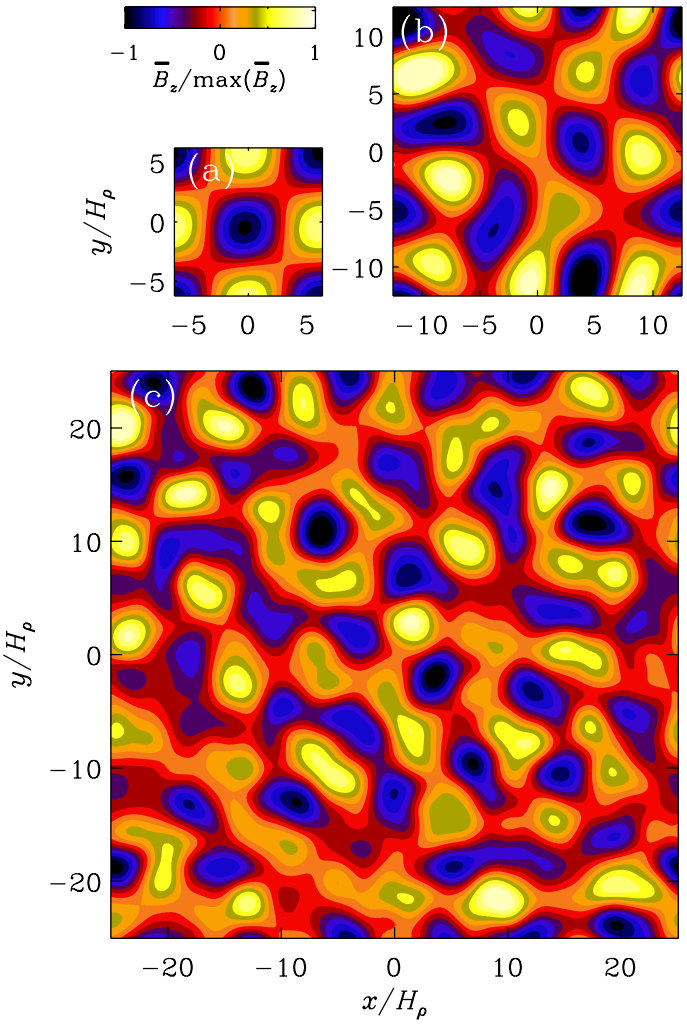

Fig. 1. Horizontal patterns of $\overline{B}_z$ at $z = 0$ from a 3D MFS during the kinematic growth phase with $B_0/B_{\rm eq0} = 0.1$ and horizontal extents with **a)** $L_\perp/H_\rho = 4\pi$; **b)** 8π; and **c)** 16π.

2.4. Aspect ratio of NEMPI

The only natural length scale in an isothermal layer in MFS is H_ρ. It determines the scale of NEMPI. At onset, the horizontal scale of the magnetic field pattern will be a certain multiple of H_ρ. In the following we denote the corresponding horizontal wavenumber of this pattern by $k_\perp$. Earlier work by Kemel et al. (2013) showed that for an imposed horizontal magnetic field we have $k_\perp H_\rho \approx 0.8...1$. This pattern was 2D in the plane perpendicular to the direction of the imposed magnetic field, corresponding to horizontal rolls oriented along the mean magnetic field. In the present case of a vertical field, the magnetic perturbations have a cellular pattern with horizontal wavenumber $k_\perp$. To determine the value of $k_\perp H_\rho$ for the case of an imposed vertical magnetic field, we have to ensure that the number of cells per unit area is independent of the size of the domain. In Fig. 1, we compare MFS with horizontal aspect ratios ranging from 2 to 8. We see that the magnetic pattern is fully captured in a domain with normalized horizontal extent $L_\perp/H_\rho = 4\pi$, i.e., the horizontal scale of the magnetic field pattern is twice the value of H_ρ,

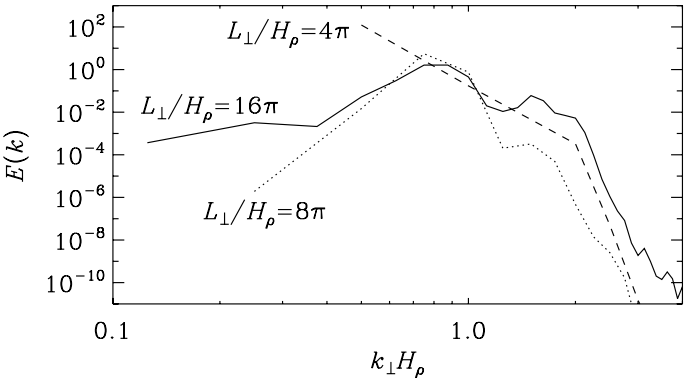

Fig. 2. Power spectra of $\overline{B}_z$ for different horizontal domain sizes at $z = 0$ from a 3D MFS during the kinematic growth phase with $B_0/B_{\rm eq0} = 0.1$.

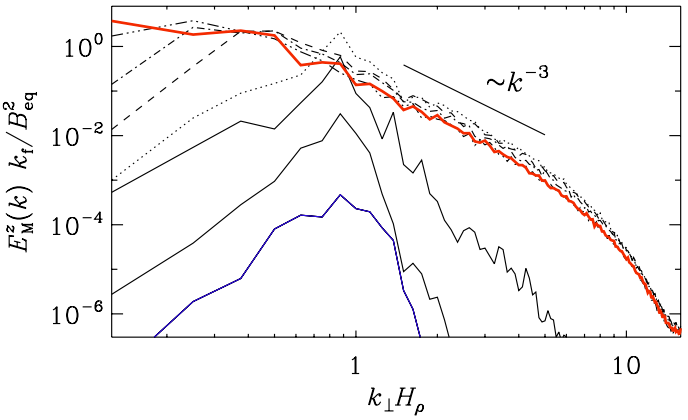

Fig. 3. Time evolution of normalized spectra of B_z from 3D MFS during the late nonlinear phase at the top of the domain, $k_1 z = \pi$, at normalized times $t\eta_{\rm t0}/H_\rho^2 \approx 5$ (blue), 6, 7, 10, 20, 30, 40, and 50 (red), with $g = c_{\rm s}^2 k_1$, $B_0/B_{\rm eq0} = 0.1$, and $L_\perp/H_\rho = 16\pi$.

i.e., $k_x = k_y = H_\rho^{-1}/2$, so that $k_\perp \equiv (k_x^2 + k_y^2)^{1/2} = H_\rho^{-1}/\sqrt{2}$, or $k_\perp H_\rho \approx 0.7$. The value $k_\perp H_\rho \approx 0.7$ is also confirmed by taking a power spectrum of $\overline{B}_z(x, y)$; see Fig. 2, which shows a peak at a similar value.

Comparing the three simulations shown in Fig. 1, we see that a regular checkerboard pattern is only obtained for the smallest domain size; see Fig. 1a. For larger domain sizes the patterns are always irregular such that a cell of one sign can be surrounded by 3–5 cells of the opposite sign. Nevertheless, in all three cases we have approximately the same number of cells per unit area.

In the nonlinear regime, structures continue to merge and more power is transferred to lower horizontal wavenumbers; see Fig. 3. Later in Sect. 3.5 we present similar results also for our DNS.

2.5. Vertical magnetic field profile during saturation

In an isothermal atmosphere, the scale height is constant and there is no physical upper boundary, so we can extend the computation in the z direction at will, although the magnetic pressure will strongly exceed the turbulent pressure at large heights, which can pose computational difficulties. To study the full extent of magnetic flux concentrations, we need a big enough domain. In the following we consider the range $-3\pi \le z/H_\rho \le 3\pi$, which results in a density contrast of more than 10^8. To simplify matters, we restrict ourselves in the present study to axisymmetric calculations which are faster than 3D Cartesian ones.

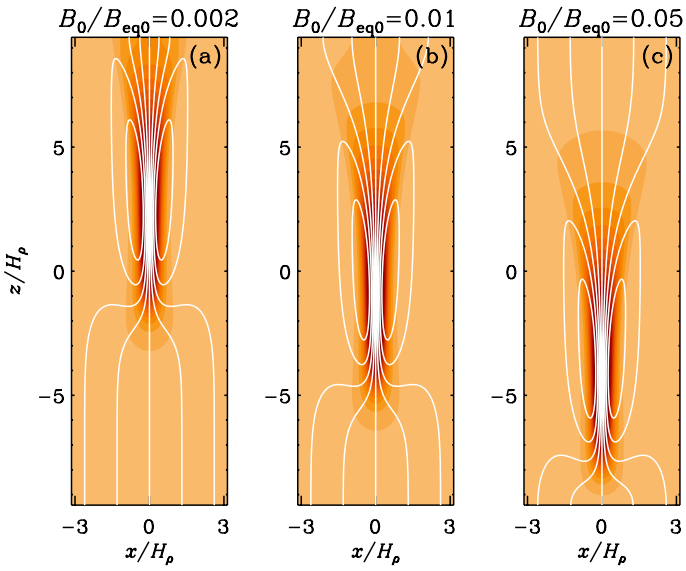

Fig. 4. Comparison of magnetic field profiles from axisymmetric MFS for Runs Bv002/33–Bv05/33 with three values of $B_0/B_{\rm eq0}$ and $\tilde{\eta}_{\rm t} = 10^{-3}$, corresponding to $k_{\rm f} H_\rho = 33$.

In Fig. 4 we compare the results for the mean magnetic field profiles for three values of $B_0/B_{\rm eq0}$ ranging from 0.002 to 0.05. These values are smaller than those studied in Sect. 2.4, because in the nonlinear regime and in a deeper domain the structures are allowed to sink by a substantial amount. By choosing $B_0/B_{\rm eq0}$ to be smaller, the tubes are fully contained in our domain. As B_0 increases, we expect the position of the magnetic flux tube, z_B, to move downward like

$$z_B = z_{B0} - 2H_\rho \ln(B_0/B_{\rm eq0}), \tag{23}$$

where $z_{B0} = 2H_\rho \ln \beta_0^{\rm opt}$ is a reference height and

$$\beta_0^{\rm opt} \equiv B_0/B_{\rm eq}(z_B) \approx 0.03...0.06 \tag{24}$$

is the optimal normalized field strength for NEMPI to be excited (Losada et al. 2013). The validity of Eq. (23) can be verified through Fig. 4, where $B_0/B_{\rm eq0}$ increases by a factor of 25, corresponding to $\Delta z_B = -6.4$.

In all cases, we obtain a slender tube with approximate aspect ratio of 1:8. In other words, the shape of the magnetic field lines is the same for all three values of $B_0/B_{\rm eq0}$, and just the position of the magnetic flux concentration shifts in the vertical direction. Note in particular that the thickness of structures is always the same. This is different from the nonlinear MFS in Cartesian geometry discussed above, where structures are able to merge. Merging is not really possible in the same way in an axisymmetric container, because any additional structure would correspond to a ring.

The mean flow structure associated with the magnetic flux tube is shown in Fig. 5 for Run Bv05/33 with $B_0/B_{\rm eq0} = 0.05$. We find inflow into the tube along field lines at large heights and outflow at larger depth. The vertical component of the flow in the tube points always downward, i.e., there is no obvious effect from positive magnetic buoyancy. The maximum downflow speed is about $0.27 u_{\rm rms}$, so it is subdominant compared with the turbulent velocity, but this could be enough to cause a noticeable temperature change in situations where the energy equation is solved.

The resulting magnetic field lines look roughly similar to those of the DNS with an imposed vertical magnetic field

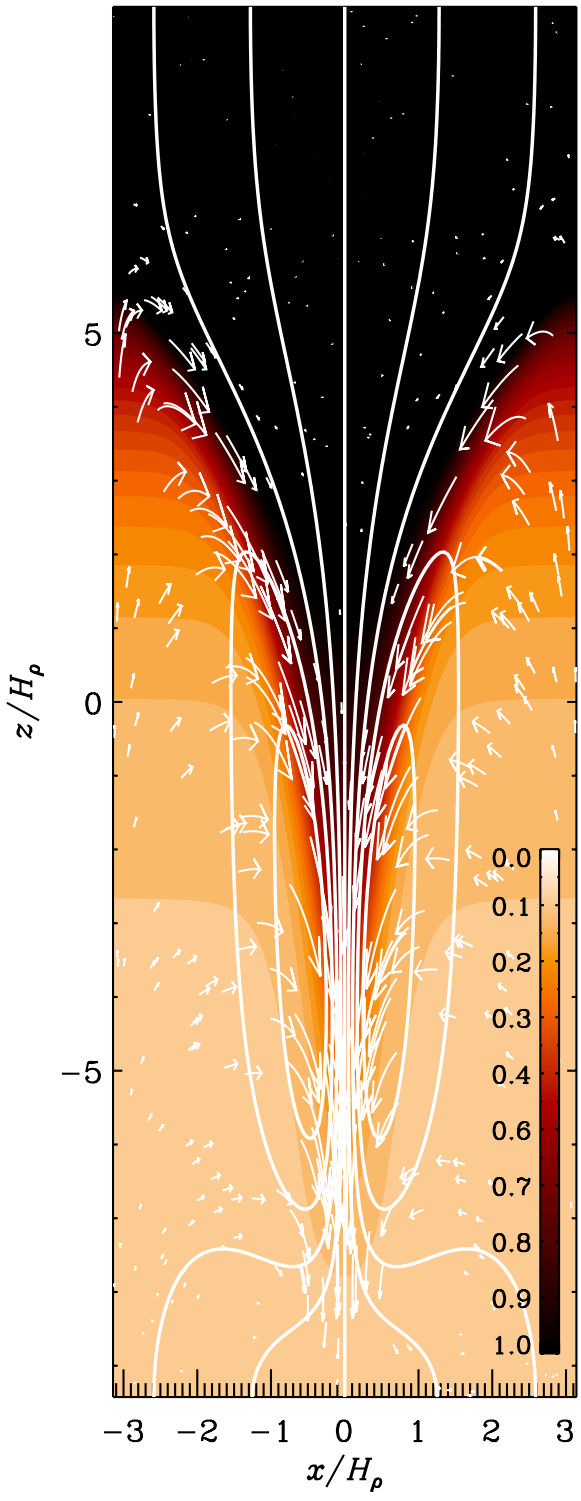

Fig. 5. $\overline{B}_z/B_{\rm eq}$ together with field lines and flow vectors from MFS, for Run Bv05/33 with $B_0/B_{\rm eq0} = 0.05$. The flow speed varies from $-0.27u_{\rm rms}$ (downward) to $0.08u_{\rm rms}$ (upward).

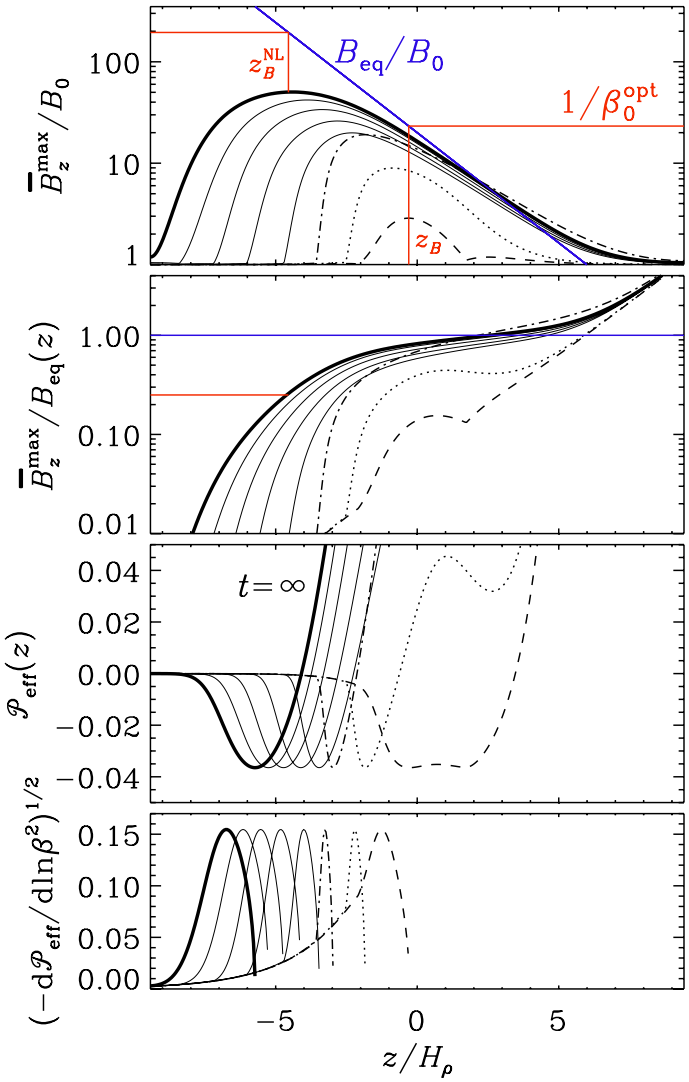

Fig. 6. Time evolution of normalized vertical magnetic field profiles, **a)** $\overline{B}_z^{\rm max}/B_0$ together with $B_{\rm eq}(z)/B_0$ (shown by blue line), **b)** $\overline{B}_z^{\rm max}/B_{\rm eq}(z)$; as well as **c)** $\mathcal{P}_{\rm eff}(z)$ and **d)** $(-{\rm d}\mathcal{P}_{\rm eff}/{\rm d}\ln\beta^2)^{1/2}$, from a MFS for Run Bv05/33 with $B_0/B_{\rm eq0} = 0.05$ at $t/\tau_{\rm td} = 2.9$ (dashed), 3 (dotted), 3.1 (dash-dotted), 3.3, 3.7, 4.2., 5, and 50 (thick solid line). The blue solid lines indicate $B_{\rm eq}(z)$, normalized by **a)** B_0 and **b)** by itself (corresponding thus to unity). The red lines indicate the locations z_B and $z_B^{\rm NL}$, as well as relevant intersections with normalized values of $\overline{B}_z^{\rm max}$ and $B_{\rm eq}$.

(Brandenburg et al. 2013). In DNS, however, the thickness of the magnetic flux tube is larger than in the MFS by about a factor of three. This discrepancy could be explained if the actual value of $\eta_{\rm t}$ was in fact larger than the estimate given by $\eta_{\rm t0}$. We return to this possibility in Sect. 3.5. Alternatively, it might be related to the possibility that the coefficients in Eq. (21) could actually be different.

The time evolution of the vertical magnetic field profiles, $\overline{B}_z^{\rm max}/B_0$ and $\overline{B}_z^{\rm max}/B_{\rm eq}(z)$, is shown in Fig. 6 at different times for the case $B_0/B_{\rm eq0} = 0.05$, corresponding to Fig. 4c. Here, we also show the time evolution of the corresponding profiles of $\mathcal{P}_{\rm eff}(z)$ and $(-{\rm d}\mathcal{P}_{\rm eff}/{\rm d}\ln\beta^2)^{1/2}$. In the kinematic regime, the peak of the latter quantity is a good indicator of the peak of the eigenfunction (Kemel et al. 2013). In the present case, the magnetic field in the kinematic phase peaks at a height z_B that is given by the condition (24). According to the MFS of Losada et al. (2013), this condition is approximately the same for vertical and horizontal fields. Looking at Fig. 6 for $B_0/B_{\rm eq0} = 0.05$, we see that at $z/H_\rho \approx -0.5$ we have $B_{\rm eq}/B_0 \approx 33$, which agrees with Eq. (24). However, unlike the case of a horizontal magnetic field, where in the kinematic phase the mean field was found to peak at a height below that where $(-{\rm d}\mathcal{P}_{\rm eff}/{\rm d}\ln\beta^2)^{1/2}$ peaks, we now see that the field peaks above that position.

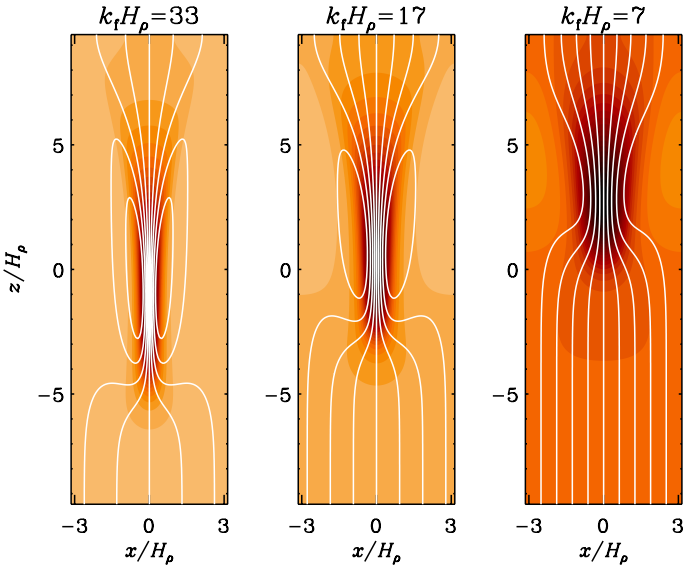

Fig. 7. Comparison of magnetic field profiles from an axisymmetric MFS for Runs Bv01/33–Bv01/7 with $B_0/B_{\rm eq0} = 0.01$ and three values of k_fH_ρ.

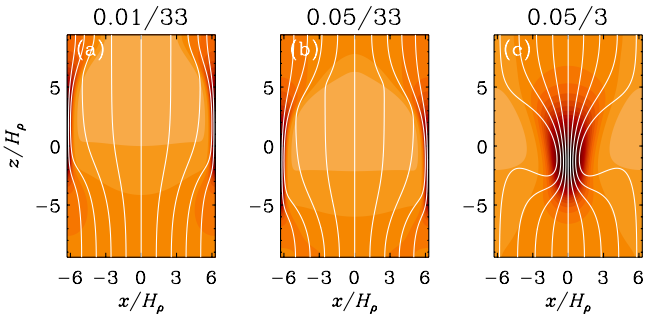

Fig. 8. Comparison of magnetic field structure in axisymmetric MFS. **a)** Run 0.01/33 with $B_0/B_{\rm eq0} = 0.01$ and **b)** Run 0.05/33 with $B_0/B_{\rm eq0} = 0.05$, both with $k_fH_\rho = 33$. The flow speeds vary from $-0.27u_{\rm rms}$ to $0.08u_{\rm rms}$ in both cases. **c)** Run 0.05/3 with $B_0/B_{\rm eq0} = 0.05$ and $k_fH_\rho = 3$. The flow speed varies from $-0.23u_{\rm rms}$ to $0.07u_{\rm rms}$.

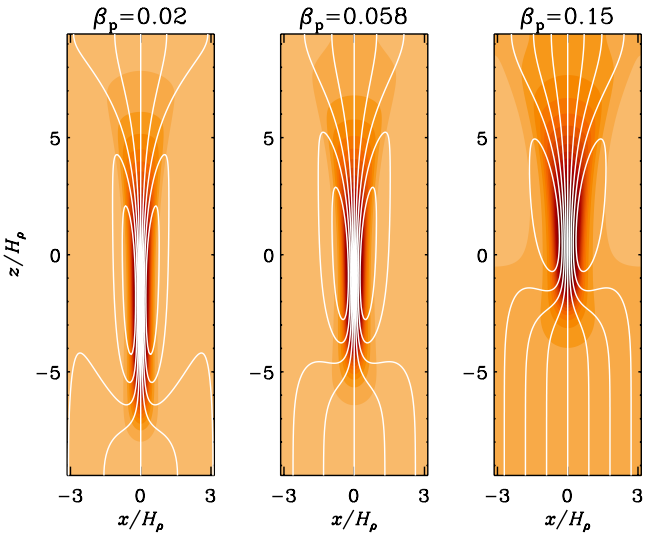

Fig. 9. Comparison of magnetic field structure in axisymmetric MFS for Runs Bu01/33–Bw01/33 with three values of $\beta_{\rm p}$.

As NEMPI begins to saturate, the peak of $\overline{B}_z^{\rm max}$ moves further down to $z = z_B^{\rm NL} \approx -5\,H_\rho$ during the next one or two turbulent diffusive times. By that time, $\overline{B}_z^{\rm max}$ has reached values up to $\overline{B}_z^{\rm max}/B_0 \approx 50$. At that depth, $\overline{B}_z^{\rm max}/B_{\rm eq}(z)$ is about 0.25, but this quantity continues to increase with height and reaches super-equipartition values at $z/H_\rho \approx 3$ (second panel of Fig. 6).

2.6. Smaller scale separation

In MFS, as noted above, the wavenumber of turbulent eddies, $k_{\rm f}$, enters the expression for the turbulent diffusivity via $\eta_{\rm t} \approx u_{\rm rms}/3k_{\rm f}$, and thus $\tilde{\eta}_{\rm t} \approx {\rm Ma}/3\tilde{k}_{\rm f}$, so we have

$$\tilde{k}_{\rm f} \equiv k_{\rm f}H_\rho = H_\rho^2/3\tau\eta_{\rm t} = {\rm Ma}/3\tilde{\eta}_{\rm t}, \quad (25)$$

where $\tau = H_\rho/u_{\rm rms}$ is the turnover time per scale height. When $u_{\rm rms}$ is kept unchanged, smaller scale separation implies a decrease of $\tilde{k}_{\rm f}$, i.e., the size of turbulent eddies in the domain is increased. Earlier work has indicated that the growth rate of the instability for horizontal magnetic field decreases with decreasing $\tilde{k}_{\rm f}$ (Brandenburg et al. 2012). However, we do not know whether this also causes a change in the spot diameter, which would be plausible, or a change in the depth at which NEMPI occurs. In our MFS we have chosen ${\rm Ma} = 0.1$ and $\tilde{\eta}_{\rm t}$ corresponds to $\tilde{k}_{\rm f} \approx 33$. For $\tilde{\eta}_{\rm t} = 5\times10^{-3}$ we have $\tilde{k}_{\rm f} \approx 7$, which is about the smallest scale separation for which NEMPI is still possible in this geometry; see Fig. 7. Interestingly, as $\tilde{k}_{\rm f}$ is decreased, the location of the flux tube structure moves upward. This can be understood as a consequence of enhanced turbulent diffusion, which makes the flux tubes less concentrated, so the magnetic field is weaker, but weaker magnetic field sinks less than stronger fields.

Even for $k_{\rm f}H_\rho \approx 3$ it is still possible to find NEMPI in MFS, but, as we have seen, the flux tube moves upward and becomes thicker. To accommodate for this change, we need to increase the diameter of the domain and, in addition, we would either need to extend it in the upward direction or increase the magnetic field strength to move the tube back down again; cf. Fig. 4. We choose here the latter. In Fig. 8, we show three cases for a wider box. In the first two runs (referred to as "0.01/33" and "0.05/33") we keep the scale separation ratio the same as before, i.e. $\tilde{k}_{\rm f} = 33$, and increase $B_0/B_{\rm eq0}$ from 0.01 to 0.05, while in the third case we keep $B_0/B_{\rm eq0} = 0.05$ and decrease $\tilde{k}_{\rm f}$ to 3. We increase the magnetic field by a factor of 5 so as to keep the structure within the computational domain. In the first case, the natural separation between tubes would be too small for this large cylindrically symmetric container. By contrast, in a 3D Cartesian domain, a second downdraft would form, which is not possible in an axisymmetric geometry. Instead, a downdraft develops on the outer rim of the container. On the other hand, if $\tilde{k}_{\rm f}$ is decreased and thus $\tilde{\eta}_{\rm t}$ increased, a single downdraft is again possible, as shown in Fig. 8b, suggesting that the horizontal scale of structures is also increased as $\tilde{\eta}_{\rm t}$ is increased. We see that the tube can now attain significant diameters. Its height remains unchanged, so the aspect ratio of the structure is decreased as the scale separation ratio is decreased.

2.7. Parameter sensitivity

It is important to know the dependence of the solutions on changes of the parameters $\beta_{\rm p}$ and $\beta_\star$ that determine the function $q_{\rm p}$. In Figs. 9 and 10, we present results where we change either $\beta_{\rm p}$ or $\beta_\star$, respectively. Characteristic properties of these solutions are summarized in Table 1. Runs Ov002/33–Ov05/33

Table 1. Survey of axisymmetric MFS giving normalized growth rates, mean field strengths, mean flow speeds, and other properties for different values of $\beta_0, \beta_\star, \beta_p$, and $\tilde{k}_f$.

Run	β_0	q_{p0}	$\beta_\star$	β_p	β_{min}	$\mathcal{P}_{eff}^{min}$	$\tilde{k}_f$	$\hat{\lambda}$	$\hat{\overline{B}}_z^{max}$	$\hat{\overline{U}}_z^{min}$	$\hat{\overline{U}}_z^{max}$	$\tilde{z}_B$	$\tilde{z}_B^{NL}$	$\tilde{Z}_b$	$\tilde{Z}_t$	$\tilde{R}$	A
Ov002/33	0.002	32	0.33	0.058	0.125	−0.036	33	5.0	52	−0.27	0.03	8.3	4.8	3.5	4.6	0.27	17
Ov01/33	0.01	32	0.33	0.058	0.125	−0.036	33	5.6	52	−0.27	0.08	5.0	1.6	3.6	4.3	0.27	16
Ov05/33	0.05	32	0.33	0.058	0.125	−0.036	33	2.2	51	−0.27	0.08	1.7	−1.7	3.7	4.3	0.27	16
Bv002/33	0.002	32	0.33	0.058	0.125	−0.036	33	7.6	52	−0.27	0.03	7.9	2.0	3.1	4.1	0.35	12
Bv01/33	0.01	32	0.33	0.058	0.125	−0.036	33	9.4	52	−0.27	0.08	3.9	−1.2	3.1	4.1	0.35	12
Bv05/33	0.05	32	0.33	0.058	0.125	−0.036	33	12.3	51	−0.27	0.08	1.8	−4.4	3.0	4.1	0.35	12
Bv01/33	0.01	32	0.33	0.058	0.125	−0.036	33	9.4	52	−0.27	0.08	4.8	−1.2	3.1	4.1	0.35	12
Bv01/17	0.01	32	0.33	0.058	0.125	−0.036	17	2.1	25	−0.27	0.08	4.9	0.3	2.8	4.1	0.50	8
Bv01/7	0.01	32	0.33	0.058	0.125	−0.036	7	0.4	8	−0.23	0.07	4.7	2.7	2.4	3.8	0.95	4
Bu01/33	0.01	270	0.33	0.02	0.079	−0.048	33	5.1	69	−0.35	0.10	4.5	−2.1	4.0	4.5	0.30	15
Bv01/33	0.01	32	0.33	0.058	0.125	−0.036	33	9.4	52	−0.27	0.08	4.8	−1.2	3.1	4.1	0.35	12
Bw01/33	0.01	4.8	0.33	0.15	0.164	−0.016	33	3.2	25	−0.15	0.05	5.4	0.3	2.2	3.8	0.50	8
Av01/33	0.01	12	0.2	0.058	0.091	−0.010	33	2.6	22	−0.13	0.04	4.3	−0.3	2.3	3.8	0.55	7
Bv01/33	0.01	32	0.33	0.058	0.125	−0.036	33	9.4	52	−0.27	0.08	4.8	−1.2	3.1	4.1	0.35	12
Cv01/33	0.01	74	0.5	0.058	0.160	−0.097	33	10.6	91	−0.47	0.09	5.4	−1.7	3.5	4.3	0.25	17
Av01/33*	0.01	12	0.2	0.058	0.091	−0.010	33	2.4	11	−0.07	0.04	4.2	1.6	1.4	3.4	0.85	4
Bv01/33*	0.01	32	0.33	0.058	0.125	−0.036	33	4.8	21	−0.15	0.08	4.7	1.5	1.3	3.3	0.60	5
Cv01/33*	0.01	74	0.5	0.058	0.160	−0.097	33	8.7	33	−0.26	0.10	5.3	1.4	1.2	3.2	0.50	6

Notes. In all cases we have $k_1 H_\rho = 1$, so $\tilde{k}_f = \hat{k}_f$. Asterisks indicate that the domain was clipped at $z_{bot} = 0$.

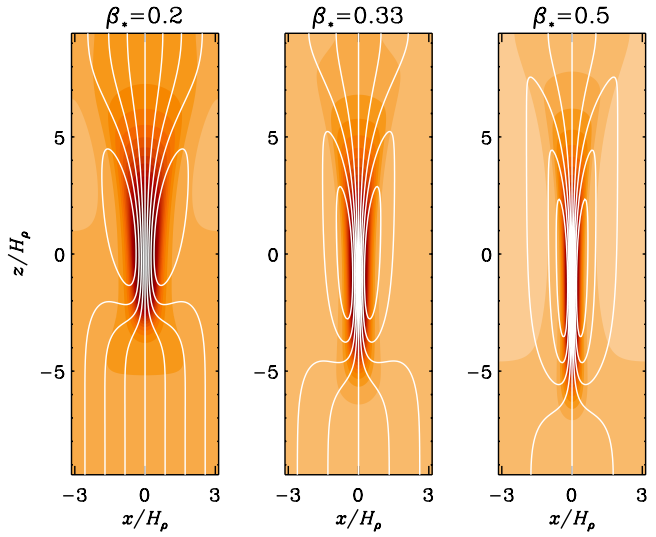

Fig. 10. Comparison of magnetic field structure in axisymmetric MFS for Runs Av01/33–Cv01/33 three values of $\beta_\star$.

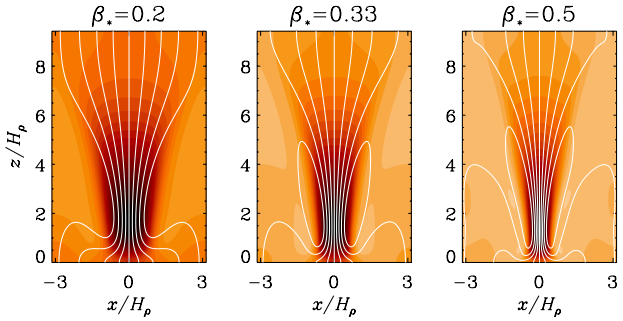

Fig. 11. Comparison of magnetic field structure in axisymmetric MFS for Runs Av–Cv01/33* with three values of $\beta_\star$ in a domain that is truncated from below.

are 2D Cartesian while all other ones are 2D axisymmetric. In addition to β_p and $\beta_\star$, we also list the values of $q_{p0} = \beta_\star^2/\beta_p^2$, as well as the minimum position of the $\mathcal{P}_{eff}(\beta)$ curve, namely (cf. Kemel et al. 2012b)

$$\mathcal{P}_{eff}^{min} = -\tfrac{1}{2}(\beta_\star^2 - \beta_p^2)^2, \quad \beta_{min} = \left(\beta_p \sqrt{-2\mathcal{P}_{eff}^{min}}\right)^{1/2}. \tag{26}$$

The main output parameters include the normalized growth rate in the linear regime, $\hat{\lambda} = \lambda H_\rho^2/\eta_t$, the maximum normalized vertical field in the tube

$$\hat{\overline{B}}_z^{max} = \overline{B}_z^{max}/B_0, \tag{27}$$

the minimum and maximum normalized velocities,

$$\hat{\overline{U}}_z^{min} = \overline{U}_z^{min}/u_{rms}, \qquad \hat{\overline{U}}_z^{max} = \overline{U}_z^{max}/u_{rms}, \tag{28}$$

the normalized maximum magnetic field positions in the linear and nonlinear regimes, $\tilde{z}_B = z_B/H_\rho$ and $\tilde{z}_B^{NL} = z_B^{NL}/H_\rho$, respectively, the similarly normalized positions where $\overline{B}_z$ has dropped by $1/e$ of its maximum at the bottom end $\tilde{Z}_b$, at the top end $\tilde{Z}_t$, and to the side $\tilde{R}$ of the tube, as well as the aspect ratio $A = Z_t/R$.

The changes of $\hat{\lambda}$ are often as expected: a decrease with decreasing values of $\tilde{k}_f$, and a increase with increasing values of $\beta_\star$. There are also some unexpected changes that could be associated with the tube not being fully contained within our fixed domain: for Run Ov05/33 the domain may not be deep enough and for Run Bw01/33 it may not be wide enough. Furthermore, we find that structures become taller when β_p is small and $\beta_\star$ large, and they become shorter and fatter when β_p is large and $\beta_\star$ small. Thus, thicker structures, as indicated by the DNS of Brandenburg et al. (2013), could also be caused by larger values of β_p or smaller values of $\beta_\star$. When the domain is clipped at $z = 0$, flux concentrations cannot fully develop. The structures are fatter and less strong; see Fig. 11.

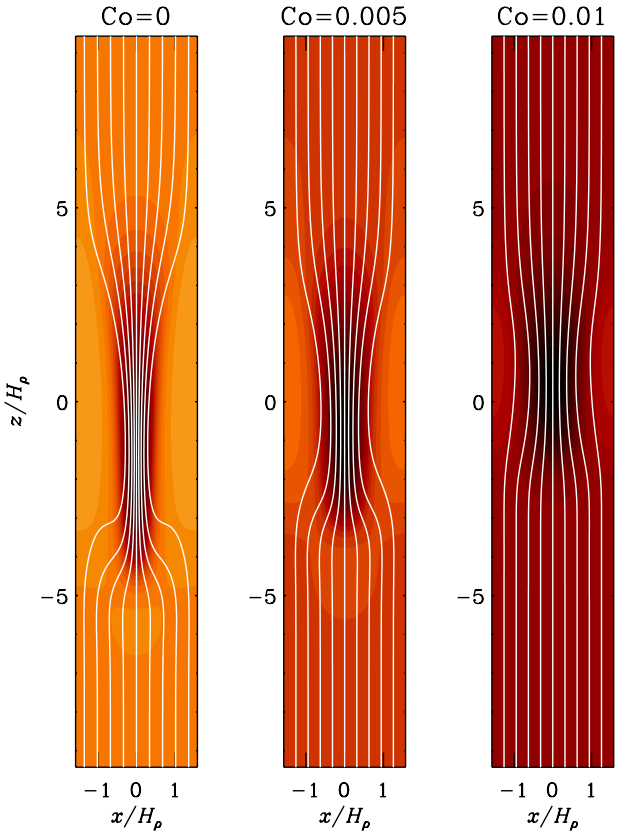

Fig. 12. Comparison of magnetic field structure in axisymmetric MFS for a run similar to Run Bv01/33, but for three values of Co and $r/H_\rho \le \pi/2$.

2.8. Effect of rotation

The effect of rotation through the Coriolis force is determined by the Coriolis number,

$$\mathrm{Co} = 2\Omega/u_{\rm rms}k_{\rm f} = 6\Omega\eta_{\rm t}/u_{\rm rms}^2, \tag{29}$$

where Ω is the angular velocity. Losada et al. (2012, 2013) found that NEMPI begins to be suppressed when $\mathrm{Co} \gtrsim 0.03$, which is a surprisingly small value. They only considered the case of a horizontal magnetic field. In the present case of a vertical magnetic field, we can use the axisymmetric model to include a vertical rotation vector $\boldsymbol{\Omega} = (0, 0, \Omega)$. We add the Coriolis force to the right-hand side of Eq. (2), i.e.,

$$\overline{\rho}\frac{\mathrm{D}\overline{\boldsymbol{U}}}{\mathrm{D}t} = \ldots - 2\boldsymbol{\Omega}\times\overline{\rho}\overline{\boldsymbol{U}}. \tag{30}$$

When adding weak rotation ($\mathrm{Co} = 0.01$) in Run Bv01/33, it turns out that magnetic flux concentrations develop on the periphery of the domain, similar to the case considered in Fig. 8. We have therefore reduced the radial extent of the domain to $r/H_\rho \le \pi/2$. The results are shown in Fig. 12.

In agreement with earlier studies, we find that rather weak rotation suppresses NEMPI. The magnetic structures become fatter and occur slightly higher up in the domain. For $\mathrm{Co} = 0.01$, the magnetic flux concentrations have become rather weak. If we write Co in terms of correlation of turnover time τ as $2\Omega\tau$, we find that the solar values of $\Omega = 3\times10^{-6}\,\mathrm{s}^{-1}$ corresponds to 30 min. According to stellar mixing length theory, this, in turn, corresponds to a depth of less than 2 Mm.

3. DNS and ILES studies

In the MFS discussed above, we have ignored the possibility of other terms in the parameterization of the mean-field Lorentz force. While this seems to capture the essence of earlier DNS (Brandenburg et al. 2013), this parameterization might not be accurate or sufficient in all respects. It is therefore useful to perform DNS to see how the results depend on scale separation, gravitational stratification, and Mach number.

3.1. DNS and ILES models

We have performed direct numerical simulations using both the Pencil Code[2] and N [3]. Both codes are fully compressible and are here used with an isothermal equation of state with $p = \rho c_{\rm s}^2$, where $c_{\rm s} = \mathrm{const}$ is the sound speed. The background stratification is then also isothermal. Turbulence is driven using volume forcing given by a function $\boldsymbol{f}$ that is δ-correlated in time and monochromatic in space. It consists of random non-polarized waves whose direction and phase change randomly at each time step.

In DNS we solve the equations for the velocity $\boldsymbol{U}$, the magnetic vector potential $\boldsymbol{A}$, and the density ρ,

$$\frac{\mathrm{D}\boldsymbol{U}}{\mathrm{D}t} = -c_{\rm s}^2\boldsymbol{\nabla}\ln\rho + \frac{1}{\rho}\boldsymbol{J}\times\boldsymbol{B} + \boldsymbol{f} + \boldsymbol{g} + \boldsymbol{F}_\nu, \tag{31}$$

$$\frac{\partial\boldsymbol{A}}{\partial t} = \boldsymbol{U}\times\boldsymbol{B} + \eta\nabla^2\boldsymbol{A}, \tag{32}$$

$$\frac{\partial\rho}{\partial t} = -\boldsymbol{\nabla}\cdot\rho\boldsymbol{U}, \tag{33}$$

where $\mathrm{D}/\mathrm{D}t = \partial/\partial t + \boldsymbol{U}\cdot\boldsymbol{\nabla}$ is the advective derivative, η is the magnetic diffusivity due to Spitzer conductivity of the plasma, $\boldsymbol{B} = \boldsymbol{B}_0 + \boldsymbol{\nabla}\times\boldsymbol{A}$ is the magnetic field, $\boldsymbol{B}_0 = (0, 0, B_0)$ is the imposed uniform vertical field, $\boldsymbol{J} = \boldsymbol{\nabla}\times\boldsymbol{B}/\mu_0$ is the current density, μ_0 is the vacuum permeability, $\boldsymbol{F}_\nu = \boldsymbol{\nabla}\cdot(2\nu\rho\mathbf{S})$ is the viscous force. The turbulent rms velocity is approximately independent of z. Boundary conditions are periodic in the horizontal directions (so vertical magnetic flux is conserved), and stress free on the upper and lower boundaries, where the magnetic field is assumed to be vertical, i.e., $B_x = B_y = 0$. In the ILES we solve the induction equation directly for $\boldsymbol{B}$, ignore the effects of explicit viscosity and magnetic diffusivity and use an approximate Riemann solver to keep the code stable and to dissipate kinetic and magnetic energies at small scales.

The simulations are characterized by specifying a forcing amplitude, which results in a certain rms velocity, $u_{\rm rms}$, and hence in a certain Mach number. Furthermore, the values of ν and η are quantified through the fluid and magnetic Reynolds numbers, $\mathrm{Re} = u_{\rm rms}/\nu k_{\rm f}$ and $\mathrm{Re}_M = u_{\rm rms}/\eta k_{\rm f}$, respectively. Their ratio is the magnetic Prandtl number, $\mathrm{Pr}_M = \nu/\eta$. Occasionally, we also quote $\tilde{\nu} = \nu/c_{\rm s}H_\rho$ and $\tilde{\eta} = \eta/c_{\rm s}H_\rho$.

An important diagnostics is the vertical magnetic field, B_z, at some horizontal layer. In particular, we use here the Fourier-filtered field, $\overline{B}_z$, which is obtained by removing all components with wavenumbers larger than 1/6 of the forcing wavenumber $k_{\rm f}$. This corresponds to a position in the magnetic energy spectrum where there is a local minimum, so we have some degree of scale separation between the forcing scale and the scale of the spot. We return to this in Sect. 3.5. To identify the magnetic field in the flux tube, we take the maximum of $\overline{B}_z$, either at each height

[2] http://pencil-code.googlecode.com
[3] http://nirvana-code.aip.de/

Table 2. Summary of DNS at varying $\tilde{B}_0$, and fixed values of $\tilde{\eta} = 2\times10^{-4}$, $\mathrm{Pr}_M = 0.5$, $\mathrm{Re} \approx 38$, $\mathrm{Ma} \approx 0.1$, $\hat{g} = 1$, $\hat{k}_\mathrm{f} = 30$, $\tau_\mathrm{td}/\tau_\mathrm{to} \approx 2700$, using 256^3 mesh points.

Run	$\hat{B}_0$	Re	Re_M	Ma	$\hat{B}_z$	$\hat{\overline{B}}_z$	$\tilde{R}$	$\tilde{z}_B^\mathrm{NL}$
(a)	0.0005	39	19	0.12	1.81	0.36	0.13	3.1
(b)	0.0010	39	19	0.12	2.68	1.00	0.11	1.8
(c)	0.0020	38	19	0.11	2.45	0.87	0.17	1.4
(d)	0.0050	37	18	0.11	3.47	1.25	0.22	−0.5
(e)	0.0100	35	18	0.11	3.95	1.49	0.29	−1.2
(f)	0.0200	31	16	0.09	4.21	1.26	0.45	$-\pi$

Notes. In all cases the number of resulting spots is unity. The positions $\tilde{z}_B^\mathrm{NL}$ agree with those marked in Fig. 13.

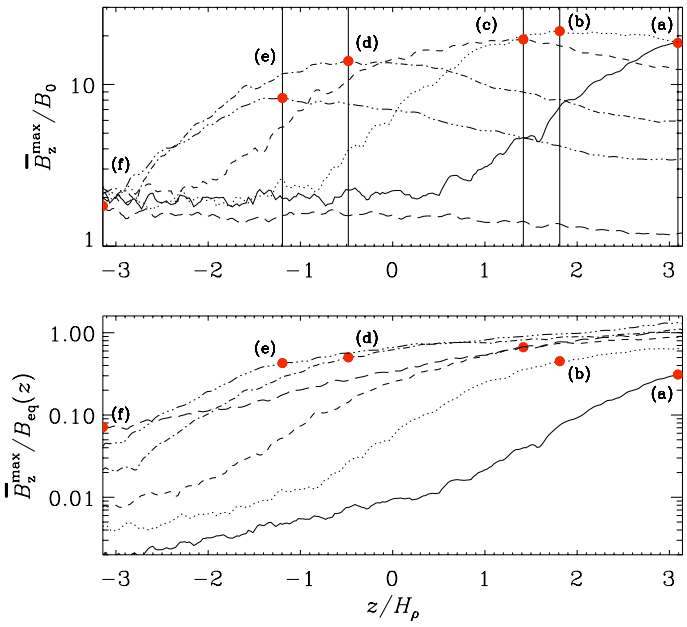

Fig. 13. Normalized vertical magnetic field profiles from DNS, $\overline{B}_z^{\max}/B_0$ (*top*) and $\overline{B}_z^{\max}/B_{\mathrm{eq}}(z)$ (*bottom*) for the six values of $B_0/B_{\mathrm{eq}0}$ listed in Table 2. In both panels, the red dots mark the maxima of $\overline{B}_z^{\max}/B_0$ at positions $\tilde{z}_B^\mathrm{NL}$. The labels (a)–(f) correspond to those in Table 2.

at one time, which is referred to as $\overline{B}_z^{\max}(z)$, or in the top layer at different times. The latter is used to determine the growth rate of the instability.

When comparing results for different values of g, it is convenient to keep the typical density at the surface the same. Since our hydrostatic stratification is given by Eq. (14), this is best done by letting the domain terminate at $z = 0$ and to consider the range $-L_z \le z \le 0$. In most of the cases we consider $L_z = \pi/k_1$, although this might in hindsight be a bit short in some cases. For comparison with earlier work of Brandenburg et al. (2013), we also present models in a domain $-\pi \le k_1 z \le \pi$.

3.2. Magnetic field dependence

In Table 2 and Fig. 13 we compare results for six values of $\tilde{B}_0 = B_0/(\mu_0\rho_0 c_{\mathrm{s}0}^2)^{1/2}$. These models are the same as those discussed in Brandenburg et al. (2013), where visualizations are shown for all six cases. Increasing $\tilde{B}_0$ leads to a decrease in the Mach number Ma and hence to a mild decline of Re and Re_M for $\tilde{B}_0 > 0.01$, corresponding to $B_0/B_{\mathrm{eq}0} > 0.1$. There is a slight increase of $\tilde{B}_z^{\max}$, while $\tilde{\overline{B}}_z^{\max}$ remains on the order of unity. This

Table 3. Summary of DNS at varying Pr_M, and fixed values of $\tilde{\eta} = 2\times10^{-4}$, $\tilde{B}_0 = 0.002$, $\mathrm{Re}_M \approx 20$–40, $\mathrm{Ma} \approx 0.1$, $\hat{g} = 1$, $\hat{k}_\mathrm{f} = 30$, $\tau_\mathrm{td}/\tau_\mathrm{to} \approx 2700$, using 256^3 mesh points.

$\tilde{\nu}$	Pr_M	Re_M	Ma	$\hat{\lambda}$	$\hat{B}_z$	$\hat{\overline{B}}_z$	$\tilde{R}$
4×10^{-5}	0.2	20	0.12	5.18	1.87	0.19	0.36
1×10^{-4}	0.5	19	0.11	1.33	2.45	0.87	0.17
2×10^{-4}	1	17	0.10	1.66	2.76	0.84	0.17
4×10^{-4}	2	14	0.08	1.46	2.78	0.64	0.20
5×10^{-4}	5	25	0.07	0.10	2.66	0.22	0.34
1×10^{-3}	10	19	0.06	0.04	2.87	0.28	0.30
5×10^{-4}	10	45	0.07	0.04	2.96	0.22	0.34

Notes. In all cases the number of spots is unity.

Table 4. Summary of DNS at varying Re and Re_M, and fixed values of $\tilde{\nu} = 10^{-4}$, $\tilde{B}_0 = 0.002$, $\mathrm{Pr}_M = 0.5$, $k_1 H_\rho = 1$, and $k_\mathrm{f} H_\rho = 30$.

Run	Re	Re_M	Ma	$\hat{B}_z$	$\hat{\overline{B}}_z$	$\tilde{R}$	Resol.
A30/1	38	19	0.11	2.45	0.87	0.17	256^3
B30/1	80	40	0.12	3.30	1.02	0.16	512^3
b30/1	200	40	0.12	3.45	1.10	0.15	512^3
C30/1	190	95	0.11	3.47	0.71	0.19	1024^3
D30/1	190	95	0.11	3.54	0.69	0.19	$1024^2\times1536$
E30/1	190	190	0.11	3.23	0.39	0.25	$1024^2\times1536$

is the case even for the largest value, $\tilde{B}_0 = 0.02$, when NEMPI is completely suppressed and there is no distinct maximum of $\overline{B}_z^{\max}/B_0$ in the upper panel of Fig. 13. This is why the visualization in Brandenburg et al. (2013) was featureless for $\tilde{B}_0 = 0.02$, even though $\tilde{B}_z/B_{\mathrm{eq}}(z) \approx 1$ at $z = z_{\mathrm{top}}$. Moreover, while $\tilde{B}_z^{\max}$ shows only a slight increase, the non-dimensional radius of the spot increases from 0.1 to about 0.4 as $\tilde{B}_0$ is increased.

3.3. Magnetic Prandtl number dependence

The results for different values of Pr_M are summarized in Table 3. It turns out that for $\mathrm{Pr}_M \ge 5$, no magnetic flux concentrations are produced. We recall that analysis based on the quasi-linear approach (which is valid for small fluid and magnetic Reynolds numbers) has shown that for $\mathrm{Pr}_M \ge 8$ and $\mathrm{Re}_M \ll 1$, no negative effective magnetic pressure is possible (Rüdiger et al. 2012; Brandenburg et al. 2012). Because of this, most of the earlier work used $\mathrm{Pr}_M = 0.5$ so as to stay below unity in the hope that this would be a good compromise between Pr_M being small and Re_M still being reasonably large. In fact, it now turns out that the difference in $\overline{B}_z^{\max}$ for $\mathrm{Pr}_M = 1$ and 1/2 be negligible, and even for $\mathrm{Pr}_M = 2$ the decline in $\overline{B}_z^{\max}$ is still small. For $\mathrm{Pr}_M = 0.2$, on the other hand, we find a large value of $\hat{\lambda}$, but a low saturation level. Again, this might be explained by the fact that the domain is not deep enough in the z direction, which can suppress NEMPI. Alternatively, the resolution of 256^3 might not be sufficient to resolve the longer inertial range for smaller magnetic Prandtl numbers. In Sect. 3.4 we present another case with $\mathrm{Pr}_M = 0.2$ where both the resolution and the Reynolds numbers are doubled, and $\overline{B}_z^{\max}$ is again large.

3.4. Reynolds number dependence

Increasing Re_M from 19 to 95, we see some changes; see Table 4. There is first a small increase of $\overline{B}_z^{\max}/B_{\mathrm{eq}}(z)$ from 0.87 to 1.02 as Re_M is increased from 19 to 40 (Run B30/1). Increasing Re

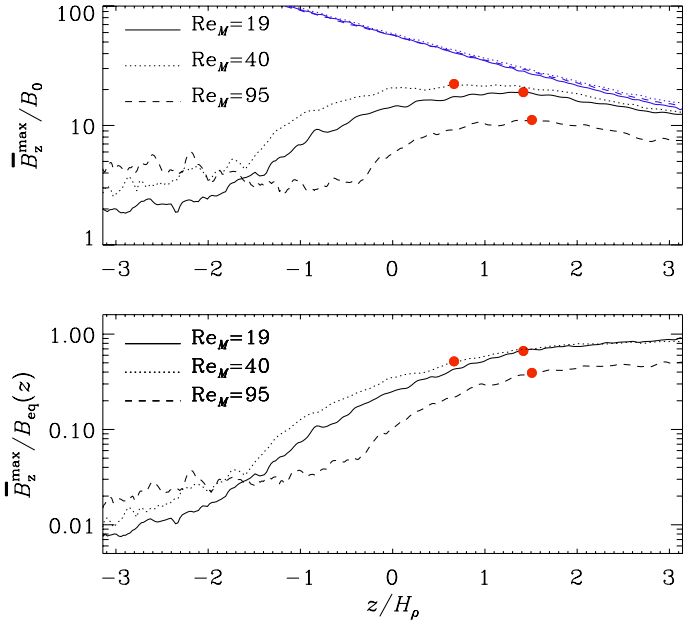

Fig. 14. Similar to Fig. 13, but for DNS Runs A30/1–C30/1 listed in Table 4, i.e., $\tilde{\nu} = 10^{-4}$, $\tilde{B}_0 = 0.002$, $\mathrm{Pr}_M = 0.5$, $k_1 H_\rho = 1$, and $k_{\rm f} H_\rho = 30$. In the *upper panel*, the blue lines denote $B_{\rm eq}(z)/B_0$ and in both panels, the red dots mark the maxima of $\overline{B}_z^{\max}/B_0$ at positions $\tilde{z}_B^{\rm NL}$.

to 200, but keeping $\mathrm{Re}_M = 40$, results in a further increase of $\overline{B}_z^{\max}/B_{\rm eq}(z)$ to 1.10 (Run b30/1). This is also an example of a strong flux concentration with $\mathrm{Pr}_M = 0.2$; cf. Sect. 3.3. However, when Re_M is increased further to 95, $\overline{B}_z^{\max}/B_{\rm eq}(z)$ decreases to about 0.71; see Table 4. Again, the weakening of the spot might be a consequence of the domain not being deep enough. Alternatively, it could be related to the occurrence of small-scale dynamo action, which is indicated by the fact that in deeper layers the small-scale magnetic field is enhanced in the run with the largest value of Re_M; see Fig. 14. In Run C30/1 with the largest value of Re_M, the spot is larger and more fragmented, but it still remains in place and statistically steady; see Fig. 15 and online material[4] for corresponding animations.

To eliminate the possibility of the domain not being deep enough, we have performed additional simulations where we have extended the domain in the negative z direction down to $z_{\rm bot}/H_\rho = -1.5\pi$. In Fig. 16 we show a computation of the resulting profiles of $\overline{B}_z^{\max}/B_0$ and $\overline{B}_z^{\max}/B_{\rm eq}(z)$. We also include here a run with $\mathrm{Pr}_M = 1$ instead of 0.5 (Run E30/1). It turns out that the strength of the spot is unaffected by the position of $z_{\rm bot}$ and that there is a deep layer below $z/H_\rho \approx -2$ in which there is significant magnetic field generation owing to small-scale dynamo action, preventing thereby also the value of $\overline{B}_z^{\max}/B_{\rm eq}(z)$ to drop below the desired value of 0.01. This might explain the weakening of the spot. This is consistent with earlier analytical (Rogachevskii & Kleeorin 2007) and numerical (Brandenburg et al. 2012) work showing a finite drop of the important NEMPI parameter $\beta_\star$ around $\mathrm{Re}_M = 60$.

3.5. Dependence on scale separation and stratification

We have performed various sets of additional simulations where we change $\hat{g}$ and/or $\hat{k}_{\rm f}$; see Table 5 and Fig. 17. In those cases, the vertical extent of the domain is from $-\pi$ to 0. As discussed in Sect. 3.1 this might be too small in some cases for NEMPI to develop fully. Nevertheless, in all cases there are clear indications for the occurrence of flux concentrations. The results regarding the growth rate of NEMPI are not fully conclusive, because the changes in $k_{\rm f}$ and H_ρ also affect turbulent-diffusive and turnover time scales. As shown in the appendix of Kemel et al. (2013) the normalized growth rate of NEMPI is given by:

$$\hat{\lambda} + 1 = 3\beta_\star\,(k_{\rm f}H_\rho)/(k_\perp H_\rho)^2, \tag{34}$$

which is not changed significantly for a vertical magnetic field; see Sect. 2.1. If $k_\perp H_\rho = \mathrm{const.} \approx 0.7$, as suggested by the MFS of Sect. 2.4, we would expect $\hat{\lambda} + 1$ to be proportional to $k_{\rm f}H_\rho$, which is not in good agreement with the simulation results.

To shed some light on this, we now discuss horizontal power spectra of $B_z(x, y)$ taken at the top of the domain. These spectra are referred to as $E_{\rm M}^z(k)$ and are normalized by $B_{\rm eq}^2/k_{\rm f}$. In Run a30/4 with $\hat{g} = 4$ and $\hat{k}_{\rm f} = 30$, we have access to wavenumbers down to $k_1 H_\rho = 0.25$. The results in Fig. 18 show that there is significant power below $k_\perp H_\rho = 0.7$. This is in agreement with the MFS in the nonlinear regime; see Fig. 3. The time evolution of $E_{\rm M}^z(k)$ suggest a behavior similar to that of an inverse magnetic helicity cascade that was originally predicted by (Frisch et al. 1975) and later verified both in closure calculations (Pouquet et al. 1976) and DNS (Brandenburg 2001). Similar results with inverse spectral transfer are shown in Fig. 19 for DNS Run A40/1. The only difference between Runs A40/1 and a40/1 is the vertical extent of the domain, which is twice as tall in the former case ($3\pi H_\rho$ instead of $1.5\pi H_\rho$). We note in this connection that the spectra tend to show a local minimum near $k_{\rm f}/6$. This justifies our earlier assumption of separating mean and fluctuating fields at the wavenumber $k_{\rm f}/6$; see Sect. 3.1. The spectra also show something like an inertial subrange proportional to $k^{-5/3}$ (Fig. 19) or $k^{-2.5}$ (Fig. 18). The latter is close to the k^{-3} subrange in the MFS of Fig. 3. Those steeper spectra could be a symptom of a low Reynolds number or, alternatively, a consequence of most of the energy inversely "cascading" to larger scales in the latter two cases.

We have also checked how different kinds of helicities vary during NEMPI. In the present case, magnetic and kinetic helicities are fluctuating around zero, but cross helicity is not. The latter is an ideal invariant of the magnetohydrodynamic (MHD) equations, but in the present case of a stratified layer with a vertical net magnetic field, $\langle \boldsymbol{u} \cdot \boldsymbol{b} \rangle$ can actually be produced; see Rüdiger et al. (2011), who showed that

$$\langle \boldsymbol{u} \cdot \boldsymbol{b} \rangle \approx \eta_{\rm t} \boldsymbol{g} \cdot \boldsymbol{B}_0 / c_{\rm s}^2 = -\eta_{\rm t} B_0 / H_\rho. \tag{35}$$

In a particular case of Run 30/1, we find a time-averaged value of $\langle \boldsymbol{u} \cdot \boldsymbol{b} \rangle$ that would suggest that $\eta_{\rm t}/\eta_{\rm t0}$ is around 6, which is significantly larger than unity. This would agree with independent

Table 5. Summary of DNS at varying $\hat{k}_{\rm f} = k_{\rm f}/k_1$, $\tilde{k}_{\rm f} = k_{\rm f}H_\rho$, $\hat{g} = g/c_{\rm s}^2 k_1$, and fixed values of $\tilde{B}_0 = 0.02$, $\tilde{\eta}_0 = 2 \times 10^{-4}$, using resolutions of 256^3 mesh points (for Run a30/1), 512^3 mesh points (for Run a30/4, a10/3, and a30/3), as well as $1024^2 \times 384$ mesh points (for Runs a40/1 and A40/1).

Run	Pr_M	Re_M	Ma	$\hat{k}_{\rm f}$	$\tilde{k}_{\rm f}$	$\hat{g}$	$\hat{\lambda}$	$\hat{B}_z$	$\hat{\overline{B}}_z$
a30/1	1.0	16	0.09	30	30	1	0.94	3.09	0.78
a30/4	1.0	21	0.13	30	7.5	4	0.18	4.42	0.88
a10/3	1.0	63	0.13	10	3.4	3	–	4.83	0.40
a40/1	1.0	33	0.07	40	10	1	0.83	3.83	0.87
A40/1	1.0	33	0.07	40	10	1	1.05	5.81	1.41
a30/3	0.5	23	0.14	30	10	3	0.46	4.47	1.31

[4] http://www.nordita.org/~brandenb/movies/NEMPI/

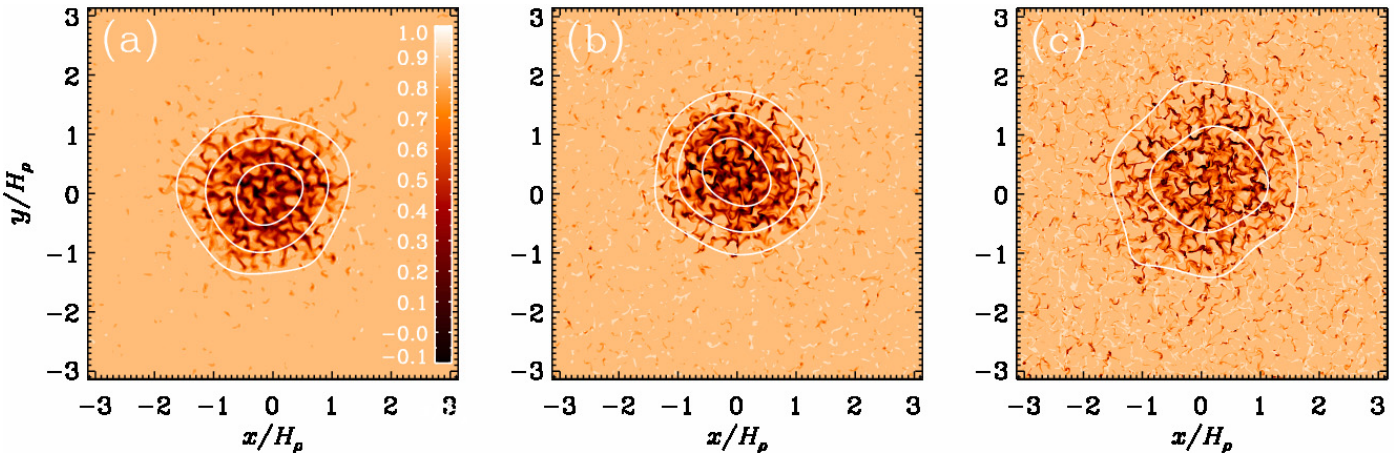

Fig. 15. Magnetic field configuration at the upper surface for DNS Runs A30/1–C30/1 at three values of the magnetic Reynolds number. The white contours represent the Fourier-filtered with $k_\perp \le k_f/6$; their levels correspond to $\overline{B}_z^{max}/B_{eq}(z_{top}) = 0.05$, 0.2, and 0.4.

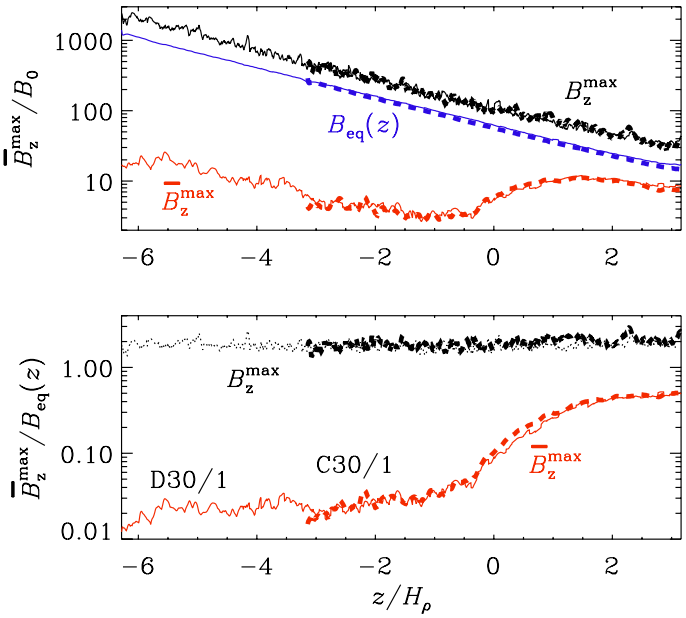

Fig. 16. Similar to Fig. 14, but for DNS Runs C30/1 ($z_{bot}/H_\rho = -\pi$; thicker lines) and D30/1 ($z_{bot}/H_\rho = -1.5\pi$; thinner lines) listed in Table 4, i.e., $\tilde{\nu} = 10^{-4}$, $\tilde{B}_0 = 0.002$, $\mathrm{Pr}_M = 0.5$, $k_1 H_\rho = 1$, and $k_f H_\rho = 30$. In the *upper panel*, the blue lines denote $B_{eq}(z)/B_0$.

arguments in favor of having underestimated η_t; see the discussion in Sect. 2.5. In other words, if η_t were really larger than what is estimated based on the actual rms velocity, it would also explain why the diameter of tubes is bigger in the DNS than in the MFS.

3.6. Mach number dependence

To study the dependence on Mach number, it is useful to consider ILES without any explicit viscosity or magnetic diffusivity. In Figs. 20–22 we show the results for three values of Ma at $\hat{g} = gk_1/c_s^2 = 3$ and $\hat{k}_f = k_f/k_1$ using a resolution of $256^2 \times 128$ nodes on the mesh. In Table 6 we give a summary of various output parameters and compare with corresponding DNS. Note first of all that the results from ILES are generally in good agreement with the DNS. This demonstrates that the mechanism causing magnetic flux concentrations by NEMPI is robust

Table 6. Summary of DNS and ILES at varying values of Ma, all for $\hat{g} = 3$, $\hat{k}_f = 30$.

Run	$\tilde{B}_0$	Re_M	Ma	$\hat{\lambda}$	$\hat{B}_z$	$\hat{\overline{B}}_z$
D01	0.01	24	0.15	0.28	3.06	0.78
D02	0.02	24	0.14	0.46	4.47	1.31
D10	0.10	8	0.50	0.25	4.91	1.61
I03	0.10	–	0.16	>1	2.86	1.14
I10	0.10	–	0.34	>1	2.70	1.00
I30	0.10	–	0.68	>1	2.41	1.02

Notes. For ILES, no accurate values of $\hat{\lambda}$ are available. In the DNS, the resolution is 256^2 for Runs D01 and D02, and 512^2 for Run D10, while for Runs I03–I30 it is $256^2 \times 128$.

and not sensitive to details of the magnetic Reynolds number, provided that $\mathrm{Re}_M \gtrsim 10$. The normalized growth rate is in all three cases above unity.

As the Mach number is increased, the magnetic structures become smaller; seen in the left-hand panels of Fig. 22. Since the properties of NEMPI depend critically on the ratio $\overline{B}_z/B_{eq}$, and since $B_{eq}(z)$ and hence B_{eq0} increase with increasing Mach number, the decrease in the size of magnetic structures might just reflect the fact that for smaller values of $\overline{B}_z/B_{eq0}$, NEMPI would operate at higher layers which are no longer included in our computational domain. Looking at Fig. 20, it is clear that the maximum of $\overline{B}_z/B_0$ moves to higher layers, but it is still well confined within the computational domain. Nevertheless, if one compensates for the decrease of B_{eq} by applying successively weaker mean fields when going to lower Mach number (right-hand panels of Fig. 22), the size of the emerging structures remains approximately similar and the curves of $\overline{B}_z/B_{eq}$ lie now nearly on top of each other. This shows clearly that in our simulations with Ma ≈ 0.7, flux concentrations are well possible. This is important, because it allows for the possibility that the energy density of magnetic flux concentrations can become comparable with the thermal energy.

4. Possible application to sunspot formation

Compared with earlier studies of NEMPI using a horizontal imposed magnetic field, the prospects of applying it to the Sun

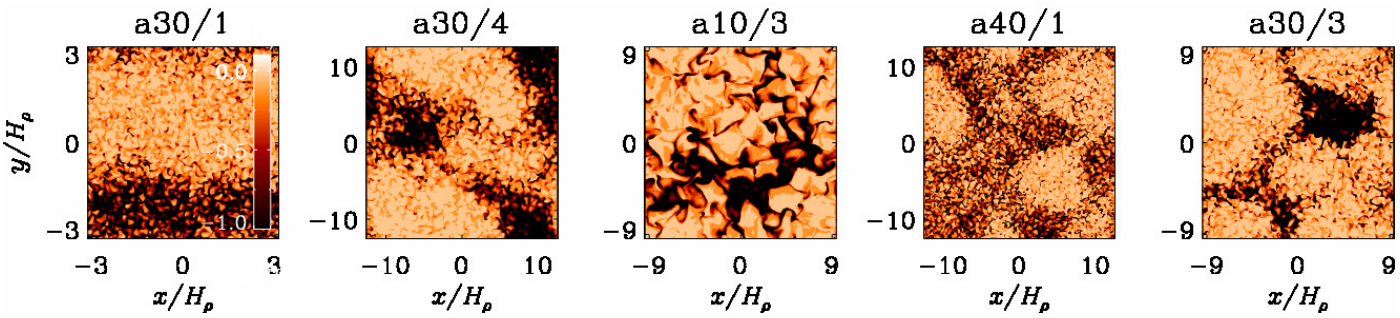

Fig. 17. Magnetic field configuration at the upper surface for DNS Runs a30/1–a30/3 of Table 5.

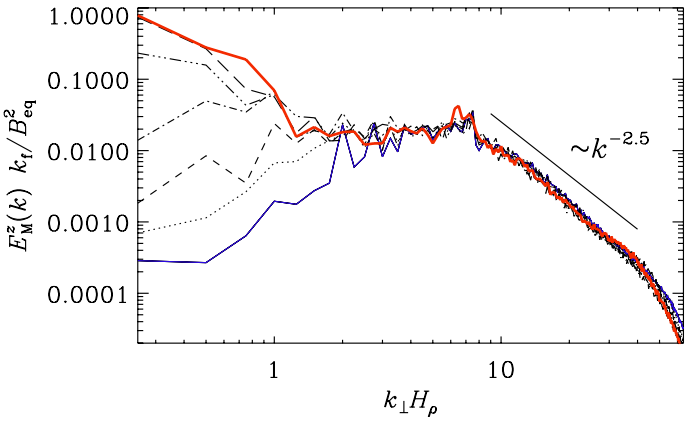

Fig. 18. Normalized spectra of B_z from DNS Run a30/4 at normalized times $t\eta_{t0}/H_\rho^2 \approx 0.2$, 0.5, 1, 2, 5, 10, and 20, for $\hat{g} \equiv g/c_s^2 k_f = 4$.

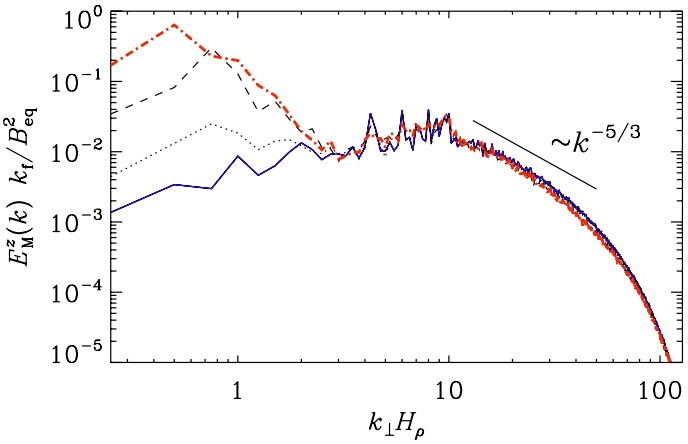

Fig. 19. Normalized spectra of B_z from DNS Run A40/1 at normalized times $t\eta_{t0}/H_\rho^2 \approx 0.2$, 0.5, 1, and 2.7 with $k_f H_\rho = 10$ and $k_1 H_\rho = 0.25$.

have improved in the sense that the flux concentrations are now stronger when there is a vertical magnetic field. In particular, the resulting magnetic structures survive in the presence of larger Mach numbers up to 0.7, which is relevant to the photospheric layers of the Sun (Stein & Nordlund 1998). However, those structures do become somewhat weaker as the magnetic Reynolds number is increased sufficiently to allow for the presence of small-scale dynamo action. This was expected based on a certain drop of $\beta_\star$ for $\mathrm{Re}_M \gtrsim 60$ found in earlier simulations (Brandenburg et al. 2012), but the possibility of spot formation still persists. More specifically, we have seen that the largest field strength, $\overline{B}_z/B_0$, occurs at a height where $\overline{B}_z^{\max}/B_{eq}$ is at least 0.4; see Fig. 16.

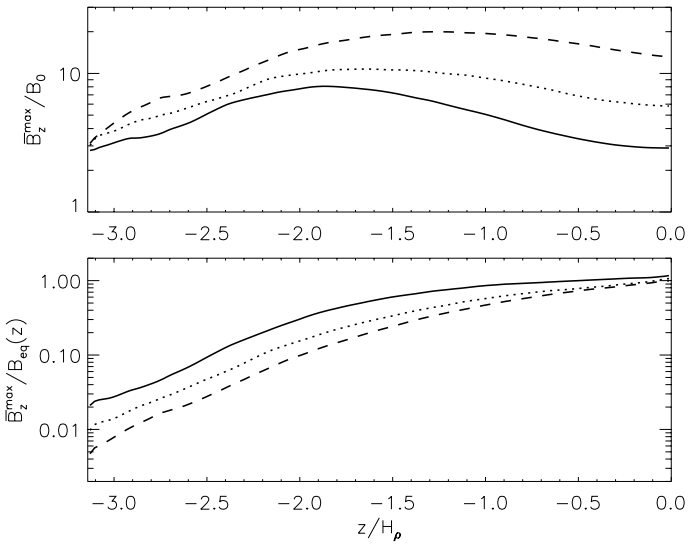

Fig. 20. Same as Fig. 13, but for the ILES runs with varying forcing amplitude. Note the different vertical extent of this set of models. The different lines indicate Ma = 0.16 (solid), 0.34 (dotted), and 0.68 (dashed).

To speculate further regarding the applicability to sunspot formation, we must look at the mean-field models presented in Sect. 2. In particular, we have seen that spot formation occurs at a depth $z_B^{\rm NL}$ where $\overline{B}_z^{\max}/B_{eq}$ is between 0.6 (for $\mathrm{Re}_M = 40$) and 0.4 (for $\mathrm{Re}_M = 95$); see Fig. 14 and Table 4. Larger ratios of $\overline{B}_z^{\max}/B_{eq}$ occur in the upper layers, but then the absolute field strength is lower. In the MFS of Sect. 2, the value of $\overline{B}_z^{\max}/B_{eq}$ at $z = z_B^{\rm NL}$ is somewhat smaller (around 0.3), suggesting that the adopted set of mean-field parameters in Eq. (21) was slightly suboptimal. Nevertheless, those models show that the depth where NEMPI occurs and where the effective magnetic pressure is most negative is even further down, e.g., at $z/H_\rho \approx -7$; see Fig. 5. Furthermore, at the depth where $(-\mathrm{d}\mathcal{P}_{\rm eff}/\mathrm{d}\ln\beta^2)^{1/2}$ is maximum, i.e., where NEMPI is strongest according to theory, we find $\overline{B}_z^{\max}/B_{eq} \approx 0.05$. Thus, there is an almost tenfold increase of the absolute field strength between the depth were NEMPI occurs and where the field is strongest.

As we have seen from Fig. 5, this increase is caused solely by hydraulic effects, similar to what Parker (1976, 1978) anticipated over 35 years ago. Our isothermal models clearly do demonstrate the hydraulic effect due to downward suction, but we cannot expect realistic estimates for the resulting field amplification. Parker (1978) gives more realistic estimates, but in his work the source of downward flows remained unclear. Our present work suggests that NEMPI might drive such motion, but in realistic simulations it would be harder to identify this

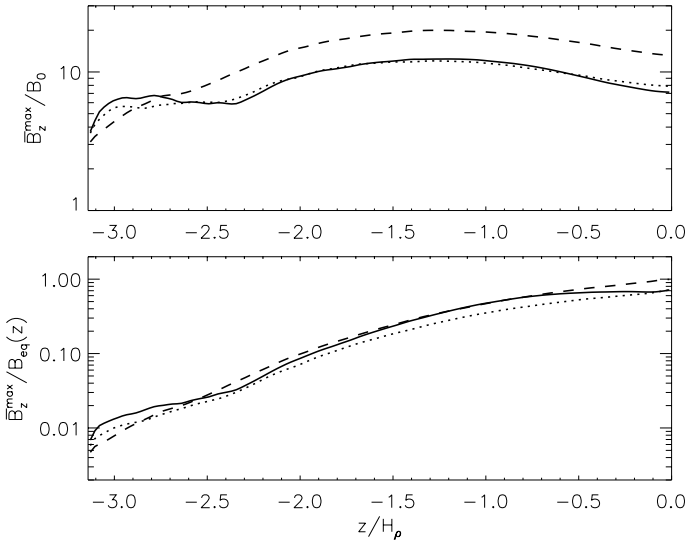

Fig. 21. Same as Fig. 20, but for the ILES runs which vary both the forcing amplitude and the imposed magnetic field at the same time, keeping the *relative* field strength comparable. The different lines again indicate Ma = 0.16 (solid), 0.35 (dotted), and 0.68 (dashed), and agree markedly well in the *lower panel* where we plot relative to $B_{eq}(z)$.

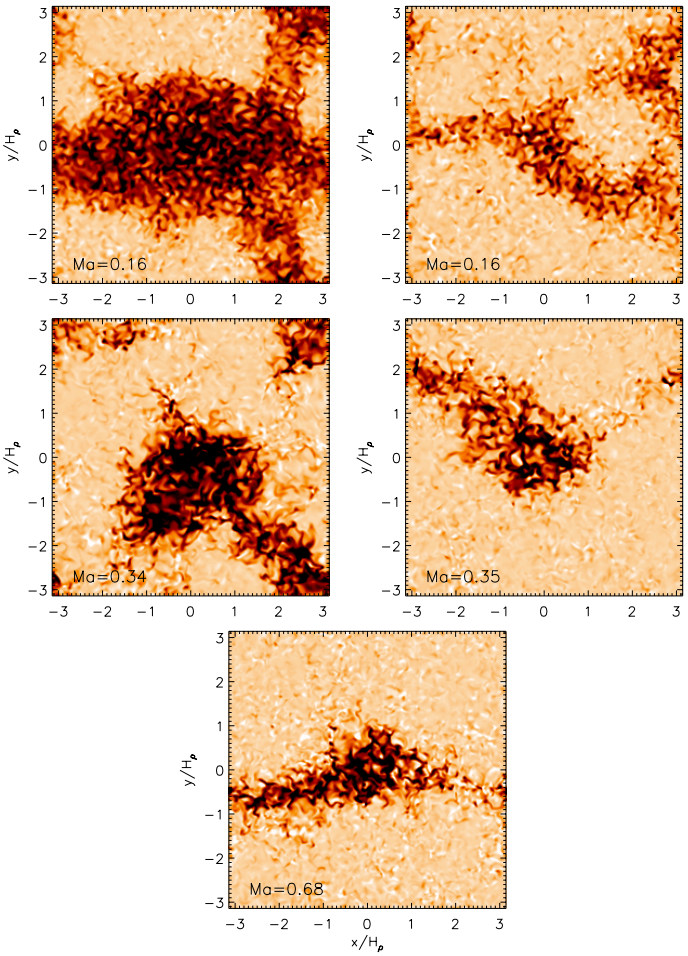

Fig. 22. Surface appearance of the vertical magnetic field, B_z^{max}, in the ILES simulations with different Mach numbers (*top to bottom*). The color coding shows B_z^{max}/B_{eq} in the range of −0.1 (white) to +1.0 (black). Root-mean-square Mach numbers are given by the labels. For the *upper two rows* with lower Mach number, the *left column* is for fixed initial mean field, whereas in the *right column* the initial field is adjusted between the runs, such that the field strength remains constant relative to the kinetic energy in the background turbulence.

as the sole mechanism. Another mechanism might simply be large-scale hydrodynamic convection flows that would continue deeper down to the lower part of the supergranulation layer at depths between 20 and 40 Mm. Some indications of this have now been seen in simulations of Stein & Nordlund (2012). Whether the reason for flux concentrations is then NEMPI or convection can only be determined through careful numerical experiments comparing full MHD with the case of a passive vector field. Such a field would still be advected by convective flows but would not contribute to the dynamical effects that would be required if NEMPI were to be responsible.

In addition to the magnetic field strength of flux concentrations, there might also be issues concerning their size. Usually they are not much larger than about 5 density scale heights; see, e.g., Fig. 15. This might be too small to explain sunspots. On the other hand, in the supergranulation layer, the density scale height increases, and larger scale structures might be produced at those depths.

To make this more concrete, let us discuss a possible scenario. At a depth of 3 Mm, the equipartition field strength is about 2 kG, and this might be where the sunspot field is strongest. If NEMPI was to be responsible for this, we should expect the effective magnetic pressure to be negative at a depth of about 10 Mm. Here, the equipartition field strength is about 3 kG. If NEMPI operates at $\overline{B}_z^{max}/B_{eq} \approx 0.1$, this would correspond to $\overline{B}_z^{max} \approx 300$ G, which appears plausible. At that depth, the density scale height is also about 10 Mm. Thus, if magnetic flux concentrations have a size of 5 density scale heights, then this would correspond to 50 Mm at that depth. To produce spots higher up, the field would need to be more concentrated, which would reduce the size by a factor of 3 again. However, given the many uncertainties, it is impossible to draw any further conclusions until NEMPI has been studied under more realistic conditions relevant to the Sun.

5. Conclusions

Using DNS, ILES and MFS in a wide range of parameters we have demonstrated that an initially uniform vertical weak magnetic field in strongly stratified MHD turbulence with large scale separation results in the formation of circular magnetic spots of equipartition and super-equipartition field strengths. Although we have confirmed that the normalized horizontal wavenumber of magnetic flux concentrations is $k_\perp H_\rho \approx 0.8$, as found earlier for horizontal imposed field (Kemel et al. 2013), it is now clear that in the nonlinear regime smaller values can be attained. This happens in a fashion reminiscent of an inverse cascade or inverse transfer[5] in helically forced turbulence (Brandenburg 2001). In the present case, this inverse transfer is found both in MFS and in DNS. This property helps explaining the possibility of larger length scales separating different flux concentrations.

The study of axisymmetric MFS helps understanding the dependence of NEMPI on the parameters $\beta_\star$ and β_p, which determine the parameterization of the effective magnetic

[5] In both cases, the transfer is *nonlocal* in wavenumber space. It is therefore more appropriate to use the term inverse transfer instead of inverse cascade.

pressure, $\mathcal{P}_{\rm eff}(\beta)$. It was always clear that changes in those parameters can significantly change the functional form of $\mathcal{P}_{\rm eff}(\beta)$, and yet the resulting growth rate of NEMPI was found to depend mainly on the value of $\beta_\star$. We now see, however, that the shape of the resulting solutions still depends on the value of $\beta_{\rm p}$, in addition to a dependence on $\beta_\star$. In fact, smaller values of $\beta_{\rm p}$ as well as larger values of $\beta_\star$ both result in longer structures. This is important background information in attempts to find flux concentrations in DNS, where the domain might not always be tall enough. As a rule of thumb, we can now say that the domain is deep enough if the resulting large-scale magnetic field is below 1% of the equipartition value. This is confirmed by Figs. 13 and 14 as well as Figs. 20 and 21, where all runs with $\overline{B}_z^{\rm max}/B_{\rm eq}(z) \le 0.01$ at $z = z_{\rm bot}$ reach $\overline{B}_z^{\rm max}/B_{\rm eq}(z) = O(1)$ at $z = z_{\rm top}$, provided the domain is also high enough. A limited extent at the top appears to be less critical than at the bottom, because NEMPI still develops in almost the same way as before.

It is important to emphasize that the formation of magnetic flux concentrations is equally well possible at large Mach numbers. This is important in view of applications to the Sun, where in the upper layers Ma ≈ 0.5 can be expected. Nevertheless, our present investigations have not yet been able to address the question whether sunspots can really form through NEMPI. For that, we would need to abandon the assumption of isothermality. Nevertheless, we expect the basic feature of downflows along flux tubes to persist also in that case. It is the associated inflow from the side that keeps the tube concentrated. Such flows have indeed been seen in local helioseismology (Zhao et al. 2010). Those authors also find an additional outflow higher in the photosphere that is known as the Evershed flow.

We expect that the downflow in the tube plays an important role in an unstably stratified layer, such as in the Sun, where it brings low entropy material to deeper layers, lowering therefore the effective temperature in the magnetic tubes. Future work should hopefully be able to demonstrate that in detail. The conceptual difference between NEMPI and other mechanisms may not always be very clear. However, by using an isothermal layer, we can be sure that convection is not operating. Thus, the phenomenon of flux segregation found by Tao et al. (1998) would not work. Conversely, however, NEMPI might well be a viable explanation for this phenomenon too. Whether the concept of flux expulsion can really serve as an alternative paradigm is unclear, because it is difficult to draw any quantitative predictions from it. In particular, flux expulsion does not make any reference to turbulent pressure or its suppression. Instead, the source of free energy is more directly potential energy which can be tapped through the superadiabatic gradient in convection. By contrast, the source of free energy for NEMPI is turbulent energy. The other possibility discussed above is the network of downdrafts associated with the supergranulation layer (Stein & Nordlund 2012). This mechanism is not easily disentangled from NEMPI, because both imply flux concentrations in downdrafts. However, in an isothermal layer, we can be sure that supergranulation flows are absent, so NEMPI is the only known mechanism able to explain the flux concentrations shown in the present paper.

Acknowledgements. This work was supported in part by the European Research Council under the AstroDyn Research Project No. 227952, by the Swedish Research Council under the project grants 2012-5797 and 621-2011-5076 (AB), by the European Research Council under the Atmospheric Research Project No. 227915, and by a grant from the Government of the Russian Federation under contract No. 11.G34.31.0048 (NK, IR). We acknowledge the allocation of computing resources provided by the Swedish National Allocations Committee at the Center for Parallel Computers at the Royal Institute of Technology in Stockholm and the National Supercomputer Centers in Linköping, the High Performance Computing Center North in Umeå, and the Nordic High Performance Computing Center in Reykjavik. Part of this work used the N code version 3.3, developed by Udo Ziegler at the Leibniz-Institut für Astrophysik Potsdam (AIP).

References

Biskamp, D. 1993, Nonlinear magnetohydrodynamics (Cambridge: Cambridge University Press)
Brandenburg, A. 2001, ApJ, 550, 824
Brandenburg, A. 2005, ApJ, 625, 539
Brandenburg, A., Kemel, K., Kleeorin, N., Mitra, D., & Rogachevskii, I. 2011, ApJ, 740, L50
Brandenburg, A., Kemel, K., Kleeorin, N., Rogachevskii, I. 2012, ApJ, 749, 179
Brandenburg, A., Kleeorin, N., & Rogachevskii, I. 2013, ApJ, 776, L23
Cheung, M. C. M., Rempel, M., Title, A. M., & Schüssler, M. 2010, ApJ, 720, 233
Fan, Y. 2009, Liv. Rev. Sol. Phys., 6, 4
Frisch, U., Pouquet, A., Léorat, J., & Mazure, A. 1975, J. Fluid Mech., 68, 769
Grinstein, F. F., Fureby, C., & DeVore, C. R. 2005, Int. J. Num. Meth. Fluids, 47, 1043
Kemel, K., Brandenburg, A., Kleeorin, N., Mitra, D., & Rogachevskii, I. 2012a, Sol. Phys., 280, 321
Kemel, K., Brandenburg, A., Kleeorin, N., & Rogachevskii, I. 2012b, Astron. Nachr., 333, 95
Kemel, K., Brandenburg, A., Kleeorin, N., Mitra, D., & Rogachevskii, I. 2013, Sol. Phys., 287, 293
Kitiashvili, I. N., Kosovichev, A. G., Wray, A. A., & Mansour, N. N. 2010, ApJ, 719, 307
Kleeorin, N., & Rogachevskii, I. 1994, Phys. Rev. E, 50, 2716
Kleeorin, N. I., Rogachevskii, I. V., & Ruzmaikin, A. A. 1989, Sov. Astron. Lett., 15, 274
Kleeorin, N. I., Rogachevskii, I. V., & Ruzmaikin, A. A. 1990, Sov. Phys. JETP, 70, 878
Kleeorin, N., Mond, M., & Rogachevskii, I. 1993, Phys. Fluids B, 5, 4128
Kleeorin, N., Mond, M., & Rogachevskii, I. 1996, A&A, 307, 293
Losada, I. R., Brandenburg, A., Kleeorin, N., Mitra, D., & Rogachevskii, I. 2012, A&A, 548, A49
Losada, I. R., Brandenburg, A., Kleeorin, N., & Rogachevskii, I. 2013, A&A, 556, A83
Parker, E. N. 1976, ApJ, 210, 816
Parker, E. N. 1978, ApJ, 221, 368
Pouquet, A., Frisch, U., & Léorat, J. 1976, J. Fluid Mech., 77, 321
Rempel, M. 2011, ApJ, 740, 15
Rogachevskii, I., & Kleeorin, N. 2007, Phys. Rev. E, 76, 056307
Rüdiger, G., Kitchatinov, L. L., & Brandenburg, A. 2011, Sol. Phys., 269, 3
Rüdiger, G., Kitchatinov, L. L.& Schultz, M. 2012, Astron. Nachr., 333, 84
Spruit, H. C. 1979, Sol. Phys., 61, 363
Spruit, H. C. 1981, A&A, 102, 129
Sur, S., Brandenburg, A., & Subramanian, K. 2008, MNRAS, 385, L15
Stein, R. F., & Nordlund, Å. 1998, ApJ, 499, 914
Stein, R. F., & Nordlund, Å. 2012, ApJ, 753, L13
Tao, L., Weiss, N. O., Brownjohn, D. P., & Proctor, M. R. E. 1998, ApJ, 496, L39
Warnecke, J., Losada, I. R., Brandenburg, A., Kleeorin, N., & Rogachevskii, I. 2013, ApJ, 777, L37
Zhao, J., Kosovichev, A. G., & Sekii, T. 2010, ApJ, 708, 304
Ziegler U., 2004, J. Comput. Phys., 196, 393